Polymerization of Ethylene with Supported Early and Late Transition Metal Catalysts

by

Yiyoung Choi

A thesis

presented to the University of Waterloo

in fulfillment of the

thesis requirement for the degree of

Doctor of Philosophy

in

Chemical Engineering

Waterloo, Ontario, Canada, 2011

Author's Declaration

I hereby declare that I am the sole author of this thesis. This is a true copy of the thesis, including any required final revisions, as accepted by my examiners.

I understand that my thesis may be made electronically available to the public.

Abstract

Single-site catalysts revolutionized the polyolefin manufacturing industry and research with their ability to make polymers with uniform microstructural properties. Several of these catalysts are currently used commercially to produce commodity and differentiated-commodity resins. The key to their rapid success and industrial implementation resides in the fact that they can be used without major modifications in the polymerization reactors that previously used heterogeneous Ziegler-Natta and Phillips catalysts. Since most of these industrial processes use slurry or gas-phase reactors, soluble single-site catalysts must be supported on adequate carriers that ensure not only high activity, but also the formation of polymer particles with the proper morphology and bulk densities.

Metallocene catalysts have been supported on a variety of carriers, but supporting late transition metal catalysts has not been investigated in detail, despite their very interesting properties such as tolerance to polar comonomers and impurities, activity in the absence of MAO, and the formation of short chain branches by the chain walking mechanism. The research work of this PhD thesis intends to fill this gap, by developing supported late transition metal catalysts with high catalyst activities towards ethylene polymerization and good polymer particle morphology.

The effects of catalyst structure and polymerization conditions on silica-supported nickel diimine catalysts are discussed in Chapter 3. Compared with the equivalent homogeneous catalysts, the covalently-attached supported catalysts had high activities, produced spherical polyethylene particles with good morphologies, and polyethylene with

higher melting temperatures, higher molecular weight averages, and broader molecular weight distributions. Borates used as internal activators during the synthesis of these supported catalysts successfully activated the nickel diimine complexes.

In Chapter 4, $MgCl_2$/alcohol adducts are recrystallized with alkylaluminum compounds and used as catalysts supports for nickel diimine complexes functionalized with amine groups. Polymerization results were compared with those of the equivalent SiO_2-supported nickel diimine catalysts. $MgCl_2$-based supported nickel diimine catalysts had high catalyst activity without the use of activators, and it was possible to control polymer molecular weight averages by changing the support composition.

Although linear low density polyethylene made with metallocenes offers superior mechanical properties such as excellent toughness, impact strength and clarity, it suffers from poor processability. To overcome some of these disadvantages, Chapter 5 introduces methods to produce bimodal polyethylene resins using supported hybrid early and late transition metal catalyst systems. The presence of short chain branches in the higher molecular weight component is attributable to the incorporation of α-olefin molecules by the metallocene sites, while the nickel diimine catalyst sites produce chains with a distribution of short chain branch sizes through the chain walking mechanism.

Finally, in Chapter 6 supporting a nickel diimine catalyst onto organo-modified montmorillonite (MMT) to prepare polyethylene/clay nanocomposites through in-situ polymerization is described. The thermal properties and crystallinity of the nanocomposites could be controlled by varying the fraction of MMT in the nanocomposite, and the dispersion

of the MMT layers in the polymer matrix were characterized by scanning electron microscopy (SEM) and transmission electron microscopy (TEM).

Acknowledgements

Firstly, I would like to thank my supervisor Dr. João B. P. Soares for his invaluable advice, guidance and encouragement. During my PhD program, his endless support cannot be described in any words.

I am really indebted to all of my group members, Saeid Mehdiabadi, Ahmad Alshaiban, Abolfazl Maneshi and Abdulaziz Abdullah for their cooperation and help. Especially, Dr. Anthony Shin shared with me creative ideas and comments that helped me focus better on my research. I extend a special appreciation to Dr. Kisoo Lee in LG Chem for motivating and supporting my PhD study.

I would also like to thank my friends, Hoonsub Song and his fiancée Sujeong Park, Taejung Kwon and his family, Teakdong Kim and his wife Eunmi Kim, Sangtak Park and his family, Hantae Choi and his family, Kyungjoo Kim, Youngjae Kim, Seokwoo Lee, Dr. Hyuksang Park, Miok Park, Hyunjoo Jang for unforgettable memories in Waterloo.

Finally, I would like to thank my parents, Jongsoo Choi and Moosoon Yang, Youngin Park and Kyuok Sung for their unlimited support and understandings. I wish to thank my beloved wife, Eunyoung Park, and my children, Sanghyun and Sanghoon for their love, patience and encouragement. I dedicate this thesis to all of them.

Dedication

To my wife, Eunyoung

Table of Contents

Author's Declaration ..... **ii**

Abstract ..... **iii**

Acknowledgements ..... **vi**

Dedication ..... **vii**

Table of Contents ..... **viii**

List of Figures ..... **xiii**

List of Tables ..... **xviii**

List of Schemes ..... **xx**

Nomenclature ..... **xxii**

Chapter 1 : Introduction **1**

Chapter 2 : Literature Review **4**

2.1. Transition Metal Catalysts for Olefin Polymerization 4

2.2. Silica Supported Single-Site Catalysts for Slurry and Gas-Phase Reactors 11

2.2.1. Silica as Support Material 11

2.2.2. Techniques for Supporting Metallocenes on Silica 14

2.2.3. Other Supporting Techniques 22

2.2.4. Silica Supported Nickel Diimine Catalysts 23

2.2.5. Other Single-Site Catalysts Supported on Silica 24

2.3. Single-Site Catalysts Supported on Other Carriers 25

2.3.1. $MgCl_2$-Supported Single-Site Catalysts 25

2.3.2. Clay-Supported Single-Site Catalysts 26

2.3.3. Zeolite-Supported Single-Site Catalysts 28

2.3.4. Alumina-Supported Single-Site Catalysts 29

2.3.5. Polymer-Supported Single-Site Catalysts 30

2.4. Supported Dual-Site Metallocene Catalysts and Hybrid Transition Metal Catalysts 31

2.5. Conclusion 33

Chapter 3 : Synthesis of Supported Nickel Diimine Catalysts for Ethylene Slurry Polymerization 34

3.1. Introduction 34

3.2. Experimental 35

3.2.1. Materials 35

3.2.2. Synthesis of Nickel Diimine Complexes 36

3.2.3. Synthesis of Supported Nickel Diimine Catalysts 41

3.2.4. Characterization of Supported Nickel Diimine Catalysts 44

3.2.5. Polymerization 44

3.2.6. Polymer Characterization..... 45

3.3. Results and Discussion 46

3.3.1. Supporting Efficiency of Supported Nickel Diimine Catalysts..... 46

3.3.2. Ethylene Polymerization Using Homogeneous Nickel Diimine Catalysts 47

3.3.3. Ethylene Polymerization Using Physisorbed Supported Nickel Diimine Catalysts..... 49

3.3.4. Ethylene Polymerization Using Covalently-Attached Supported Nickel Diimine Catalysts..... 52

3.3.5. Ethylene Polymerization with Covalently-Attached Supported Nickel Diimine Catalysts with Borate Activator..... 58

3.4. Conclusion 62

Chapter 4 : Ethylene Slurry Polymerization Using Nickel Diimine Catalysts Covalently-Attached onto $MgCl_2$-Based Supports 63

4.1. Introduction..... 63

4.2. Experimental 64

4.2.1. Materials 64

4.2.2. Synthesis of $MgCl_2$-Based Supported Nickel Diimine Catalysts 64

4.2.3. Characterization of Supported Nickel Diimine catalysts..... 65

4.2.4. Polymerization 65

4.2.5. Polymer Characterization 66

4.3. Results and Discussion 66

4.3.1. Structure of $MgCl_2$-Based Supported Nickel Diimine Catalysts 66

4.3.2. Ethylene Polymerization 70

4. 4. Conclusion 77

Chapter 5 : Supported Hybrid Early and Late Transition Metal Catalysts for the Synthesis of Polyethylene with Tailored Molecular Weight and Chemical Composition Distributions 78

5. 1. Introduction 78

5.2. Experimental 79

5.2.1. Materials 79

5.2.2. Synthesis of Supported Catalysts 81

5.2.3. Characterization of the Supported Catalysts 82

5.2.4. Polymerization 82

5.2.5. Polymer Characterization 82

5.3. Results and Discussion 83

5.3.1. Supported Catalyst Structure 83

5.3.2. Polymerization 85

5.3.3. SCB Characterization 107

5.3.4. Polymer morphology 109

5.4. Conclusion 114

Chapter 6 : Preparation of Polyethylene/MMT Nanocomposites Through In Situ Polymerization Using a Montmorillonite-Supported Nickel Diimine Catalyst 115

6.1. Introduction 115

6.2. Experimental 117

6.2.1. Materials 117

6.2.2. Nanocomposite Characterization 117

6.2.3. Synthesis of the MMT-supported nickel diimine catalysts 118

6.2.4. In Situ Polymerization 119

6.3. Results and Discussion 119

6.3.1. Structure of MMT-supported Nickel Diimine Catalysts 119

6.3.2. In Situ Polymerization 125

6.4. Conclusion 138

Chapter 7 : Recommendations 139

Bibliography 141

List of Figures

Figure 2.1. Example of multiple-site catalysts for olefin polymerization: (a) Ziegler-Natta catalyst; (b) Phillips catalyst. 5

Figure 2.2. Metallocene catalysts for olefin polymerization: (a) Cp_2ZrCl_2; (b) *rac*-$Et(Ind)_2ZrCl_2$; (c) iPr(Flu)(Cp)$ZrCl_2$; (d) Constrained geometry catalyst (CGC). 7

Figure 2.3. Cocatalysts used for metallocene activation: (a) Methylaluminoxane (MAO: cage structure); (b) Tetrakis(3,5-bis(trifluoromethyl)-phenyl)borate. 8

Figure 2.4. An example of a late transition metal catalyst for olefin polymerization: 1,4-bis(2,6-diisopropylphenyl)acenaphthene diimine nickel(II) dibromide. 9

Figure 2.5. Metallocene catalyst supported through a spacer group (Lee et al., 1999). 21

Figure 2.6. Structure of FI catalyst. 26

Figure 3.1. Borates structures: Dimethylanilium tetrakis(pentafluorophenyl)borate (**B1**), Lithium tetrakis(pentafluorophenyl)borate n-etherate (**B2**). 41

Figure 3.2. Structure of supported nickel diimine catalysts: a) **N1TS**; b) **N2TS**. 43

Figure 3.3. Cyrstaf (SCBD) profiles of polyethylene made with homogenous and supported nickel diimine catalyst: (1) **N1** (Run 1, Table 3.2); (2) **N1TS** (Run 4, Table 3.3). 51

Figure 3.4. Morphology of polymer made with **N1TS** (Run 4, Table 3.3). 52

Figure 3.5. Comparison of ethylene flow as a function of polymerization time for **N2** and **N2TS**: (1) Supported nickel diimine catalyst system (**N2TS**, Run 5, Table 3.4), (2) Homogenous nickel diimine complex system (**N2**, Run 7, Table 3.2). 55

Figure 3.6. SEM micrographs (scale bar 100 μm): a) **N2TS** particle before polymerization; b) Polyethylene particles made with **N2TS** (Run 6, Table 3.4). 57

Figure 3.7. A proposed structure for **N2B1TS**. 60

Figure 3.8. SEM micrographs (Run 2, Table 3.6): a) Polyethylene particles made with **N2B1TS (**scale bar 20 μm); b) A closer look at the external surface of a) (scale bar 0.4 μm)..... 61

Figure 4.1. SEM micrograph of a **N2Mg** particle (Entry 1 in the Table 4.1, scale bar 5 μm). 68

Figure 4.2. Cyrstaf (SCBD) profiles of polyethylene made with **N2** and **N2Mg**. 72

Figure 4.3. SEM micrographs of polymer particles: a) Polyethylene particles using **N2Mg (**Run 5 in Table 4.2, scale bar 200 μm); b) Polyethylene particles made with **N2Si (**Run 3 in Table 4.2, scale bar 200 μm); c) A closer look at the external surface of a) (scale bar 2 μm); d) A closer look at the external surface of b) (scale bar 2 μm)..... 76

Figure 5.1. a) Catalysts: bis(6-t-butoxyhexylcyclopentadienylide)zirconium dichloride (**Z**), methyl(6-t-butoxyhexyl)silyl(η^5-tetramethylcyclopentadienyl)(t-butylamido)titanium dichloride (**T**), and bis(4-amino-2,3,5,6-tetramethylimino)acenaphtene nickel(II) dibromide (**N**); and b) Activator: dimethylanilium tetrakis(pentafluorophenyl)borate (**B**). 80

Figure 5.2. MWD and SCB frequency profiles of poly(ethylene-*co*-1-hexene) made with $_S$**Z** (Run 9, Table 5.2). 87

Figure 5.3. CEF (CCD) profiles of poly(ethylene-*co*-1-hexene) made with $_S$**Z:** A (Run 7, Table 5.2), B (Run 8, Table 5.2) and C (Run 9, Table 5.2). 88

Figure 5.4. Representative pictures of polymer particles made with a: $_S$**Z** (Run 9, Table 5.2), b: $_S$**T** (Run 14, Table 5.2), c: $_S$**T** (Run 16, Table 5.2), and d: $_S$**N** (Run 9, Table 5.3). 89

Figure 5.5. MWD and SCB frequency profiles of polyethylene made with $_S$**N** (Run 7, Table 5.3). 91

Figure 5.6. CEF profiles for poly(ethylene-*co*-1-hexene) made with $_S$**N**: a) (Run 1 and 3, Table 5.3) and b) (Run 7 and 9, Table 5.3). 93

Figure 5.7. MWD and SCB frequency of polyethylene made with $_S$**ZN**. Polymerization conditions: a) 40°C, C6/C2 0.4 (Run 3, Table 5.4); b) 70°C, C6/C2 0 (Run 7, Table 5.4); c) 70°C, C6/C2 0.4 (Run 10, Table 5.4). 96

Figure 5.8. Representative pictures of polymer particles made with a: $_S$**ZN** (Run 10, Table 5.4), b: $_S$**TN** (Run 3, Table 5.6), c: $_S$**TN** (Run 7, Table 5.6), and d: $_S$**TN** (Run 9, Table 5.6). 97

Figure 5.9. CEF (CCD) profiles of polyethylene made with $_S$**ZN**: A (Run 7, Table 5.4), B (Run 8, Table 5.4), C (Run 9, Table 5.4) and D (Run 10, Table 5.4)..... 100

Figure 5.10. MWD and SCB frequencies for polyethylene made with $_S$**TN**. Polymerization conditions: a) 40°C, C6/C2 0.4 (Run 3, Table 5.6); b) 70°C, C6/C2 0.4 (Run 9, Table 5.6). 103

Figure 5.11. Comparison of MWDs for polyethylene samples made with $_S$**TN** at: a) 40°C (Runs 1-3, Table 5.6) and b) 70°C (Runs 7-9, Table 5.6). 105

Figure 5.12. CEF (CCD) profiles for polyethylene samples made with $_S$**TN**: A (Run 7, Table 5.6), B (Run 8, Table 5.6), C (Run 9, Table 5.6)..... 106

Figure 5.13. High-temperature ^{13}C NMR spectra for polyethylenes made with: a) $_S$**Z** (Run 9, Table 5.2), and b) $_S$**ZN** (Run 10, Table 5.4). 108

Figure 5.14. SEM micrographs of polymer particles made with $_S$**ZN** (Run 7, Table 5.4): a) External surface (scale bar 10 μm); b) A closer look at the region indicated with a square box on a) (scale bar 1 μm); c) A closer look at the region indicated with a square box on b) (scale bar 100 nm); d) Particle with different morphology from a) (scale bar 10 μm); e) A closer look at the region indicated with a square box on d) (scale bar 1 μm). 111

Figure 5.15. SEM micrographs of a microtomed slice of a polymer particle made with $_S$**ZN** (Run 7, Table 5.4): a) A sliced particle (inside white circle, scale bar 20 μm); b) A closer look at the region indicated with a square box on a) (scale bar 10 μm); c) A closer look at the region indicated with a square box on b) (scale bar 1 μm)..... 113

Figure 6.1. Structure of organic modifiers: a) Methyl tallow bis-2-hydroxyethyl ammonium (Cloisite 30B); b) Methyl di-hydrogenated tallow ammonium (Cloisite 93A)..... 117

Figure 6.2. TGA analysis results: a) Dried MMTs; b) MMT-supported nickel diimine catalysts. 122

Figure 6.3. X-ray diffraction patterns of the MMTs and MMT-supported **N2** catalyst: a) Cloisite Na and **CNa**, b) Cloisite 93A and **C93A**, c) Cloisite 30B and **C30B**..... 124

Figure 6.4. Comparison of ethylene uptake rates as a function of polymerization time: 1) Unsupported **N2** catalyst (Run 1, Table 6.1); 2) **C30B** (Run 11, Table 6.1)..... 127

Figure 6.5. Influence of MMT fraction of the derivative TGA curves for: a) PE/**CNa**; b) PE/**C93A**; and c) PE/**C30B**. 130

Figure 6.6. X-ray diffraction patterns of nanocomposites using MMT-supported nickel diimine catalysts: a) PE/**CNa**; b) PE/**C93A**. 131

Figure 6.7. X-ray diffraction patterns of nanocomposites using a MMT-supported nickel diimine catalyst: a) PE/**C30B** with activator; b) PE/**C30B** without activator. 132

Figure 6.8. SEM micrographs: a) **C30B** (scale bar 1 µm); b) Expanded view of a) (scale bar 0.4 µm); c) PE/**C30B** nanocomposite (Run 10 in Table 6.1, scale bar 200 µm); d) Expanded view of c) (scale bar 0.5 µm)..... 134

Figure 6.9. TEM micrographs (Run 17, Table 6.1): a) PE/**C30B** (scale bar 200 nm); b), c) and d) Closer views (scale bar 50 nm) of the regions marked as 1, 2 and 3 in a). 136

Figure 6.10. TEM micrographs of PE/**C30B** (Run 10, Table 1), scale bar 100 nm. 137

List of Tables

Table 3.1. Description of supported nickel diimine catalysts. 46

Table 3.2. Ethylene polymerization results using homogeneous nickel diimine complexes. 48

Table 3.3. Ethylene polymerization results using physisorbed supported nickel diimine catalysts. 50

Table 3.4. Ethylene polymerization results using covalently-attached supported nickel diimine catalysts. 53

Table 3.5. Comparison of ethylene polymerization results with different Al/Ni ratios. 56

Table 3.6. Ethylene polymerization results using supported nickel diimine catalysts with borate activators. 59

Table 4.1. Description of prepared $MgCl_2$-based supported nickel diimine catalysts. 69

Table 4.2. Comparison of ethylene polymerization results with homogeneous and supported nickel diimine catalysts. 70

Table 4.3. Ethylene polymerization results using $MgCl_2$-based supported nickel diimine catalysts in the absence of activator. 73

Table 4.4. Effect of the support components using **N2** complex on ethylene polymerization. 74

Table 5.1. Description of the supported catalysts. 85

Table 5.2. Results for ethylene homopolymerization and ethylene/1-hexene copolymerization using supported single catalysts $_S$**Z** and $_S$**T**. 86

Table 5.3. Results for ethylene homopolymerization and ethylene/1-hexene copolymerization with $_S$**N**. 90

Table 5.4. Results for ethylene homopolymerization and ethylene/1-hexene copolymerization with $_S$**ZN**. 95

Table 5.5. Theoretically calculated catalyst activity and M_w for $_S$**ZN** using results for $_S$**Z** and $_S$**N**. 99

Table 5.6. Results for ethylene homopolymerization and ethylene/1-hexene copolymerization using $_S$**TN**. 102

Table 5.7. Influence of catalyst structures and polymerization conditions on SCBD. 109

Table 6.1. Ethylene polymerization results using MMT-supported nickel diimine catalysts. 126

List of Schemes

Scheme 2.1. Chain walking mechanism for branch formation with late transition metal catalysis (Gate et al., 2000). 11

Scheme 2.2. Schematic representation of silica surface dehydration (Hlatky, 2000). 13

Scheme 2.3. Modified silica surface with HMDS (Schneider et al., 2001). 14

Scheme 2.4. Supporting Method A.1 with thermal-treated silica (Collins et al., 1992). 16

Scheme 2.5. Reaction of TMA with silica to form in situ MAO (Simplicio et al., 2004). 17

Scheme 2.6. Metallocene supporting by Method B.1 involves the reaction of hydroxyl groups on the silica surface and functional groups in the metallocene ligands (US Patent 5767300, 1998). 19

Scheme 2.7. Metallocene supporting by Method B.2 using siloxane groups (European Patent 839836, 1997). 20

Scheme 2.8. Metallocene synthesis by the consecutive-combined method (Soga et al., 1994a). 21

Scheme 2.9. Possible mechanism of supporting Fe(II) catalyst on silica (Ma et al., 2002)... 24

Scheme 2.10. Supported 2,6-Bis(imino)pyridyl Fe(II) and Co(II) catalysts (Kim et al., 2003). 25

Scheme 2.11. Supporting a metallocene catalyst on a clay layer (M: Ti, Zr; Weiss et al., 2002). 27

Scheme 2.12. Activation of metallocene catalysts on the DEAL-ZSM-2 zeolite surface. 29

Scheme 2.13. Synthetic route of a polystyrene-supported catalyst (Kitagawa et al., 1997). . 31

Scheme 3.1. Synthesis of 1,4-bis(2,6-diisopropylphenyl) acenaphthene nickel(II) dibromide (**N1**)..... 37

Scheme 3.2. Synthesis of bis(4-amino-2,3,5,6-tetramethylimino)acenaphtene nickel(II) dibromide (**N2**). 39

Scheme 3.3. Synthesis of bis(4-amino-2,3,5,6-tetramethylimino)butane nickel(II) dibromide (**N3**)..... 40

Scheme 4.1. Preparation of $MgCl_2$-based supported nickel diimine catalyst (**N2Mg**). 67

Scheme 5.1. Synthesis steps for supported hybrid catalysts (***s*ZN** and ***s*TN**)..... 84

Scheme 6.1. Preparation steps for **C30B** and PE/MMT nanocomposites..... 120

Nomenclature

Al	Aluminum
Al_2O_3	Alumina
B1	Dimethylanilium tetrakis(pentafluorophenyl)borate
B2	Lithium tetrakis(pentafluorophenyl)borate n-etherate
CCD	Chemical composition distribution
CEF	Crystallization elution fractionation
CGC	Constrained geometry catalyst ($Me_2Si(C_5Me_4)(N\text{-}t\text{Bu})TiCl_2$)
^{13}C NMR	Carbon 13 nuclear magnetic resonance
$CpTiCl_3$	Cyclopentadienyl titanium trichloride
Cp_2ZrCl_2	Bis(cyclopentadienyl)zirconium dichloride
Cr	Chromium
CRYSTAF	Crystallization analysis fractionation
C2	Ethylene
C6	1-Hexene
DSC	Differential scanning calorimetry
EASC	Ethylaluminum sesquichloride

EDX	Energy dispersive X-ray
HDPE	High density polyethylene
Hf	Hafnium
HMDS	Hexamethyl disilazine
HNO_3	Nitric acid
GPC	Gel permeation chromatography
GPC-IR	Gel permeation chromatography-Infrared spectroscopy
ICP	Inductively coupled plasma-optical emission spectroscopy
LLDPE	Linear low density polyethylene
MAO	Methylaluminoxane
$MgCl_2$	Magnesiumchloride
MMT	Montmorillonite
MWD	Molecular weight distribution
$NiBr_2$(DME)	Nickel(II) dibromide-ethyleneglycol dimethyl ether complex
Ni	Nickel
N1	1,4-Bis(2,6-diisopropylphenyl)acenaphthene nickel(II) dibromide
N2	Bis(4-amino-2,3,5,6-tetramethylimino)acenaphtene nickel(II) dibromide
N3	Bis(4-amino-2,3,5,6-tetramethylimino)butane nickel(II) dibromide
$(n\text{BuCp})_2ZrCl_2$	Bis(n-butylcyclopentadienyl)zirconium dichloride

Pd	Palladium
SiO_2	Silica
SCB	Short chain branch
SCBD	Short chain branching distributions
SEM	Scanning electron microscope
TEA	Triethylaluminum
TEM	Transmission electron microscope
Ti	Titanium
TIBA	Triisobutylaluminum
$TiCl_4$	Titaniumtetrachloride
TGA	Thermogravimertic analysis
TMA	Trimethylaluminum
TREF	Temperature rising elution crystallization
XRD	X-ray diffractometer
Zr	Zirconium
T_d	Maximum decomposition temperature
T_m	Melting temperature
M_w	Weight average molecular weight
M_w/M_n	Polydispersity index

A_{S^N}	Polymerization activities of catalyst **N**
A_{S^Z}	Polymerization activities of catalyst **Z**
m_Z	Molar fractions of polymer made with catalyst **Z**
m_N	Molar fractions of polymer made with catalyst **N**
x_Z	Molar fractions of catalyst **Z** in catalyst $_S$**ZN**
x_N	Molar fractions of catalyst **N** in catalyst $_S$**ZN**
$M_{w_{S^{ZN}}}$	Molecular weight of polymer made with catalyst $_S$**ZN**

Chapter 1 : Introduction

The polyolefin industry has been under constant development since Ziegler-Natta catalysts were invented in the 1950's. The total production of polyethylene and polypropylene was over 100 million tons in 2009, accounting for more than 60% of all industrial polymer production in the world (CMAI, 2010 World Polyolefins Analysis). The reasons for the success of polyolefins are their low production cost, and their well-defined molecular structures and properties that can be controlled by selecting adequate transition metal catalysts and polymerization conditions.

Single-site catalysts, including early (metallocenes) and late transition metal catalysts, are soluble in hydrocarbon solvents and are, therefore, classified as homogeneous catalysts. However, most commercial polyolefin production plants use slurry and gas-phase reactors; nearly 70 % of the total industrial polyolefin production results from the use of supported transition metal catalysts (Galli and Vecellio, 2004). The continuous operation of these slurry and gas-phase processes requires morphologically uniform catalyst particles that can be continuously fed to the reactor; soluble catalysts must be fixed onto insoluble carriers before

they can be used in these processes (Alonso et al., 2004; Chu et al., 2000; Fink et al., 2000; Hlatky, 2000; McKenna and Soares, 2001).

The morphology of the resultant polymer particles depends on the morphology of the support (the so-called replication phenomenon), that is, the support type controls the polymer particle size distribution and bulk density (Abbenhuis, 1999). It is very important that the catalyst structure, activity, and comonomer reactivity be maintained after its heterogenization. Moreover, the catalyst should not leach from the support during polymerization to avoid reactor fouling. The main advantages of supported catalysts over their homogeneous counterparts are: 1) the cocatalyst/catalyst ratio required to reach maximum activity is generally lower for supported catalysts than for homogeneous catalysts; 2) the average polymer molecular weight varies upon supporting, often by increasing; 3) the molecular weight distribution (MWD) may broaden upon catalyst supporting, facilitating processability (at the cost of poorer mechanical properties); 4) some supported catalysts can be activated by common alkylaluminum compounds in the absence of more expensive MAO; 5) different single-site catalysts can be incorporated onto the same support for producing polymers with tailored MWD and chemical composition distribution (CCD).

One of the most important developments in olefin polymerization with late transition metal catalysts was the development of nickel(II) and palladium(II) catalysts with α-diimine ligands. Some important features of these catalysts are worth noting: 1) they were the first late transition metal catalysts to make high molecular weight polyethylene; 2) nickel diimine catalysts have activity similar to metallocene catalysts when activated with methyl aluminoxane (MAO); and 3) the short chain branch (SCB) content of the polymer made with these catalysts can be controlled by varying polymerization conditions and ligand structure.

The main purpose of the present thesis is to synthesize polyethylene with well controlled morphology in a slurry reactor system using late transition metal catalysts supported on a variety of carriers. These supported catalysts were used to polymerize ethylene and copolymerize ethylene and 1-hexene to produce polymer particles with good morphology and controlled microstructural properties at high catalyst activities.

This thesis consists of seven Chapters: Chapter 1 gives a brief instruction to the thesis. Chapter 2 contains a literature review of transition metal catalysts for olefin polymerization, and supporting techniques using various carriers. Chapter 3 summarizes our experimental results on the synthesis of SiO_2-supported late transition metal catalysts and optimized supported catalyst systems for ethylene polymerization. Chapter 4 focuses on alternative $MgCl_2$-based supports to control catalyst activity and microstructural polymer properties. In Chapter 5, hybrid supported catalysts using two kinds of metallocenes and a nickel diimine catalyst are used to produce polyolefins with tailored microstructures. Chapter 6 explores a method to make polyolefin/clay nanocomposites through in situ polymerization using a nickel diimine catalyst supported on organically modified montmorillonite. Lastly, Chapter 7 presents some recommendations for future work.

Chapter 2 : Literature Review

2.1. Transition Metal Catalysts for Olefin Polymerization

The most common type of Ziegler-Natta catalyst is $TiCl_4$ supported on $MgCl_2$, mainly because of its high catalytic activity and excellent polymer particle morphology. Ziegler-Natta catalysts can make high density polyethylene (HDPE), linear low density polyethylene (LLDPE), and isotactic polypropylene, expanding the material properties available for polyolefins through the control of their branching structure, stereo- and regioregularity. The unique characteristic of Ziegler-Natta catalyst is the presence of several types of active sites. For polypropylene polymerization, the use of electron donors, such as ethers and esters, selectively poison aspecific sites so that the catalyst makes mostly isotactic polypropylene (Soares et al., 2007; Suhm et al., 1998).

Phillips catalysts are based on chromium oxide and are heterogenized on inorganic carriers such as silica. They are widely used for the production of HDPE. Phillips catalysts do not require a cocatalyst (activator), but they must be treated at high temperatures to become active. Hydrogen, the usual chain transfer agent for other transition metal catalysts, is not

effective for Phillips catalysts. Both heterogeneous Ziegler-Natta catalysts and Phillips have multiple active site types which are characterized by distinct comonomer reactivity ratios, chain transfer rates, and propagation rates. As a consequence, both catalysts make polyolefins with heterogeneous microstructure. This is commonly reflected in their broad molecular weight distribution (MWD) and chemical composition distribution (CCD) or short chain branching distributions (SCBD) (Bubeck, 2002; Soares et al., 2007). Figure 2.1 illustrates the typical structures of heterogeneous Ziegler-Natta and Phillips catalysts.

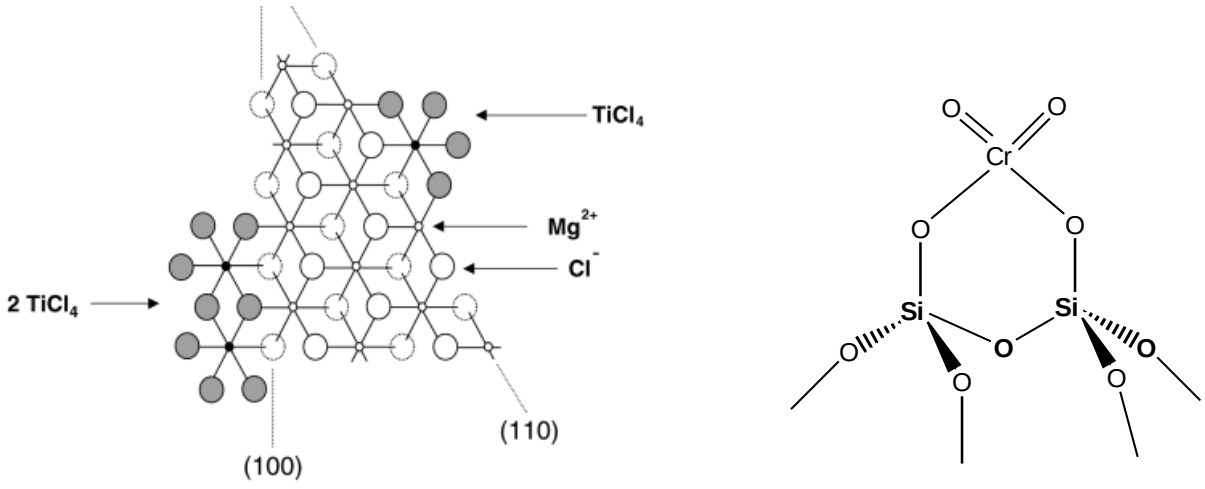

(a) (b)

Figure 2.1. Example of multiple-site catalysts for olefin polymerization: (a) Ziegler-Natta catalyst; (b) Phillips catalyst.

While most multiple-site catalysts produce α-olefin copolymers consisting of a mixture of homo- and copolymers with broad MWD, single-site catalysts such as metallocenes and late transition metal complexes permit the synthesis of polyethylenes and polypropylenes

with well-controlled microstructures, more homogeneous comonomer distributions, and lower polydispersities than those made with Ziegler-Natta catalysts; late transition metal catalysts can also produce polyolefins containing functional comonomers (Boffa and Novak, 2000; Brintzinger et al., 1995; Chung, 2002; Hamielec et al., 1996; Janiak, 2006; Wang, 2006).

Metallocenes are composed of an early transition metal (Ti, Zr, Hf), substituted cyclopentadienyl ligands, and halogen ligands. The general structure of metallocene catalysts is illustrated in Figure 2.2. The metal center is bonded to one or two cyclopentadienide anions and the cyclopentadienyl-type ligands can bear various alkyl or silyl substituents. The cyclopentadienyl-type ligands can be linked by one or more atoms to yield complexes that are referred to as *ansa*-metallocene. The electronic and steric environment around the active sites can be changed by modifying the metallocene ligand structure and the polymer microstructure can be controlled by catalyst design. This is why metallocenes are called tailor-made catalysts. A typical example of metallocene catalyst used in a commercial process is the constrained geometry catalyst (CGC), used for solution olefin polymerization (Bubeck, 2002).

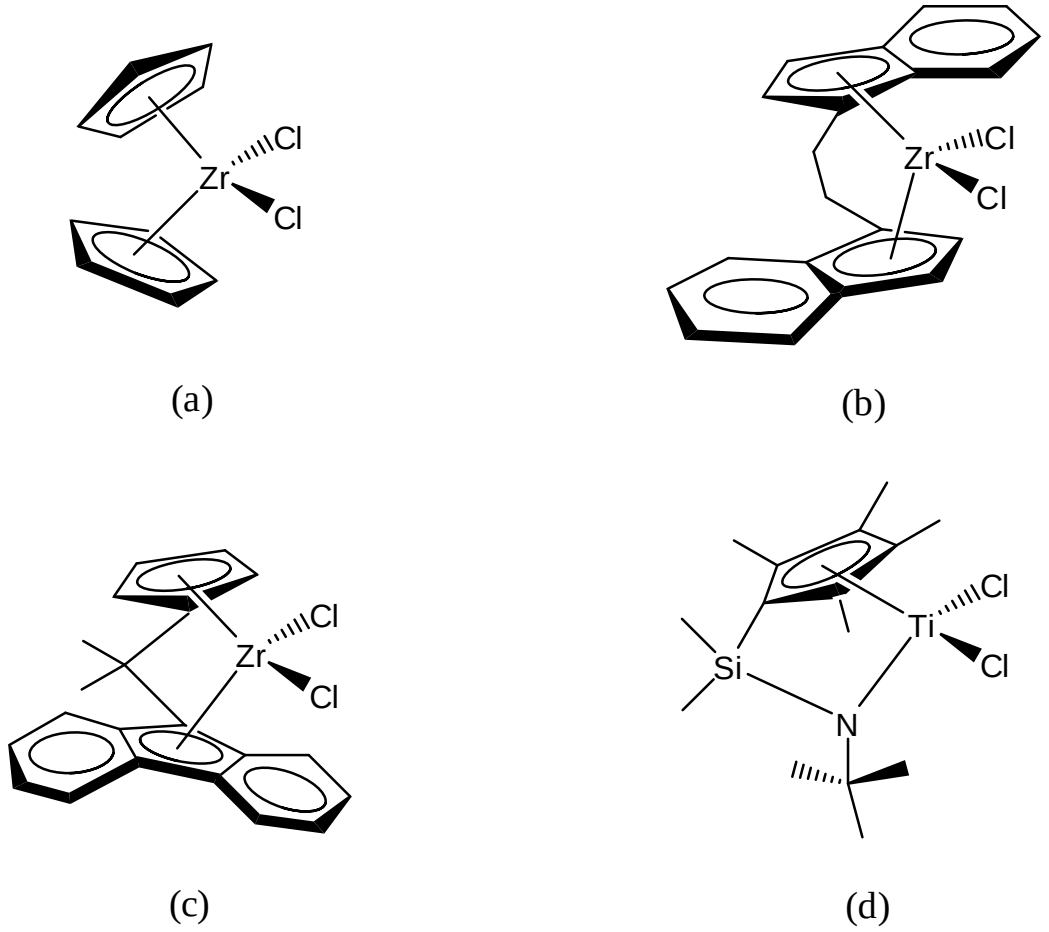

Figure 2.2. Metallocene catalysts for olefin polymerization: (a) Cp_2ZrCl_2; (b) *rac*-$Et(Ind)_2ZrCl_2$; (c) $iPr(Flu)(Cp)ZrCl_2$; (d) Constrained geometry catalyst (CGC).

Activators such as MAO and borate compounds are indispensable for metallocene activation (Figure 2.3). Metallocenes activated by alkylaluminums or aryl halides have low ethylene polymerization activities and are found to be inactive for propylene and higher olefins (Chen and Marks, 2000). MAO is produced from the hydroxylation of alkylaluminums under well controlled conditions (Bleinmeister et al., 1995). MAO has been identified with several roles in olefin polymerization: acting as an impurity scavenger and

alkylation agent, forming active sites, and preventing bimetallic deactivation of active sites. MAO quickly reacts with oxidizing compounds present in the reactor, thus preventing them from reacting with the sensitive metallocene molecules. MAO can also be used to treat catalyst supports prior to metallocene supporting, helping prevent catalyst deactivation and allowing active site formation.

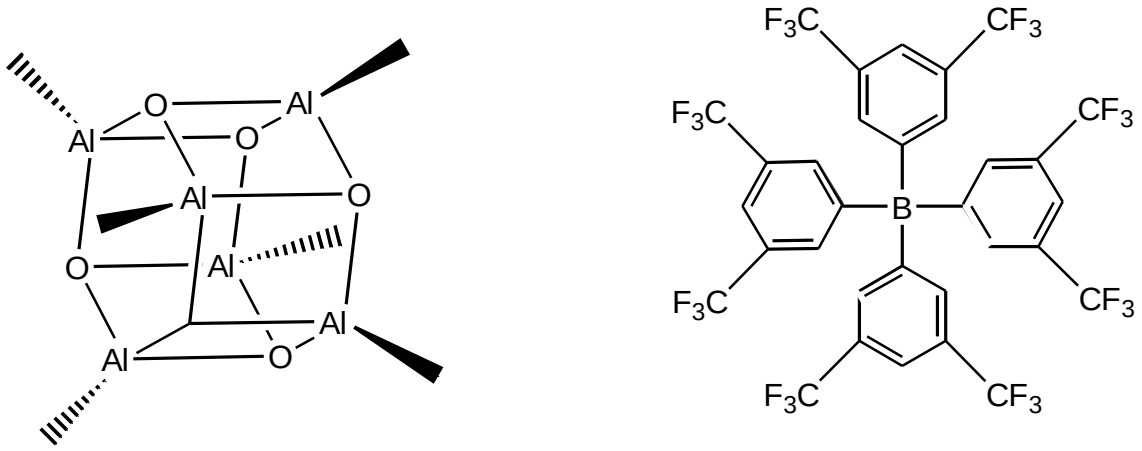

Figure 2.3. Cocatalysts used for metallocene activation: (a) Methylaluminoxane (MAO: cage structure); (b) Tetrakis(3,5-bis(trifluoromethyl)-phenyl)borate.

In general, ethylene insertion rates for late transition metal catalysts are lower than those of early transition metal catalysts such as metallocenes. Moreover, β-hydride elimination, leading to chain transfer, competes more strongly with chain growth, making it more difficult to produce polymers with high molecular weight. In spite of these difficulties, many late transition metal catalysts for olefin polymerization have been reported since Brookhart's group made their first high molecular weight polyethylene with bulky substituted aryl α-diimine nickel(II) catalysts (Johnson et al., 1995).

The high oxophilicity of early transition metal catalysts (Ti, Zr, Hf, Cr) causes them to be poisoned by most functionalized olefins. The lower oxophilicity and presumed greater function group tolerance of late transition metals (Ni, Pd) relative to early transition metals make them likely targets for the development of catalysts for the copolymerization of ethylene with polar comonomers under mild conditions. These catalysts are based largely on chelating nitrogen-based ligands that are active for homopolymerization of ethylene and the copolymerization of ethylene with α-olefins or polar comonomers (Figure 2.4).

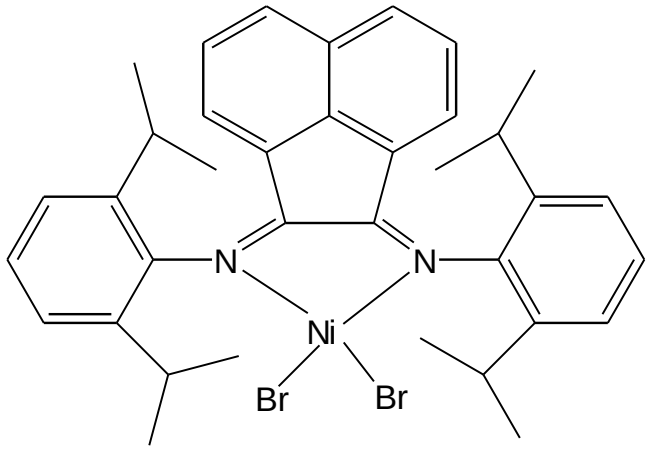

Figure 2.4. An example of a late transition metal catalyst for olefin polymerization: 1,4-bis(2,6-diisopropylphenyl)acenaphthene diimine nickel(II) dibromide.

The well-known Brookhart type α-diimine catalyst has three key features: 1) highly electrophilic cationic nickel or palladium metal centers; 2) sterically bulky α-diimine ligands; and 3) noncoordinating counterions. The electrophilicity of the late metal center in these cationic complexes results in rapid rates of olefin insertion. The use of bulky ligands favors insertion over chain transfer and the α-diimine ligands play a role in stabilizing the

organometallic complexes. The use of noncoordinating counterions provides an accessible coordination site for the incoming olefins (Ittel and Johnson, 2000).

Interestingly, late transition metal catalysts are known for making polyethylene with many short chain branches in the absence of α-olefin by a mechanism called *chain walking* (Gate et al., 2000). The mechanism for branch formation with late transition metal catalysts is shown in Scheme 2.1. Metal migration (*chain walking*) along the alkyl chain can occur in these species via β-H elimination and re-addition reactions (to species C and D). These migration reactions occur without chain transfer. Successive migratory insertion and ethylene trapping cycle from species A leads to linear polymer chains, while insertion following *chain walking* leads to the introduction of short branches in the polymer chain. The higher the extent of *chain walking*, the more highly branched the polymer.

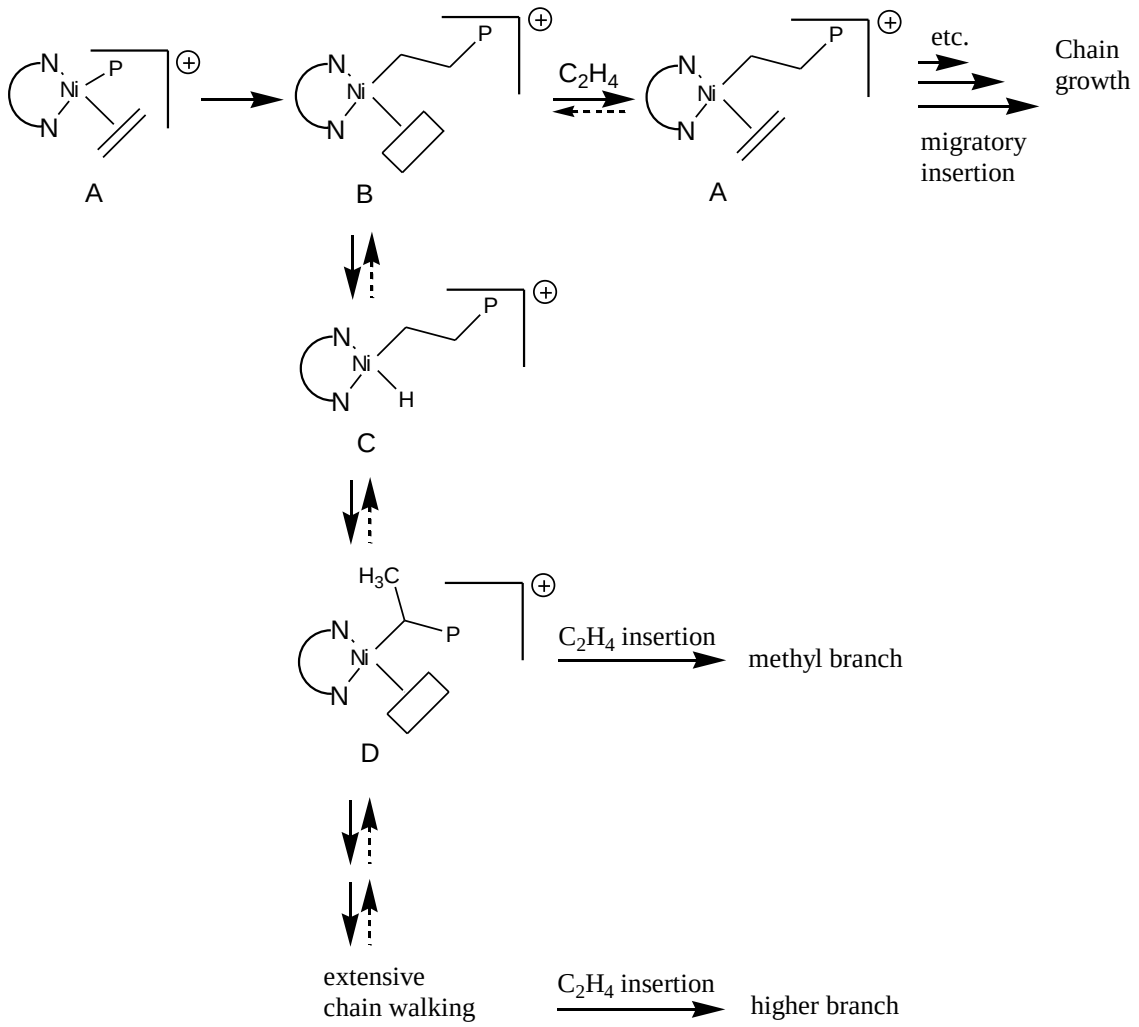

Scheme 2.1. Chain walking mechanism for branch formation with late transition metal catalysis (Gate et al., 2000).

2.2. Silica Supported Single-Site Catalysts for Slurry and Gas-Phase Reactors

2.2.1. Silica as Support Material

Key factors when selecting a support for an olefin polymerization catalyst are its chemical composition, surface characteristics, morphology (surface area, particle size distribution, pore size distribution, pore volume distribution) and mechanical strength.

Silica is the most extensively used support for metallocene and Phillips catalysts. Silica has several properties that make it attractive as a catalyst support: it is relatively chemically inert, stable at high temperatures, and can be synthesized with several pore sizes, volumes and surface areas. In addition, silica is a relatively inexpensive support, ideal for the production of commodity polymers such as polyolefins.

Porosity is a vital feature of catalyst supports, since it is one of the factors determining how good the polymer particle morphology will be (Fink et al., 2000). Unlike other, more unusual supports, not only the chemical but the physical properties of silica have been investigated – for instance, various publications exist comparing the performance of silica with varying porosities (Pullukat et al., 1998; Quijada et al., 1997; Santos et al., 1997). In general, support materials with high pore volumes result in higher activity catalysts that produce polymers with better morphology. However, a metallocene supported on non-porous silica yielded higher activity for ethylene polymerization compared to a similar porous material, which suggested that some of the catalyst trapped in the pores may not be active (Quijada et al., 1997). In addition, silica particles of varying particle sizes have been studied (Przybyla et al., 1999). Catalyst particles with smaller diameters were found to be more active and had a shorter induction period, likely due to less significant inter- and intraparticle mass transfer limitations, a more uniform intraparticle distribution of activator, and an earlier onset of catalyst fragmentation which helps expose new active sites to the polymerization medium.

The chemical properties of silica are mostly governed by the presence of silanol groups on its surface that can be changed with appropriate thermal or chemical treatments. Scheme 2.2 illustrates the thermally-induced change of silica surface groups from silanol to siloxane. The hydroxylated surface is hydrophilic and easily absorbs moisture from air. This physically

absorbed water can be desorbed by raising the temperature to 200°C. The number of hydroxyl groups decreases continuously as the temperature is raised, until at a temperature of 600-800°C an almost completely dehydroxylated silica surface with approximately 1.0 OH group per nm^{2} is left (Hlatky, 2000).

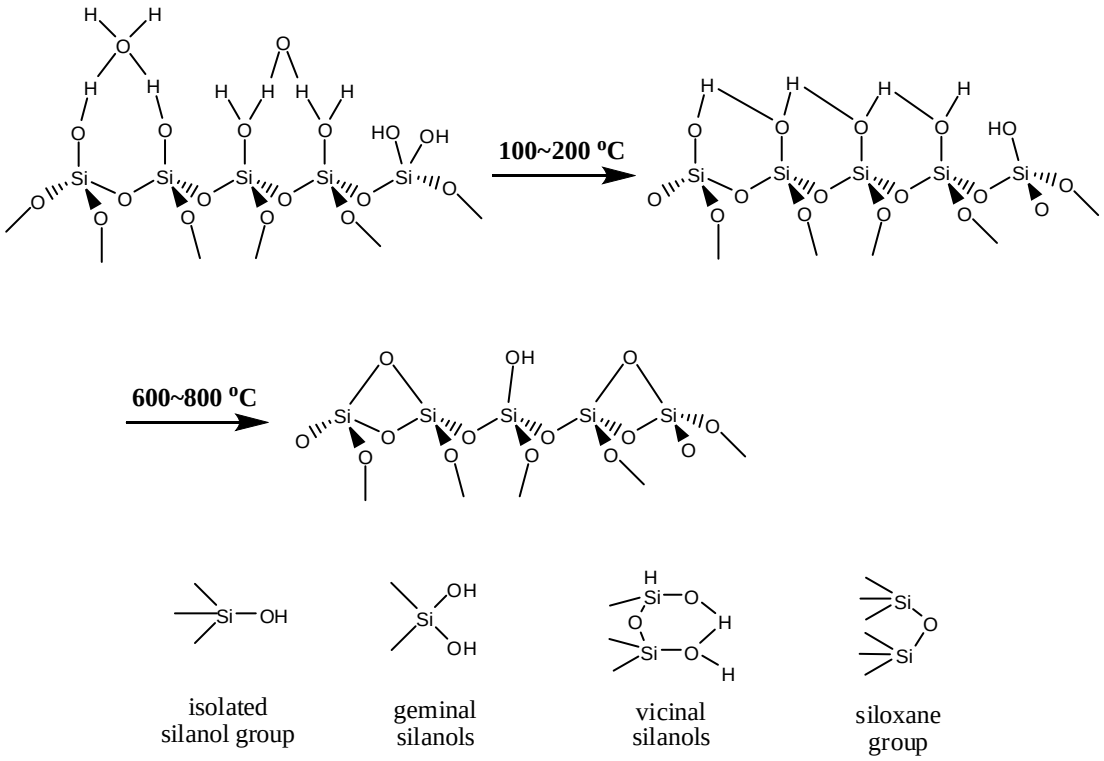

Scheme 2.2. Schematic representation of silica surface dehydration (Hlatky, 2000).

Hydroxyl groups on the silica surface may also be treated with a dehydroxylating agent such as hexamethyl disilazine (HMDS) to form other functional groups; this treatment is also effective in eliminating hydroxyl groups, as shown in Scheme 2.3 (Schneider et al., 2001).

Similarly, silica can be modified using $Si(CH_3)_2Cl_2$ followed by treatment with $NaHCO_3$ aqueous solution (Soga and Kaminaka, 1993).

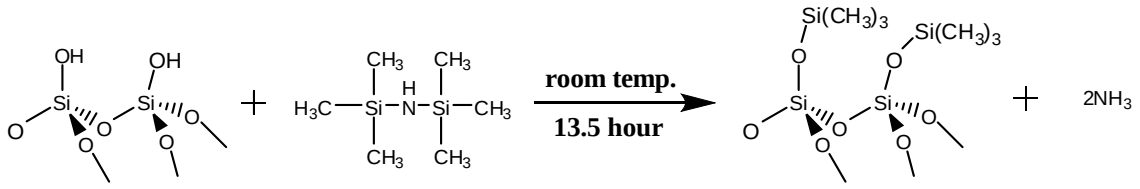

Scheme 2.3. Modified silica surface with HMDS (Schneider et al., 2001).

2.2.2. Techniques for Supporting Metallocenes on Silica

Various supporting methods have been used to immobilize metallocenes on silica surfaces; these methods are equally applicable to other single-site catalysts such as late transition metal complexes. These methods are listed below and will be described in more detail in the next paragraphs.

A. Physical adsorption supporting methods

Method A.1. SiO_2 / metallocene / activator

Method A.2. SiO_2 / activator / metallocene

Method A.3. SiO_2 / (metallocene + activator)

B. Covalent attachment supporting methods

Method B.1. SiO_2-OH / metallocene / activator

Method B.2. Si-O-Si / metallocene / activator

Physical adsorption supporting methods are very commonly used because of their simplicity (Kaminsky and Renner, 1993; Soga and Kaminaka, 1992; Soga and Lee, 1992; Soga et al., 1993b; US Patent 4701432, 1986). Method A.1 consists of supporting the metallocene compound on the carrier first, and then reacting it with an activator like MAO. The hydroxyl density on the silica surface decreases with increasing temperature and duration of the thermal treatment as a result of an increase in the number of siloxane reactive groups that lead to active immobilized metallocene sites, as depicted in Scheme 2.4 (Collins et al., 1992; Kaminsky et al., 1993; Santos et al., 1999). In some cases, active sites can react with hydroxyl groups that remain on the silica surface after the thermal treatment, producing inactive sites and significantly decreasing catalyst activity (Collins et al., 1992). In addition, catalyst poisons, such as HCl, may be formed during the supporting, further reducing catalyst activity. As a simpler method, supported catalysts can also be prepared by directly contacting metallocene and silica, while MAO is supplied as an external activator during polymerization (De Freitas et al., 2011).

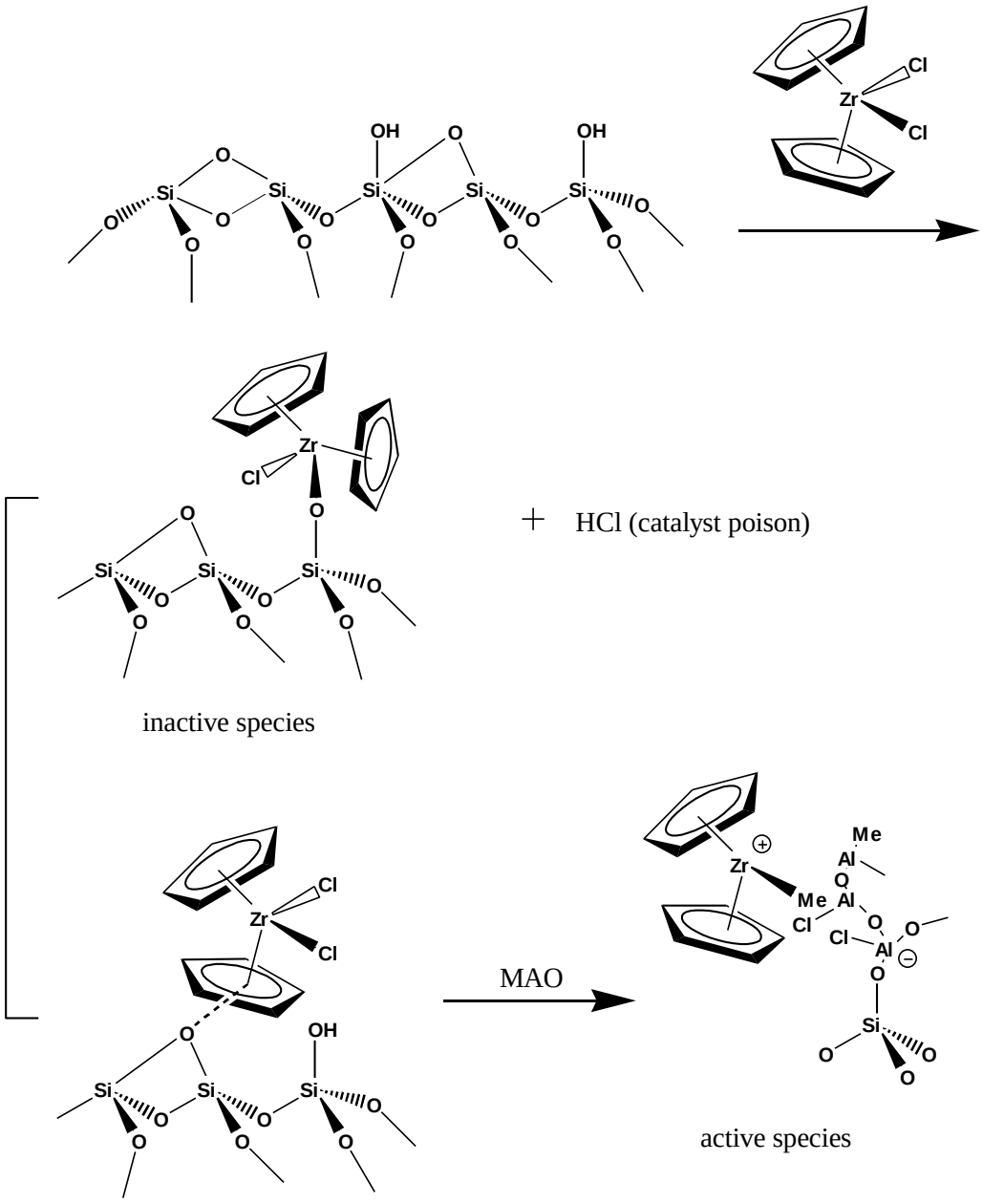

Scheme 2.4. Supporting Method A.1 with thermal-treated silica (Collins et al., 1992).

In Method A.2, silica is first treated with an alkylaluminum or aluminoxane, followed by washing, drying, and impregnation with an appropriate metallocene compound (Kaminaka and Soga, 1992; Soga and Kaminaka, 1992). Alternatively, the metallocene can be directly

supported onto commercially available MAO-modified silica (SMAO) (Franceschini et al., 2009). Not all supported metallocene catalysts made by this method have been found to be active if only alkylaluminums were used as activators (Kim, 1998). The supported catalyst obtained by this method can be further activated by the addition of MAO (Chien and He, 1991) and/or common alkylaluminums to the polymerization reactor (Soga et al., 1994a; Soga et al., 1994b). The SiO_2/MAO/metallocene/MAO system, commonly referred to as a "sandwich" structure on account of the position of the metallocene between two MAO layers, has also been explored (Tait and Ediati, 1999). Reversely, the slow addition of silica to an alkylaluminum solution was claimed to achieve high catalyst activity (US Patent 5006500, 1991; US Patent 5238892, 1993).

Instead of contacting the silica support with aluminoxane, TMA or a mixture of alkylaluminums can be reacted directly with the water adsorbed onto the silica surface, generating in situ aluminoxanes, as shown in Scheme 2.5 (Simplicio et al., 2004).

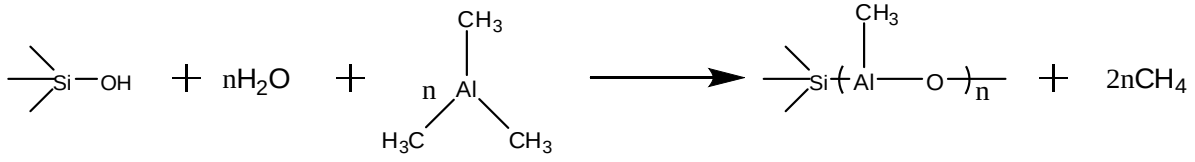

Scheme 2.5. Reaction of TMA with silica to form in situ MAO (Simplicio et al., 2004).

In Method A.3, the metallocene and the activator are pre-contacted before supporting. Because the metallocene is activated in solution, this procedure may increase the number of active sites and lead to highly active catalysts. This method also has the benefit of reducing

the number of reaction steps required during supporting and solvent usage (US Patent 5635437, 1997).

All the variations on the physical adsorption methods summarized above assume that the reagents and the support material onto which they adsorb are suspended or dissolved in a solvent. With a different approach, a supporting method emerged which involves the gas-phase impregnation of TMA and water vapor, and then of a metallocene onto a porous silica support with a known content of adsorbed water in a fluidized bed reactor (US Patent 6124229, 2000). This method reduces the preparation cost of the supported catalyst because MAO, generated and supported in situ, achieves higher loads than in slurry processes.

Metallocenes supported through physical adsorption methods are often extracted by the diluent during polymerization in slurry reactors. This evidently poses less of a problem for gas-phase reactors. These solubilized sites make polymer particles with poor morphology (polymer chunks) that cause reaction fouling in slurry processes. Fortunately, supporting methods that involve the covalent bonding of the catalyst to the support surface (B.1 and B.2) overcome the disadvantage of physical adsorption supporting methods, but may be more complex and expensive (Dubois and Zegarski, 1993; European Patent 839836, 1997; WO 087770, 2004).

Method B.1 is very attractive because it promotes the chemical bonding between support and catalyst. For example, a functional group may be added to the metallocene ligand to react with other functional groups present on the support surface. Metallocenes with chemically tethered groups are strongly supported and cannot be appreciably leached from the support surface during polymerization, avoiding reactor fouling. Scheme 2.6 illustrates a common

method for supporting metallocenes on silica: surface hydroxyl groups provide the anchoring sites for the functionalized metallocene complexes (US Patent 5767300, 1998). Unfortunately, other side reactions may also take place during supporting (for instance, between other metallocene ligands, such as chlorine, and silica), leading to the formation of inactive sites and other byproducts such as water and hydrochloric acid that act as catalyst poisons.

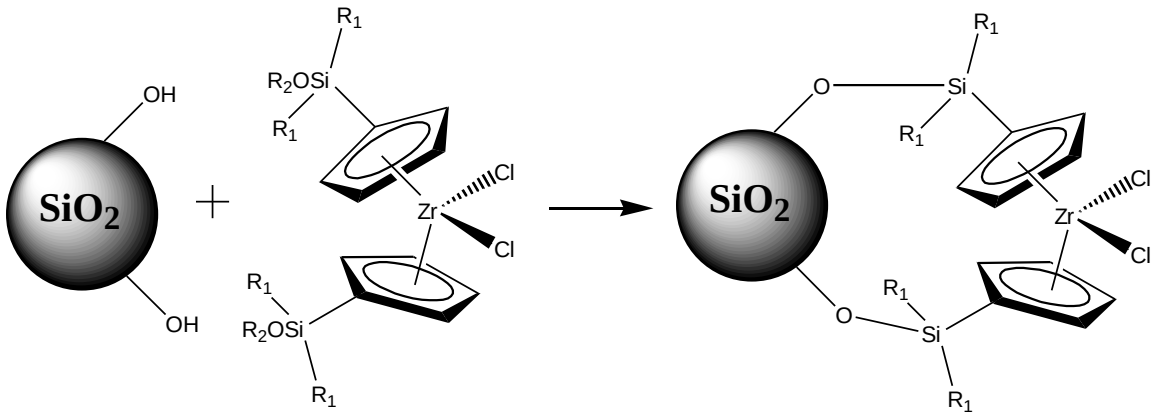

R_1, R_2 : H,CH_3,C_2H_5,higher alkyl chain

Scheme 2.6. Metallocene supporting by Method B.1 involves the reaction of hydroxyl groups on the silica surface and functional groups in the metallocene ligands (US Patent 5767300, 1998).

Method B.2 is a modification of Method B.1, where siloxane groups on the silica surface can react with other functional groups on the metallocene ligands to create a supported metallocene (US Patent 6114555, 2000). This method is attractive because byproducts such as water are not formed during catalyst supporting (Scheme 2.7).

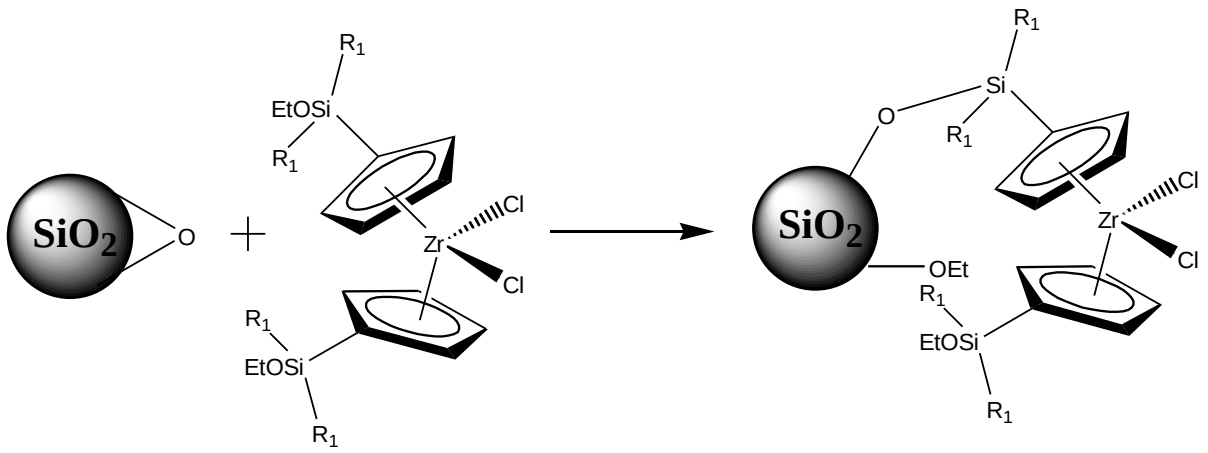

Scheme 2.7. Metallocene supporting by Method B.2 using siloxane groups (European Patent 839836, 1997).

Scheme 2.8 illustrates another supporting approach, the *consecutive-combined* method, where the transition metal complex is synthesized directly on the silica surface after its ligands are chemically bonded to the support surface (Ban et al., 1999; Iiskola et al., 1997; Soga et al., 1994a; Arai et al., 1997; Timonen et al., 1999; Uozumi et al., 1997). Even though this method reduces side reactions, the reported synthesis yields are commonly low, making it economically less attractive.

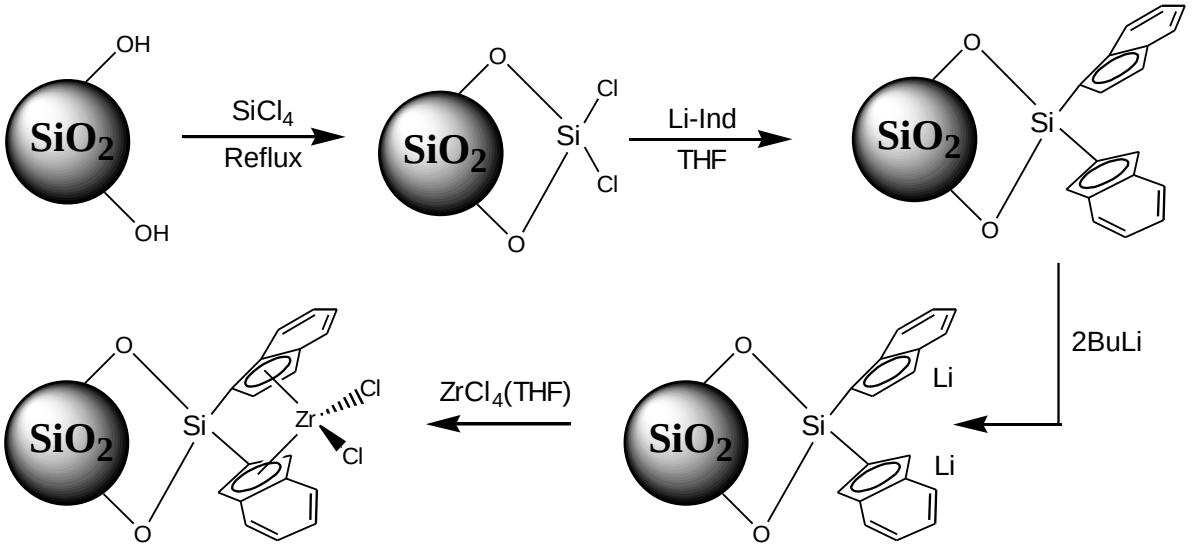

Scheme 2.8. Metallocene synthesis by the consecutive-combined method (Soga et al., 1994a).

In general, a supported catalyst is less active than its equivalent homogeneous catalyst. This may be due to the proximity of the catalyst to the support surface. Significant electrical and/or sterical effects caused by the presence of the support around the active sites may decrease the monomer insertion frequency or deactivate some of the catalytic sites. Spacer groups may be used to improve catalyst activity because they help reduce electronic and steric effects between support and catalyst, as illustrated in Figure 2.5 (Lee et al., 1999).

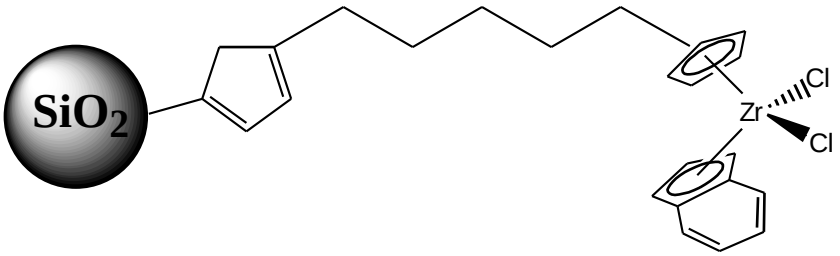

Figure 2.5. Metallocene catalyst supported through a spacer group (Lee et al., 1999).

Fairly extensive investigations regarding the effects of silica activation temperature, grafting temperature, and solvent type on supported catalyst activity were explored by Santos et al. (1999), but since the order of reactant addition and supporting conditions influence the activity of the resulting catalyst and the polymer microstructure, the comparison of the relative performances of supported metallocene catalysts prepared by many researchers is difficult to make.

2.2.3. Other Supporting Techniques

A technique that does not fall under any of the supporting methods described above is the *in situ supporting* method. In this procedure, a metallocene solution is contacted directly with MAO-modified silica in the polymerization reactor a few minutes prior to the beginning of the polymerization. In situ supporting eliminates the need for a separate catalyst supporting step, yielding catalysts that are activated by common alkylaluminums having good activities, and stable polymerization rates. They also make polymer particles with good morphology, high bulk density, and no reactor fouling, for the production of polyethylene and ethylene/1-hexene copolymers (Chu et al., 2000). However, because this method is hard to implement in continuous polymerization processes, it does not seem to be a viable alternative for commercial applications.

Another alternative route for depositing a dissolved substance onto a solid carrier is the *incipient wetness* method (Kamfjord et al., 1998). The underlying principle of the method is that only enough solution is added to fill the pores of the support, facilitating the uniform distribution of solute in the support pores. MAO-modified silica is prepared by this method

through the impregnation of silica with a MAO solution. The solvent, very commonly toluene, is evaporated from the support after a prescribed contact period, leaving behind MAO. Metallocene catalysts can also be immobilized following an analogous procedure. More interesting, metallocene catalysts can be dissolved in liquid comonomers (1-hexene, styrene, or 1,7-octadiene) and the monomer may be allowed to polymerize slowly within the support pores. The type of monomer used during the prepolymerization affects the overall catalyst activity, as well as the polymerization kinetic behavior. The prepolymerization step can be used to encapsulate the catalyst and may lead to higher catalyst activity and better particle morphology.

2.2.4. Silica Supported Nickel Diimine Catalysts

Many organic or inorganic materials may be used as supports for late transition metal catalysts; physical adsorption or covalent attachment methods can be applied as these techniques are common for metallocene systems. However, the activities reported using nickel diimine catalysts supported by Method A.2 were very low when compared to the equivalent homogeneous polymerizations (Alobaidi et al., 2003). It has been suggested that large molar excesses of alkylaluminum used to support and activate nickel diimine complexes may lead to catalyst deactivation by reduction of the Ni(II) sites (Peruch et al., 1999).

Preishuber-Pflugl and Brookhart showed that covalent bonding between Ni(II) diimine catalysts and supports permits the use of activators other than MAO and allows higher Ni(II) loadings on the support, leading to high activity. In addition, the catalyst is firmly

immobilized on the support surface, minimizing catalyst leaching and reactor fouling (Preishuber-Pflugl and Brookhart, 2002; Schrekker et al., 2006).

A cost reduction in catalyst production is achieved by using inexpensive alkylaluminum, such as ethylaluninum sesquichloride, instead of MAO. Polyethylene properties, including melting temperatures, molecular weight, and branch densities can be varied by modification of the *ortho*-aryl substituents in the catalyst (Schrekker et al., 2006).

2.2.5. Other Single-Site Catalysts Supported on Silica

Silica-supported 2,6-bis[1-(2,6-diisopropylphenylimino)ethyl]pyridine iron(II) chloride for ethylene polymerization is synthesized by the consecutive silica/MAO/catalyst reactions, and the possible supporting mechanism is shown in Scheme 2.9 (Ma et al., 2002). The supported catalyst had lower activity than the equivalent homogeneous catalyst; however, the supported catalyst made polymer with higher molecular weights and melting temperatures with lower MAO concentration.

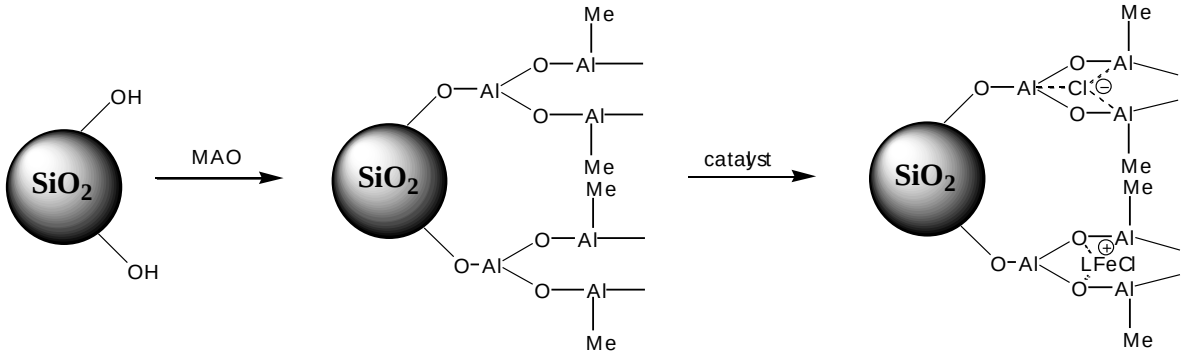

Scheme 2.9. Possible mechanism of supporting Fe(II) catalyst on silica (Ma et al., 2002).

Scheme 2.10 shows another example where the catalyst, bis(imino)pyridyl Co(II) and Fe(II) complexes, are anchored on silica by covalent bonds. The resulting catalyst produces polyethylene with high molecular weight after activation with MAO (Kim et al., 2003).

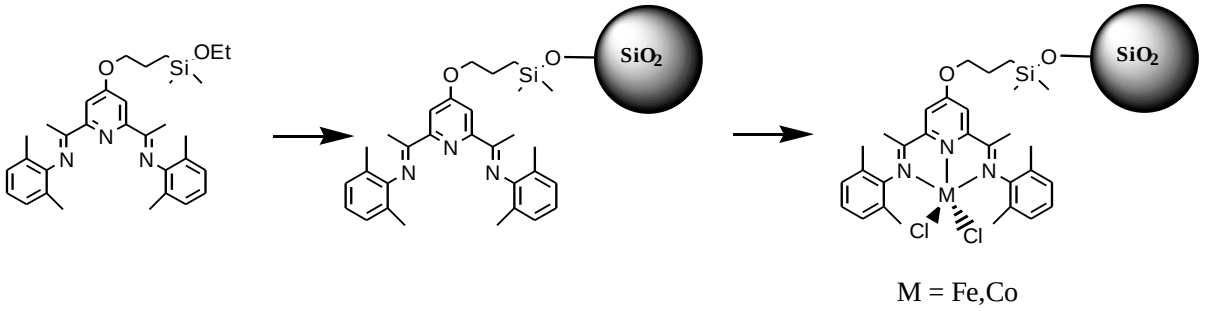

Scheme 2.10. Supported 2,6-Bis(imino)pyridyl Fe(II) and Co(II) catalysts (Kim et al., 2003).

2.3. Single-Site Catalysts Supported on Other Carriers

2.3.1. $MgCl_2$-Supported Single-Site Catalysts

Magnesium chloride is most widely used as a support for $TiCl_4$ Ziegler-Natta catalysts, greatly improving the activity and the stereospecificity of the catalyst. Magnesium chloride has also been used as a support for early and late transition metal catalysts (Przybyla et al., 1999; Santos et al., 1997; Severn and Chadwick, 2004a; Severn and Chadwick, 2004b; Soga et al., 1997).

Xu and coworkers (2006) reported that spherical $MgCl_2$ particles, obtained by the re-crystallization method using ethanol, and impregnated with Fe(II) and Ni(II) catalysts, had activities comparable to those of silica-supported catalysts, and the properties of the resultant polymers were similar also.

Nakayama and coworkers (2006) showed that $MgCl_2$-based compounds could act as good activator/supports for a bis(phenoxyimine) catalyst, known as FI catalysts (Figure 2.6). When compared to the corresponding homogeneous MAO activation system, the catalyst had high activity and made polymer with high molecular weight and well-controlled morphology.

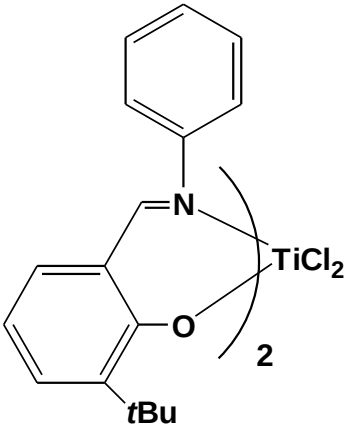

Figure 2.6. Structure of FI catalyst.

2.3.2. Clay-Supported Single-Site Catalysts

Clay minerals, such as montmorillonite and kaolin, may also be used as inorganic carriers for metallocene catalysts. The Si-OH groups on the clay surface react with Lewis acids to produce a cocatalyst for metallocene activation, as illustrated in Scheme 2.11. High molecular weight polymers were produced with clay-supported metallocenes. Montmorillonite supported metallocenes had higher activity than kaolin supported metallocenes, comparable to the activity obtained for ethylene polymerization with the equivalent homogeneous system (Weiss et al., 2002).

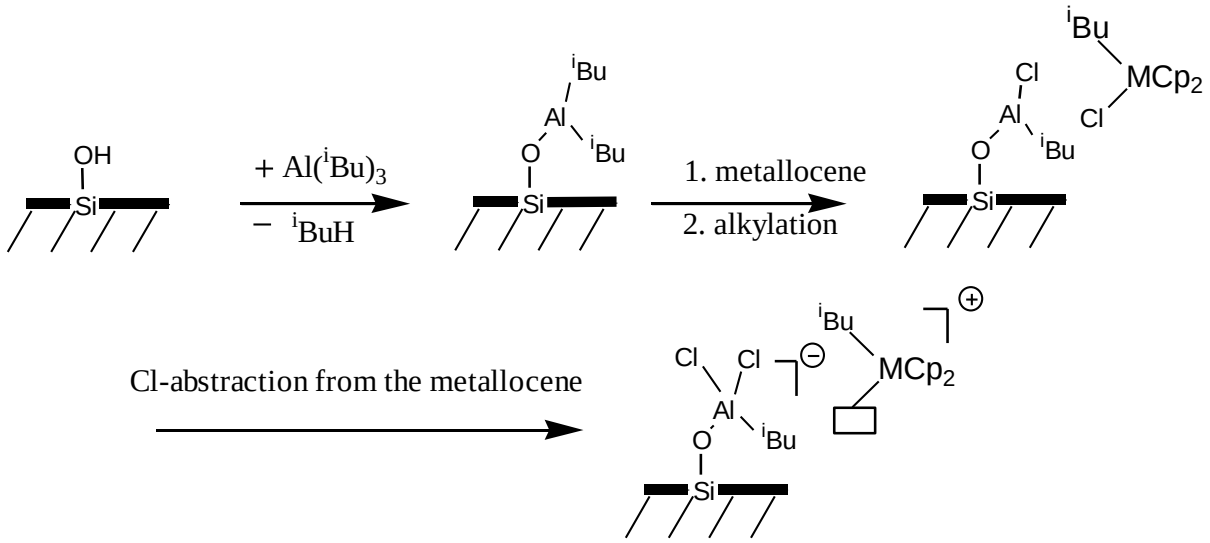

Scheme 2.11. Supporting a metallocene catalyst on a clay layer (M: Ti, Zr; Weiss et al., 2002).

It has been reported that the polymerization of olefins using MAO-activated coordination catalysts placed between silicate layers promote clay exfoliation (Bergman et al., 1999; Dubois et al., 2003; Heinemann et al., 1999; Todor et al., 1996). This approach is called in situ intercalative polymerization and can be used to make polyolefin-clay nanocomposites. Shin et al. prepared polyethylene clay nanocomposites using a similar in situ technique, where montmorillonite was intercalated with triisobutylaluminum and ω-undecylenyl alcohol before polymerization (Shin et al., 2003). The authors claimed that such modification allowed the copolymerization of ethylene with pendant double bonds of the ω-undecylenyl alcohol molecules that had been anchored to the clay surface, permitting the formation of clay-polyethylene hybrid nanocomposite via covalent bonding of the organic and inorganic phases.

A naturally existing clay mineral, palygorskite, which has the microstructure of nano-fibers, was also used to support Cp_2TiCl_2. After activation by MAO, the supported catalyst

initiated ethylene polymerization, resulting in the exfoliated dispersion of the nano-fibers into the polyethylene matrix. The obtained composites have increased rigidity, as reflected by almost doubling the polyethylene storage modulus at room temperature (Li et al., 2010).

2.3.3. Zeolite-Supported Single-Site Catalysts

Zeolites, typically aluminosilicates, are similar materials that are characterized by highly ordered crystalline structures, large surface areas, and defined pore geometries. Due to the presence of aluminum atoms, the zeolite framework possesses negative charges that are counterbalanced by cations. These cations are mobile, can be ion exchanged, and their nature, number and location influence the zeolite properties. Metallocenes have been heterogenized on various zeolites with varying levels of success (Ciardelli et al., 1999; Ko et al., 1999; Marques et al., 1997; Michelotti et al., 1998; Rahiala et al., 1999 Woo et al., 1995).

C. Covarroubias et al. supported metallocene onto modified zeolites, as shown in Scheme 2.12. These catalysts make polyethylenes with high crystallinity and narrow MWD. Furthermore, the strong Lewis acidity of the zeolite support was capable of activating the metallocene in the absence of MAO (Covarrubias et al., 2008).

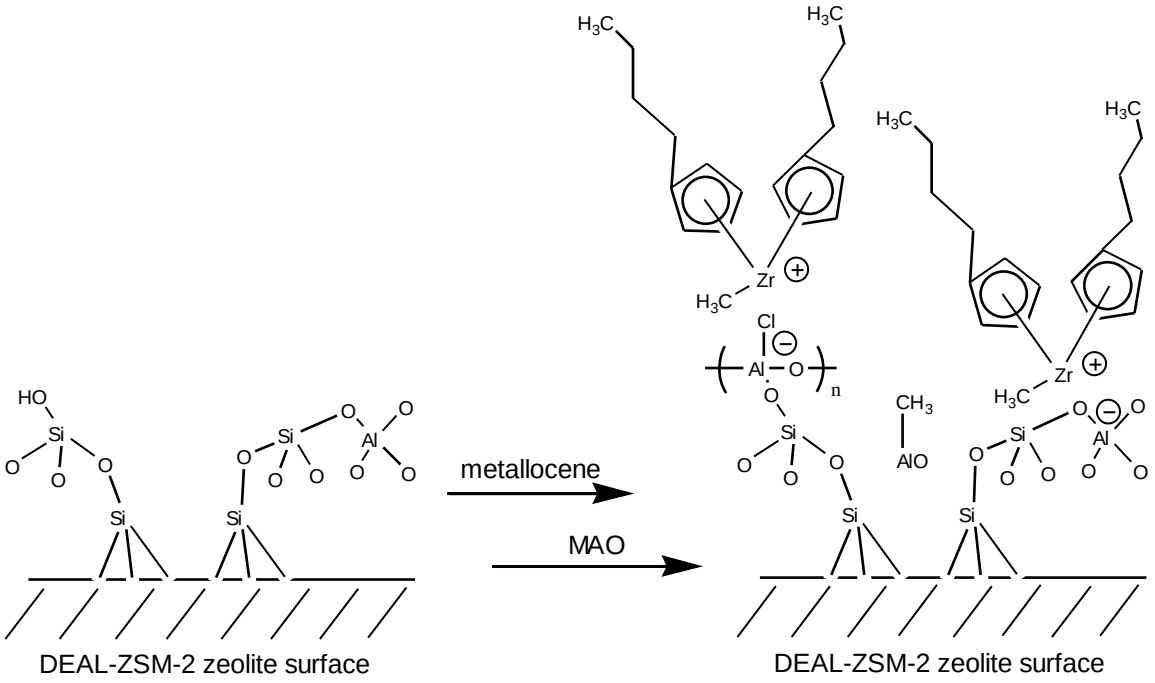

Scheme 2.12. Activation of metallocene catalysts on the DEAL-ZSM-2 zeolite surface.

2.3.4. Alumina-Supported Single-Site Catalysts

Soga and coworkers used alumina, usually γ-Al_2O_3, as a metallocene support, as well as analogous alkylaluminum-modified silica and alumina (Soga and Kaminaka, 1994; Soga et al., 1994c). Alumina supported systems were active with additional alkylaluminum as activator, but their silica analogues were inactive. They also supported $CpTiCl_3$ directly onto silica. The resulting catalyst was found to be active only when MAO was used as activator, while when $CpTiCl_3$ was supported directly onto alumina it yielded a catalyst active in the presence of both MAO and triisobutylaluminum. Treatment of the γ-Al_2O_3 support at the high temperature of 800°C increased the resulting catalytic activity. Furthermore, higher molecular

weight polymer was produced when the γ-Al_2O_3-supported catalyst was used than with the equivalent silica supported catalyst (Soga et al., 1994c).

Collins and coworkers (1992) reported that less metallocene decomposition during metallocene supporting was evident for alumina supports than for silica. Interestingly, metallocene decomposition was not observed for either material when silica and alumina had been previously modified with TMA. Moreover, the activities of the alumina-based systems were found to be comparable to those of silica-supported systems, despite the fact that the alumina used had relatively lower surface areas and total porosities.

2.3.5. Polymer-Supported Single-Site Catalysts

The primary advantage afforded by immobilizing metallocenes on polymeric materials is the lack of inorganic ash in the final product (Kitagawa et al., 1997; Sun et al., 1994). The most commonly used polymeric support materials are beads of crosslinked polystyrene, since they are porous and have large surface areas (Braca et al., 1996; Barret and Miguel, 1998; Liu et al., 1999; Meng et al., 1999; Nishida et al., 1995; Xu et al., 2000). Scheme 2.13 shows an example of polystyrene supported metallocene catalysts (Kitagawa et al., 1997).

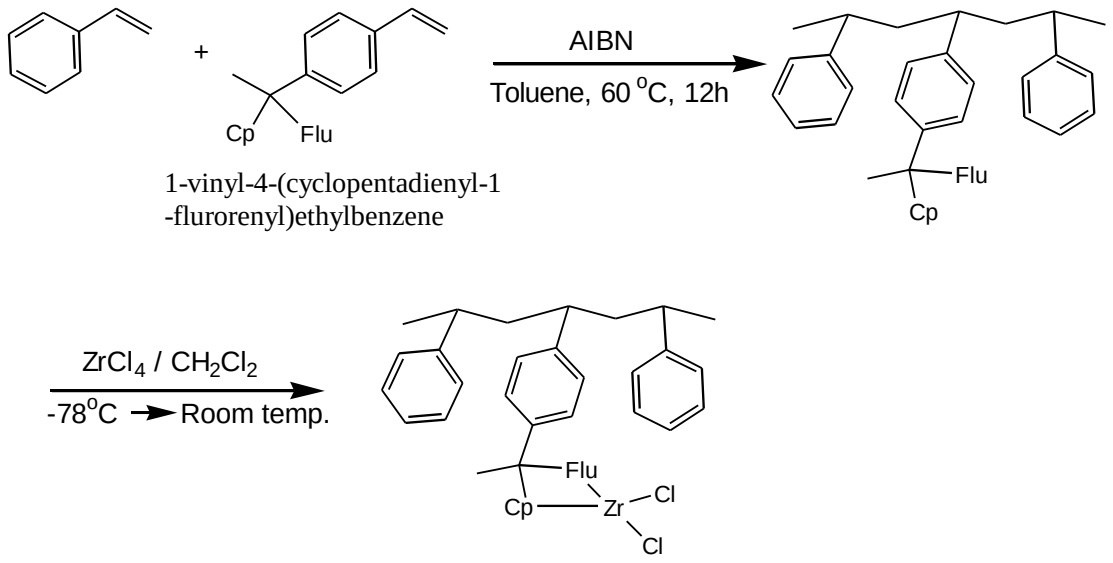

Scheme 2.13. Synthetic route of a polystyrene-supported catalyst (Kitagawa et al., 1997).

2.4. Supported Dual-Site Metallocene Catalysts and Hybrid Transition Metal Catalysts

In order to take advantage of commonly available polymerization plant infrastructure using a single reactor, the use of dual-site metallocene catalysts or hybrid transition metal catalyst systems, where each catalyst makes a polymer with its own unique properties, has considerable value (Hong et al., 2007; Soares and Kim, 2000). Single-site catalysts can be selected to make bimodal MWD resins even in a single reactor. Because metallocene catalysts produce polymers with narrow MWD and constant short chain branch (SCB) averages across the MWD, combining a metallocene that makes high molecular weight polymer with higher comonomer content and another metallocene that produces low molecular weight polymer with low comonomer content, permits the synthesis of resins with very useful properties (polyethylene pipe resins, for instance) that can ordinarily be made

only in two reactors in series. However, the characteristics of the two (or more) different catalysts having distinct chemical natures and polymerization kinetics in the same support/reactor must be taken carefully into account to create a well-balanced catalyst useful for industrial plant operation.

Hong and coworkers reported supported hybrid metallocene systems. $Me_2Si(C_5Me_4)(N\text{-}t\text{Bu})TiCl_2$ (CGC) has an open structure around the active sites, resulting in olefin copolymer production with high α-olefin content. On the other hand, $(n\text{BuCp})_2ZrCl_2$ makes low molecular weight polymer with low α-olefin content. Therefore, a hybrid catalyst using CGC/$(n\text{BuCp})_2ZrCl_2$ could make polyethylene with bimodal MWD and reverse comonomer incorporation.

Several studies of co-supporting metallocenes and conventional Ziegler-Natta catalysts have been reported (Cho et al., 1998; Chung et al., 1999; Forte et al., 2001; Park et al., 2006). Chung and coworkers (1999) synthesized Ziegler–Natta and metallocene hybrid catalysts supported onto colloidal silica using $MgCl_2$ solution as an initiator. The prepared bi-support was modified by treatment with alkylaluminum compounds, and the supported hybrid catalysts exhibited characteristics of both Ziegler–Natta and metallocene catalysts, such as a bimodal MWD. Cho and coworkers (1998) synthesized Ziegler-Natta/metallocene supported hybrid catalysts in order to control the molecular weight and MWD of polyethylene. Polymer reactor blends, having two melting temperatures and a bimodal MWD, are produced with this system because each individual catalyst makes polymers with distinct average properties.

2.5. Conclusion

From an industrial point of view, there is significant interest in supporting single-site catalysts on a variety of carriers, so they can be easily used in existing slurry and gas-phase processes. Indeed, most of the major polyolefin manufacturing companies already produce polymer grades using these types of catalysts. Since the combinations between catalyst types, support types, and supporting methods is practically infinite, several options exist for the synthesis of supported catalysts with novel characteristics.

Many supporting techniques have been developed to overcome the decrease in activity that generally happens upon supporting, to control polymer particle morphology, and to produce polymers with well-controlled properties for existing and new applications. Some supporting technologies also allow the use of single-site catalysts to make polyolefins with rather different properties, such as the preparation of nanocomposites by nanophase-dispersed supports into a polymer matrix. In addition, more sophisticated polymer microstructure designs are possible using catalysts such as hybrid metallocene/Ziegler-Natta and early/late transition metal catalysts, which can produce polyolefins with improved or entirely new applications.

Chapter 3 : Synthesis of Supported Nickel Diimine Catalysts for Ethylene Slurry Polymerization

3.1. Introduction

Many investigations using late transition metal catalysts for olefin polymerization have been reported since Brookhart and coworkers made their first high molecular weight polyethylene with bulky substituted aryl α-diimine nickel(II) complexes (Johnson et al., 1995). However, the activities reported using supported nickel diimine catalysts are very low compared to those of the equivalent homogeneous catalysts (Alobaidi et al., 2003). It seems that the large molar excess of alkylaluminum cocatalyst used to support and activate nickel diimine complexes may be responsible for this decrease in activity. Methylaluminoxane (MAO) is effective catalyst activator but requires Al/transition metal ratios that may vary from hundreds to thousands.

This chapter describes the preparation of supported nickel diimine catalysts to polymerize ethylene in a slurry reactor. The prepared catalysts had covalent bonds between the nickel diimine complexes and functional groups on the support surface, allowing higher

nickel loadings and leading to high activity, as well as stable catalyst immobilization on the support surface. Instead of commonly used aluminoxane activators, such as MAO, alternative bulky anionic borates were used in stoichiometric ratio to activate the catalyst, providing a more precisely defined catalyst system. The properties of the resultant polymers were controlled by the catalyst structure, type of activators, and polymerization conditions.

3.2. Experimental

3.2.1. Materials

All operations were performed under nitrogen (99.999 %, Praxair) using standard Schlenk techniques or inside a glove-box. Polymer grade ethylene (99.9 %, Praxair) and nitrogen were further purified by passing through columns packed with R3-11 copper catalyst, activated alumina and 3A/4A mixed molecular sieves. Materials for catalyst synthesis were purchased from Aldrich and used without further purification. MAO (10 wt. % in toluene), TMA (2 M in toluene) and TIBA (1 M in hexane) were purchased from Aldrich. Ethylaluminum sesquichloride (EASC, 97 %) was kindly donated by Akzo Nobel. Silica (XPO-2410 Grace Davison, average particle size 29 µm, total volatiles 0.85 %, surface area 304 m^2/g, pore volume 1.64 cc/g) was used as the catalyst support. Solvents for catalyst synthesis and polymerization were purified by passing through columns packed with activated alumina and molecular sieves (Zeolum Type F-9, Tosoh). All purified solvents were stored in Schlenk flasks with 3A/4A mixed molecular sieves. The borate activators, dimethylanilium tetrakis(pentafluorophenyl)borate **(B1)** and lithium tetrakis(pentafluorophenyl)borate *n*-etherate **(B2)** were purchased from Boulder Scientific.

3.2.2. Synthesis of Nickel Diimine Complexes

N1 and **N2** were synthesized following procedures published in the literature (Johnson et al., 1995; Preishuber-Pflugl and Brookhart, 2002), and **N3** was synthesized in a similar procedure with **N2**. Each synthetic route is described briefly below.

3.2.2.1. Nickel diimine complexes, 4-bis(2,6-diisopropylphenyl)acenaphthene nickel(II) dibromide (N1)

Acenaphthenequinone (1.5 g, 8.2 mmol), excess of 2,6-diisopropyl aniline (3.6 mL, 19.1 mmol) and 100 mL methanol as solvent were added to a 250 mL Schlenk flask. A volume of 1.5 mL formic acid as reaction catalyst was added dropwise. The mixture was stirred for 3 days at room temperature. The solid was filtered, washed three times with methanol, and then dried under vacuum. A dried orange powder (4.12 g, 84.4 % yield) was isolated at the end of the reaction.

Nickel(II) dibromide-ethyleneglycol dimethyl ether complex ($NiBr_2$(DME)) (0.622 g, 2.0 mmol) was added to a 250 mL Schlenk flask, then dissolved in 40 mL dichloromethane. Then, 1,4-bis(2,6-diisopropylphenyl)acenaphthene (1.0 g, 2.0 mmol) was added to a 100 mL Schlenk flask, and dissolved in 20 mL dichloromethane. This solution was transferred to the 250 mL flask using a cannula. The Ni(II) compound mixture was stirred for 3 days at room temperature, and two-thirds of the dichloromethane was removed by vacuum. A volume of 50 mL hexane as a non-solvent was added to this mixture and the final mixture was kept in the freezer (-15°C) overnight. The precipitated product was filtered, washed three times with cold hexane, and dried under vacuum. A dried dark red powder (1.26 g, 88 % yield) was isolated

and named **N1**. All procedures were conducted under nitrogen atmosphere. The synthetic route for catalyst synthesis is shown in Scheme 3.1. (Elemental Analysis **N1** ($C_{36}H_{40}N_2Br_2Ni$) (719.2): Calculated: C 60.1, H 5.6, N 3.9; Found: C 59.7, H 5.7, N 3.9).

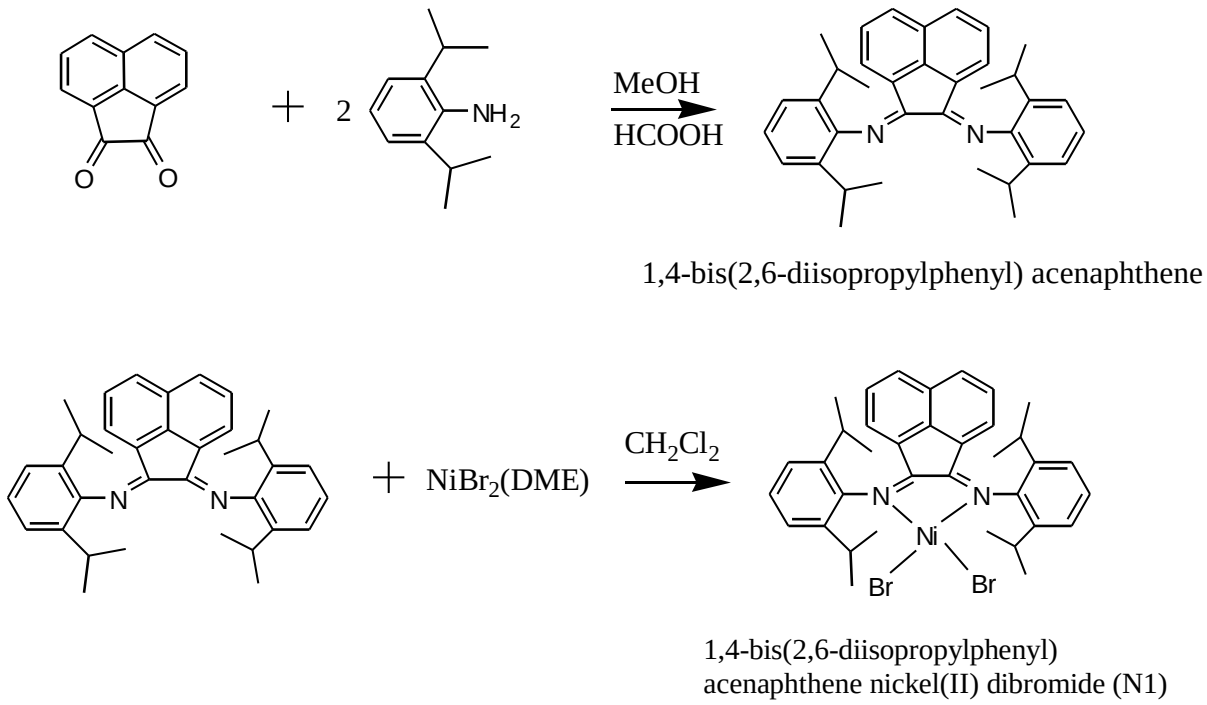

Scheme 3.1. Synthesis of 1,4-bis(2,6-diisopropylphenyl) acenaphthene nickel(II) dibromide (**N1**).

3.2.2.2. Bis(4-amino-2,3,5,6-tetramethylimino)acenaphthene nickel(II) dibromide (N2)

An amount of 8.2 mmol acenaphthenequinone, 30.0 mmol 2,3,5,6,-tetramethyl-phenylene-1,4-diamine, and 50 mL toluene as solvent were added to a 100 mL Schlenk flask.

A volume of 0.03 mL sulfuric acid as reaction catalyst was added dropwise to the flask. The mixture was stirred and refluxed for 3 hours. After the insoluble residue was filtered while still hot, the product was dried under vacuum. The dried powder was dissolved in 200 mL ethyl acetate, 400 mL hexane was added, and the mixture was stirred for 30 minutes. This solution was kept in the freezer at -15°C overnight. The precipitated product was filtered and washed with 50 mL cold hexane, and vacuum-dried overnight. A dried red powder (2.75 g, 71 % yield) was obtained.

An amount of 1.6 mmol nickel(II) dibromide-ethyleneglycol dimethylether complex ($NiBr_2$(DME)) and 1.8 mmol bis(4-amino-2,3,5,6-tetramethylimino)acenaphtene were added to a 50 mL Schlenk flask, then dissolved with 20 mL dichloromethane. After the mixture was stirred for 3 days at room temperature, dichloromethane was removed by vacuum. The product was washed three times with 20 mL diethyl ether each time, and then dried under vacuum. A dried black powder (0.8 g, 73 % yield) was isolated and named **N2**. The synthetic route for catalyst synthesis is shown in Scheme 3.2. (Elemental Analysis **N2**, $C_{32}H_{34}N_4Br_2Ni$ (695.6): Calculated: C 55.3, H 5.3, N 8.1; Found: C 55.0, H 5.2, N 8.0).

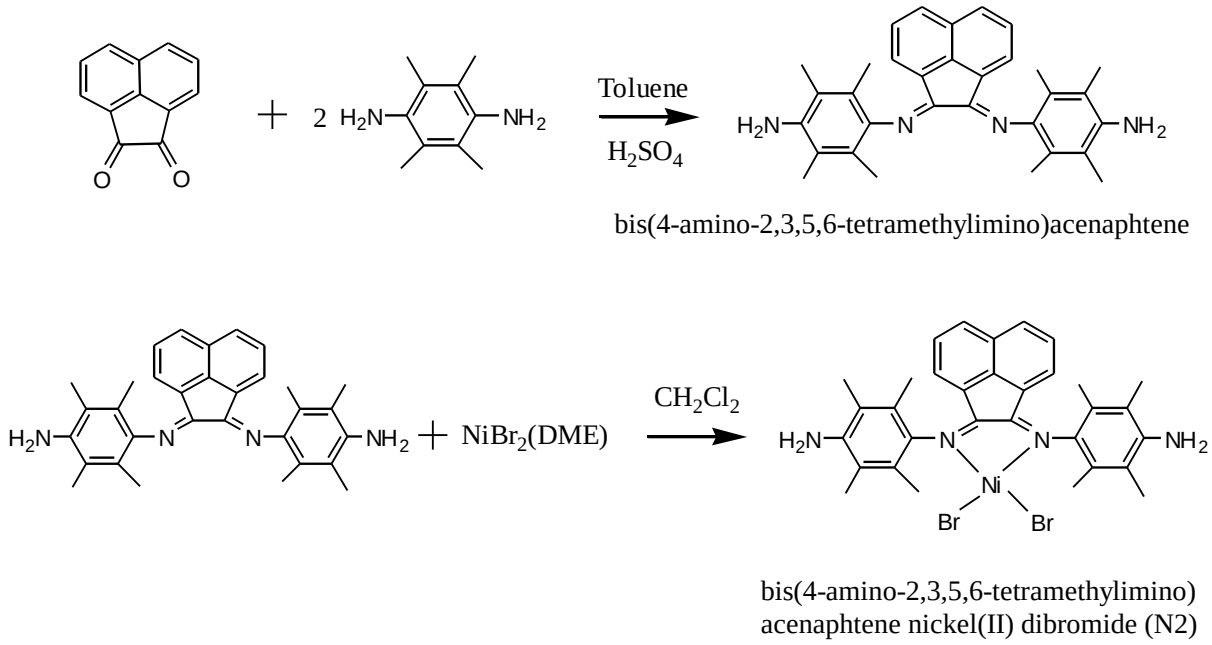

Scheme 3.2. Synthesis of bis(4-amino-2,3,5,6-tetramethylimino)acenaphtene nickel(II) dibromide (**N2**).

3.2.2.3. Synthesis of bis(4-amino-2,3,5,6-tetramethylimino)butane nickel(II) dibromide (N3)

An amount of 10 mmol 2,3 butanedione, 30.0 mmol 2,3,5,6,-tetramethyl-phenylene-1,4-diamine, and 50 mL benzene as solvent were added to a 100 mL Schlenk flask. A volume of 0.03 mL sulfuric acid as reaction catalyst was added dropwise to the flask. The mixture was stirred and refluxed for 3 hours. The insoluble residue was removed by filtration while still hot, and dried overnight under vacuum. A volume of 200 mL cold hexane was added to the flask containing the dried product and stirred for 2 hours. The solid fraction was filtered and

washed with 100 mL cold hexane, and vacuum-dried overnight. A dried yellow powder (2.90 g, 77 % yield) was obtained.

An amount of 1.6 mmol nickel(II) dibromide-ethyleneglycol dimethylether complex ($NiBr_2$(DME)) and 1.8 mmol bis(4-amino-2,3,5,6-tetramethylimino)butane were added to a 50 mL Schlenk flask, then dissolved with 20 mL dichloromethane. After the mixture was stirred for 3 days at room temperature, dichloromethane was removed by vacuum. The product was washed three times with 20 mL diethyl ether each time, and then dried under vacuum. A dried brown powder (0.7 g, 67 % yield) was isolated and named **N3**. The synthetic route for catalyst synthesis is shown in Scheme 3.3. (Elemental Analysis **N3**, $C_{24}H_{34}N_4Br_2Ni$ (599.5): Calculated: C 48.1, H 6.1, N 9.3; Found: C 47.8, H 6.2, N 9.6).

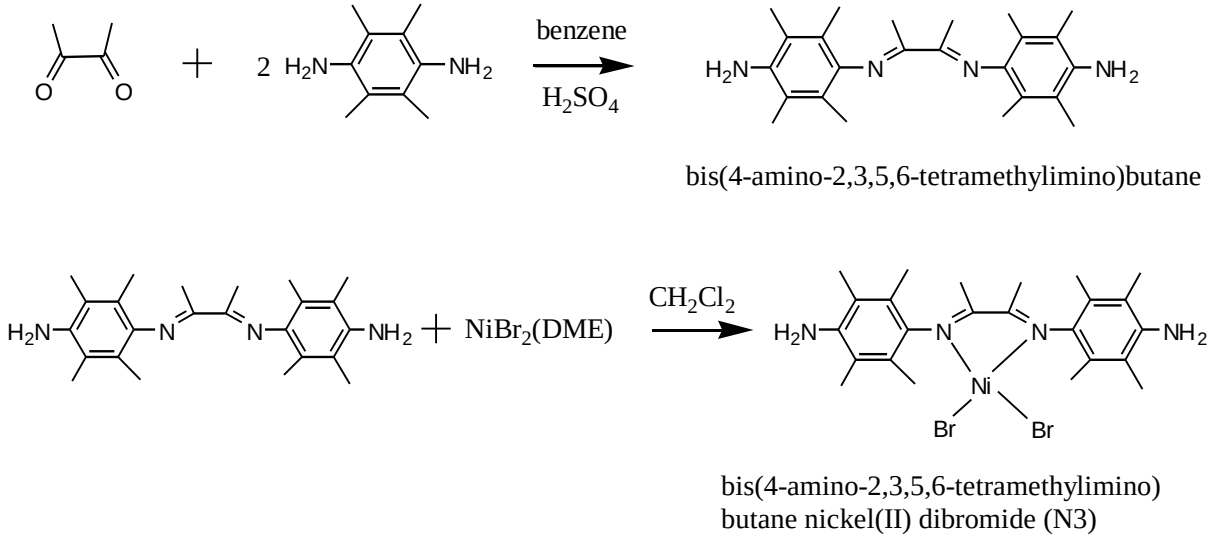

Scheme 3.3. Synthesis of bis(4-amino-2,3,5,6-tetramethylimino)butane nickel(II) dibromide (**N3**).

Finally, the structures of the two borate activators investigated in this study are shown in Figure 3.1.

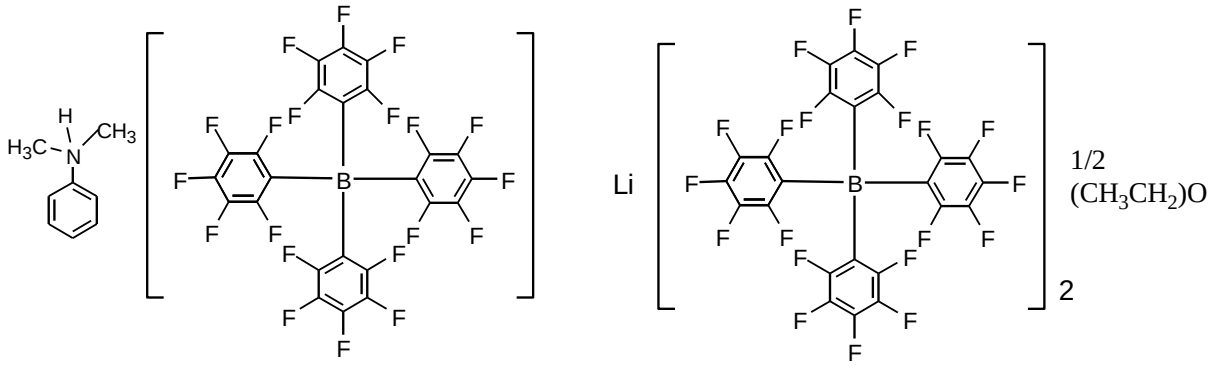

B1 B2

Figure 3.1. Borates structures: Dimethylanilium tetrakis(pentafluorophenyl)borate (**B1**), Lithium tetrakis(pentafluorophenyl)borate n-etherate (**B2**).

3.2.3. Synthesis of Supported Nickel Diimine Catalysts

3.2.3.1. Silica-supported 1,4-bis(2,6-diisopropylphenyl)acenaphthene nickel(II) dibromide (N1MS, N1TS)

One gram of silica XPO 2410 and 20 mL toluene were introduced in a dried 225 mL glass reactor equipped with a mechanical stirrer (Lab-Crest Glass Pressure Reaction Vessels, Andrews Glass Co.). The reactor was heated to 60°C at a stirring rate of 200 rpm, then 20 mmol MAO was slowly added and reacted for 15 hours. After stopping the stirrer, the supernatant liquid was removed with a cannula. The product was washed three times with 20 mL toluene, and finally heated to 30°C under 200 rpm. An amount of 0.14 mmol **N1** was

added to the reactor with 20 mL toluene, and reacted for 3 days. The produced supported catalyst was washed with 20 mL toluene until a colorless liquid appeared, and finally dried under vacuum. The supported catalyst was named **N1MS**. **N1TS** was synthesized according to a similar procedure, but 20 mmol TMA was used instead of MAO.

3.2.3.2. Silica-supported bis(4-amino-2,3,5,6-tetramethylimino)acenaphtene nickel(II) dibromide (N2MS, N2TS) and Silica-supported bis(4-amino-2,3,5,6-tetramethylimino)butane nickel(II) dibromide (N3TS)

Following the procedure described above, the silica support was treated with MAO, and then an amount of 0.14 mmol **N2** was added to the reactor with 20 mL dichloromethane, and reacted for 1 day. The produced supported catalyst was filtered, washed with 20 mL dichloromethane until a colorless liquid appeared, and then dried under vacuum. The product was named **N2MS**. **N2TS** was synthesized according to the same procedure, but 20 mmol TMA was used instead of MAO.

N3TS was synthesized according to a same procedure used to make **N2TS**, but **N3** was used in place of **N2**.

Figure 3.2 shows the structure of **N1TS** and **N2TS**. The complex in Figure 3.2.a was synthesized through physical adsorption of **N1** and TMA, and that in Figure 3.2.b was synthesized through covalent bonding between the functional groups of **N2** and TMA.

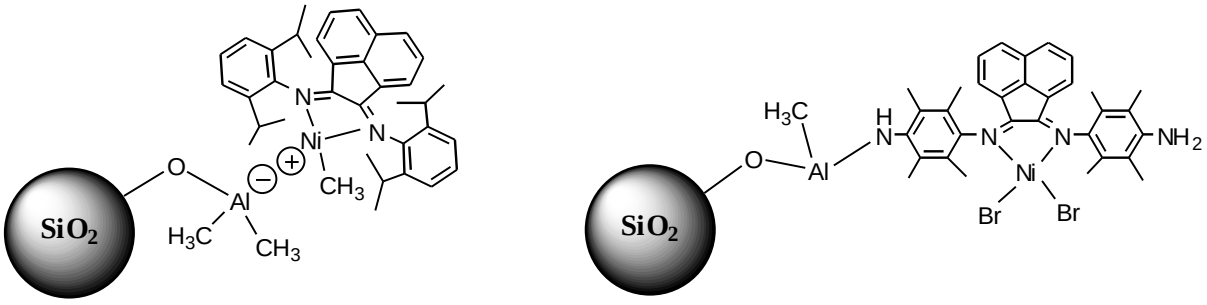

(a) (b)

Figure 3.2. Structure of supported nickel diimine catalysts: a) **N1TS**; b) **N2TS**.

3.2.3.3. Silica-supported bis(4-amino-2,3,5,6-tetramethylimino)acenaphtene nickel(II) dibromide with borate activator (N2B1TS-a, N2B1TS, N2B2TS) and silica-supported bis(4-amino-2,3,5,6-tetramethylimino)butane nickel(II) dibromide with borate activator (N3B1TS)

The procedure for **N2TS** supporting was followed, but using 12 mmol TMA and 0.07 mmol **N2**. The product was reacted with an amount of 0.07 mmol **B1** (**B1/N2** mole ratio 1) and was added to the reactor with 20 mL dichloromethane and reacted for 3 hours. The product was dried under vacuum without washing. The final catalyst was named **N2B1TS-a**. **N2B1TS** was synthesized according to the same procedure used to make **N2B1TS-a,** but 0.14 mmol **B1** (**B1**/**N2** mole ratio 2) was used. Similarly, **N2B2TS** was synthesized according to the same procedure for **N2B1TS**, but 0.14 mmol **B2** (**B2**/**N2** mole ratio 2) was used.

N3B1TS was synthesized according to the same procedure used for **N2B1TS**, but **N3** was used in place of **N2**.

3.2.4. Characterization of Supported Nickel Diimine Catalysts

Ni and Al contents on the supported nickel diimine catalysts were measured by inductively coupled plasma-optical emission spectroscopy (ICP, Teledyne Leeman Labs, Prodigy High Dispersion ICP). A mass of 20 mg of supported nickel diimine catalyst was dissolved in 10 mL 3N HNO_3 solution and the solution was diluted with distilled water prior to analysis.

3.2.5. Polymerization

Polymerizations were carried out in a 500 mL semi-batch reactor (Zipperclave, Autoclave Engineers Inc.) equipped with a mass flow controller and a temperature control unit consisting of a cooling coil and an electric heater. The polymerization temperature was maintained within ± 0.2^{o}C of the set point. Prior to each polymerization, the reactor was purged five times with 200 psig nitrogen, then heated to 120°C under vacuum, and purged again to the set point temperature under nitrogen flow. To completely remove residual moisture, 0.3 g TIBA (1 M in toluene) with 50 mL toluene or hexane was transferred to the reactor. Then, the reactor stirrer was turned on to 1000 rpm for 5 minutes. The reactor was washed again with 100 mL of solvent. After that, 200 mL solvent and the external activator (MAO or EASC) or scavenger TMA were transferred to the reactor, the reactor was stabilized at the set point temperature and fed with ethylene under a stirring rate of 1000 rpm. When the set point temperature and ethylene saturation were attained, the catalyst solution (**N1** with toluene, **N2** and **N3** with dichloromethane), or supported nickel diimine catalysts slurry with toluene or hexane were injected into the reactor. The polymerization was performed with a

continuous ethylene flow to meet the desired pressure. At the end of the polymerization time, the reactor was rapidly vented and the obtained polymer was precipitated and washed with acidified ethanol, then filtered and dried under vacuum. To get reliable polymerization results, reproducibility test were performed using unsupported catalyst systems. When the catalyst activities were within 5 % differences, other runs were performed with same solvent and ethylene.

3.2.6. Polymer Characterization

The catalyst activity was calculated as the mass of polymer product divided by the number of moles of nickel per hour. The melting temperature of the obtained polymer was characterized using differential scanning calorimetry (DSC, TA Instruments Q2000). The second scan was done at a heating rate of 10°C/min and used to characterize the sample. Molecular weight averages and distributions were determined by high-temperature gel permeation chromatography (GPC, Polymer Char). Samples were dissolved at 145°C with 1,2,4-trichlorobenzene and passed through three linear Polymer Laboratories columns which were calibrated with polystyrene standards and operated with a flow rate of 1 mL/min. SCBD was determined by crystallization analysis fractionation (CRYSTAF, Polymer Char). Samples were dissolved at 160°C for 30 minutes, followed by 60 minutes of equilibration at 95°C. The cooling rate during crystallization was 0.1^{o}C/min, from 95°C to 30°C. A scanning electron microscope (SEM, Leo Electron Microscopy LEO 1530) was used to investigate the morphology of catalyst and polymer particles. The samples were placed on the conductive tapes on the aluminum pan and were coated in 10 nm thick gold film using high vacuum sputter.

3.3. Results and Discussion

3.3.1. Supporting Efficiency of Supported Nickel Diimine Catalysts

Table 3.1 summarizes the components and the ICP results of all supported nickel diimine catalysts. Most of the Ni was deposited onto the silica support, but supporting efficiencies for Al were much lower, especially when TMA was used. It is reasonable to speculate that the alkylaluminum molecules first react with the hydroxyl groups available on the silica support and the remaining excess molecules are then physically adsorbed onto the surface.

Table 3.1. Description of supported nickel diimine catalysts.

Name	Components			ICP Results		Supporting Efficiency	
	Nickel diimine complex (mmol)	Alkyl aluminum (mmol)	Internal activator (mmol)	Ni (mmol/g catalyst)	Al (mmol/g catalyst)	Ni [a)] (wt.-%)	Al [b)] (wt.-%)
N1MS	N1 0.14	MAO 20	Not used	0.122	2.831	83.3	31.6
N1TS	N1 0.14	TMA 20	Not used	0.138	1.283	100	16.5
N2MS	N2 0.14	MAO 20	Not used	0.101	2.196	99.0	28.0
N2TS	N2 0.14	TMA 20	Not used	0.113	1.123	100	14.0
N3TS	N3 0.14	TMA 20	Not used	0.116	1.069	99.0	12.6
N2B1TS-a	N2 0.07	TMA 12	B1 0.07	0.058	0.761	98.6	11.7
N2B1TS	N2 0.07	TMA 12	B1 0.14	0.052	0.762	93.7	13.6
N2B2TS	N2 0.07	TMA 12	B2 0.14	0.054	0.818	97.2	13.5
N3B1TS	N3 0.07	TMA 12	B1 0.14	0.053	0.918	96.4	15.3

Support: Silica XPO2410 1gram.

[a)] Calculated on ICP results of Al deposition.

[b)] Calculated on assumption of 100 % Ni deposition.

3.3.2. Ethylene Polymerization Using Homogeneous Nickel Diimine Catalysts

Ethylene polymerizations using homogenous nickel diimine catalysts were conducted under various reaction conditions to set a reference for the polymerizations using supported nickel diimine catalysts. Table 3.2 summarizes the results of these polymerizations.

The catalyst activity was higher at low temperatures (30°C) and high ethylene pressures. The catalyst deactivation rate is much faster at high temperatures and the polymerization rate is proportional to monomer pressure, as generally expected. **N1** was more active and produced polymer with higher molecular weight averages than **N2** and **N3**. However, **N1** deactivates rapidly at 60°C (Kim et al., 1998). Increasing ethylene pressure or decreasing the polymerization temperature led to polymer with higher melting temperature. **N1** made polyethylene with lower melting temperature than **N2** and **N3**. This behavior indicates that **N1** is more prone to chain walking than **N2** and **N3** under the same polymerization conditions.

The catalyst system obtained from activating **N1** with EASC had good activity and produced polyethylene with lower melting temperature and lower molecular weight average than those made with MAO (Runs 1 and 2, Table 3.2).

Table 3.2. Ethylene polymerization results using homogeneous nickel diimine complexes.

Run	Polymerization Conditions				Results			
	Complexes [a)]	Activator	Pressure (Psig)	Temp. (^{o}C)	Activity [b)]	T_m (^{o}C)	M_w (g/mol ×10^{-3})	M_w/M_n
1	N1	MAO	150	30	59300	113.7	667	2.4
2	N1	EASC	150	30	55100	104.0	565	2.6
3	N1	MAO	150	60	25400	n.d.[c)]	214	2.1
4	N1	MAO	50	30	14200	86.3	433	1.6
5	N1	MAO	220	30	43500	114.4	671	2.8
6	N2	MAO	150	30	23200	132.5	117	3.1
7	N2	MAO	150	60	25300	123.0	53	3.5
8	N2	EASC	150	60	44000	116.5	57	2.8
9	N2	EASC	50	60	8700	92.8	31	2.5
10	N2	EASC	150	30	62300	126.5	153	3.6
11	N3	EASC	150	60	7600	122.5	65	3.8
12	N3	EASC	150	30	23600	126.4	139	2.6
13	N3	EASC	50	30	14900	122.5	122	2.8

Polymerization conditions: catalyst 0.5 μmol, Al (MAO or EASC)/Ni ratio 3000, solvent 200 mL toluene, time 15 min.

[a)] **N1**: 1,4-bis(2,6-diisopropylphenyl) acenaphthene nickel(II) dibromide, 1 M toluene solution.

N2: bis(4-amino-2,3,5,6-tetramethylimino)acenaphthene nickel(II) dibromide, 1 M dichloromethane solution.

N3: bis(4-amino-2,3,5,6-tetramethylimino)butane nickel(II) dibromide, 1 M dichloromethane solution.

[b)] Activity in kg PE/(mol Ni × hour).

[c)] not detected.

3.3.3. Ethylene Polymerization Using Physisorbed Supported Nickel Diimine Catalysts

Table 3.3 shows the ethylene polymerization results using supported **N1** catalysts. Polyethylene samples made with the supported catalyst had different microstructures from those made with the homogeneous catalyst. Supported **N1** had lower catalyst activity and made polymer with higher melting temperature, although the polymerization trends were the same with respect to ethylene pressure and temperature. The drastic reduction in the activity of the supported catalyst may be attributed to the steric hindrance of the support (Hong et al., 2007). Moreover, steric effects between support and catalyst depress chain walking rates, producing polymer chains with lower SCB content and higher melting temperatures.

Polyethylene samples made in Runs 1, 4, 6 and 7 (Table 3.3) had two melting peaks. Probably, some of the catalyst sites were either extracted from, or loosely anchored to, the support, producing two kinds of active sites during the polymerization: active sites immobilized on the support made polyethylene with lower SCB frequency and higher melting temperature, while extracted (or loosely supported) active sites made chains with higher SCB content and lower melting temperature. On the other hand, the polymer made in Runs 3 and 5 had only one low melting temperature peak, which could be caused by the low ethylene pressure (Run 3, Table 3.3) or high polymerization temperature (Run 5, Table 3.3) used in these polymerizations.

As reported by Brookhart and co-workers, nickel diimine catalysts activated with EASC had high catalyst activities (WO 094302, 2006); when **N1TS** was activated with EASC,

remarkable high activities were observed (Run 7, Table 3.3). EASC was found to be a much more efficient external activator than MAO for this system.

Table 3.3. Ethylene polymerization results using physisorbed supported nickel diimine catalysts.

Run	Polymerization Conditions				Results	
	Catalyst	External Activator	Pressure (Psig)	Temperature (^{o}C)	Activity [a)]	T_m (^{o}C)
1	N1MS	MAO	150	30	850	113.9,126.2
2	N1MS	MAO	150	60	530	n. d.[b)]
3	N1TS	MAO	50	30	110	117.8
4	N1TS	MAO	150	30	590	111.9,126.6
5	N1TS	MAO	150	60	230	118.1
6	N1TS	TMA	150	30	180	115.7,121.6
7	N1TS	EASC	150	30	2080	109.7,118.8

Polymerization conditions: catalyst 50 mg, external activator MAO (2 mmol), solvent 200 mL toluene, time 15 min.

[a)] Activity in kg PE/(mol Ni × hour).

[b)] not detected.

Comparative CRYSTAF results are shown in Figure 3.3. Polyethylene made with the homogeneous **N1** (Run 1, Table 3.2) had a broad unimodal SCBD in the temperature range 40-70°C. For the **N1TS** (Run 4, Table 3.3), the SCBD was trimodal and broader (40-90°C), with a high crystalline peak (>75°C). It seems that the lowest melting temperature peak came from extracted or loosely supported nickel diimine sites, since this peak location coincides with that of the homogeneous system. The other two peaks at higher temperature are likely

for polyethylene made by sites supported in different configurations or locations on the silica surface.

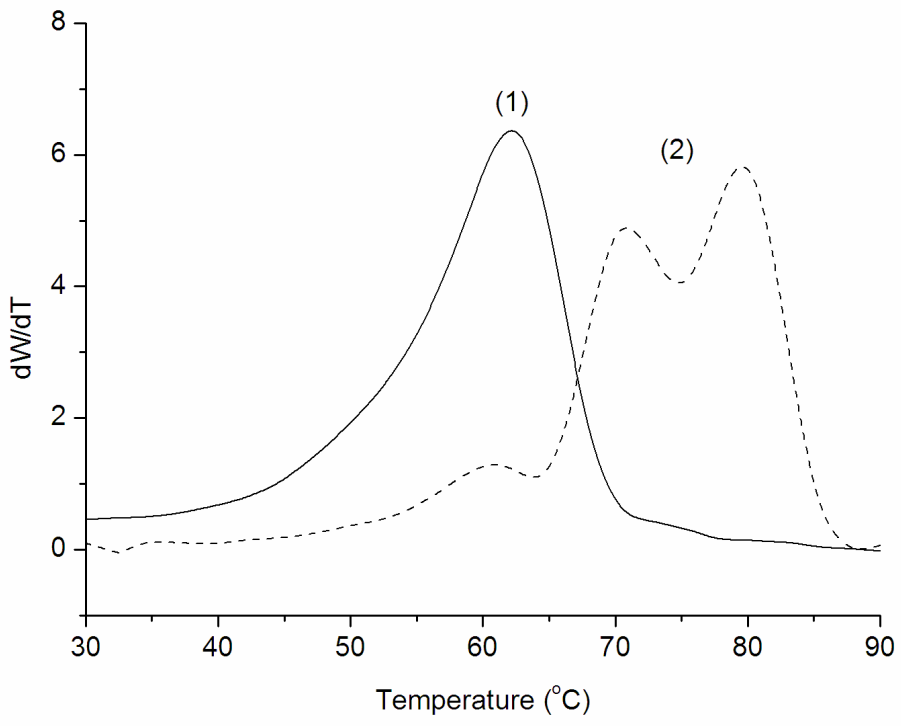

Figure 3.3. Cyrstaf (SCBD) profiles of polyethylene made with homogenous and supported nickel diimine catalyst: (1) **N1** (Run 1, Table 3.2); (2) **N1TS** (Run 4, Table 3.3).

Figure 3.4 shows the particle morphology for polymers made with **N1TS** (Run 4, Table 3.3); other polymers using supported **N1** catalysts had similar poor morphologies. It seems that **N1** is partially extracted from the silica surface during the polymerization due to the weak ionic interactions between active site and support surface, and the obtained "soft" polymer particles (because of the SCBs resulting from chain walking during polymerization) are easily agglomerated to one another.

Figure 3.4. Morphology of polymer made with **N1TS** (Run 4, Table 3.3).

3.3.4. Ethylene Polymerization Using Covalently-Attached Supported Nickel Diimine Catalysts

Several supported **N2** and **N3** catalysts were prepared through chemical bonding between the functional groups in the ligands of nickel diimine complexes and TMA-treated silica. Ethylene polymerization results using these catalysts are summarized in Table 3.4.

Table 3.4. Ethylene polymerization results using covalently-attached supported nickel diimine catalysts.

Run	Polymerization Conditions					Results				
	Catalyst	Cat. (mg)	Solvent	Pres. (Psig)	Temp. (^{o}C)	Yield (g)	Activity [a)]	T_m (^{o}C)	M_w (g/mol $\times 10^{-3}$)	M_w/M_n
1	N2MS	30	toluene	150	30	2.1	2860	132.1	218	5.7
2	N2MS	30	toluene	150	30	1.3	1800	131.9	238	6.1
3	N2MS	20	toluene	150	60	6.8	14000	127.2	163	6.9
4	N2MS	15	toluene	150	80	2.5	5940	126.0	104	6.2
5	N2TS	6	toluene	150	60	6.5	37800	127.8	143	6.7
6	N2TS	6	hexane	150	60	3.9	24900	127.0	130	6.1
7	N2TS	10	hexane	50	60	2.8	10200	125.5	115	5.9
8	N3TS	15	hexane	150	60	4.0	9200	124.4	113	5.2
9	N3TS	11	hexane	150	30	1.7	5200	129.2	161	4.0
10	N3TS	15	hexane	50	60	1.6	3680	122.5	150	5.3
11	N3TS	15	hexane	50	30	1.1	2550	125.6	140	4.1

Polymerization conditions: external activator 2 mmol EASC except 2 mmol MAO in Run 2, time 15 min.

[a)] Activity in kg PE/(mol Ni × hour).

In contrast to supported **N1** catalysts, the activities of supported **N2** and **N3** catalysts were much higher and the polymer particles had good morphologies. **N1** is physisorbed onto the silica surface, which may cause significant steric hindrance and electronic interference of the bulky silica surface on ethylene insertion rates. However, **N2** and **N3** are likely supported through their NH_2 functional groups, creating covalent chemical bonds with the silica surface. The tethered group linking the support to the catalyst ligand permits the formation of highly

active and strongly immobilized metal centers (Schneider et al., 2001). GPC results showed that supported **N2** and **N3** catalysts made polyethylene with higher molecular weight averages, broader molecular weight distributions, and higher melting temperature peaks than the equivalent polymers produced with homogeneous **N2** and **N3**.

N2MS showed maximum activity and made polymer with highest molecular weight averages at 60°C, followed by a decrease of both properties at higher temperatures. Surprisingly, the activity of **N2TS** at 60°C (Run 6, Table 3.4) was similar to that of the homogeneous **N2** (Run 7, Table 3.2). Figure 3.5 shows that **N2TS** activated more slowly and had a longer life time than **N2**. This indicates that more stable active centers are generated in the supported nickel diimine catalyst system, resulting in higher overall activity and molecular weight averages. In addition, it can be hypothesized that **N3** active sites that were unstable at 60°C were converted to stable active sites after supporting (Run 11, Table 3.2 and Run 8, Table 3.4).

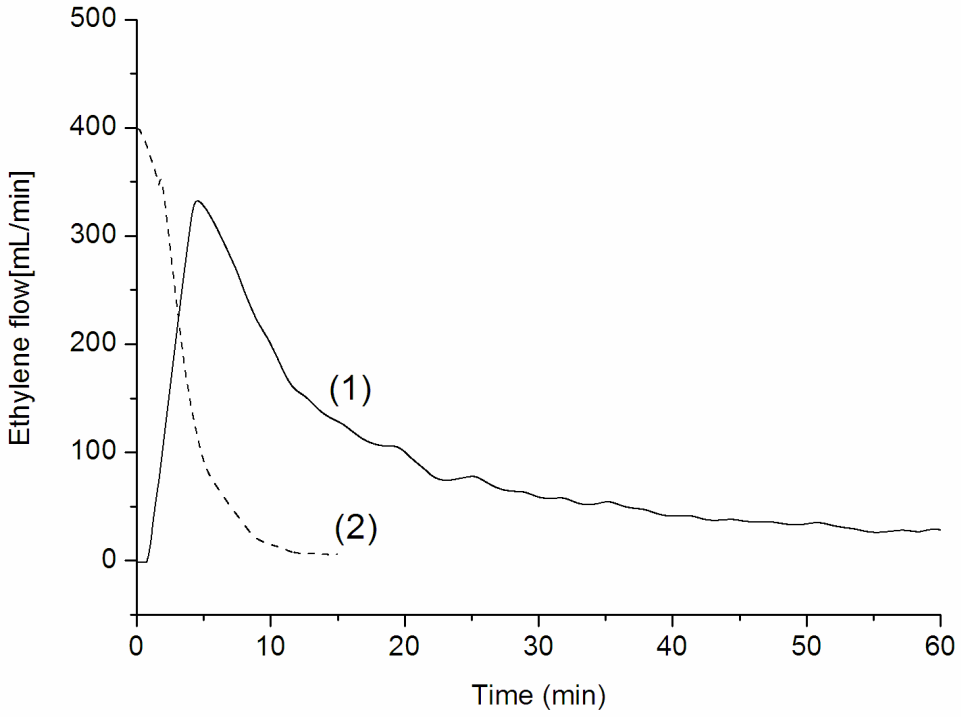

Figure 3.5. Comparison of ethylene flow as a function of polymerization time for **N2** and **N2TS**: (1) Supported nickel diimine catalyst system (**N2TS**, Run 5, Table 3.4), (2) Homogenous nickel diimine complex system (**N2**, Run 7, Table 3.2).

Runs 1 and 2 in Table 3.4 were performed at the same conditions to compare the effect of different external activator types. EASC led to a catalyst with higher activity than MAO. When the effect of alkylaluminum within the supported catalyst was considered (Runs 3 and 5, Table 3.4), TMA gave higher catalyst activity than MAO. This indicates that supported nickel diimine catalysts that do not use MAO have great potential to reduce the cost of catalyst production. Some particle agglomeration was observed when supported **N2** was used to polymerize ethylene in toluene slurry, probably because low molecular weight chains with high SCB frequencies were extracted by the solvent. On the other hand, polymer particles

made in hexane slurry had good morphology, but the catalyst activity was lower (Run 5 and 6, Table 3.4).

Polymerization results under different concentrations of external activators are shown in Table 3.5. The catalyst activity was highest for Al/Ni molar ratios of 2000 (Run 3, Table 3.5), then slightly decreased with increasing concentrations of external activator. These results may be tentatively attributed to the fact that the amount of alkylaluminum within the supported catalyst is not enough for fully activating the catalyst; the activator may also be required as a scavenger of impurities or to stabilize the active sites.

Table 3.5. Comparison of ethylene polymerization results with different Al/Ni ratios.

Run	Polymerization Conditions			Results		
	Catalyst	Ni amount (μmol)	Al/Ni	Yield (g)	Activity [a)]	T_m (°C)
1[b)]	N2TS	3.8	0	1.9	1100	128.0
2	N2TS	0.70	1000	1.8	10100	127.9
3	N2TS	0.70	2000	5.3	30200	127.4
4	N2TS	0.73	3000	4.9	27000	127.1
5	N2TS	0.63	6000	3.9	24900	127.0

Polymerization conditions: external activator EASC, solvent 200 mL hexane, temperature 60°C, time 15 min.

[a)] Activity in kg PE/(mol Ni × hour).

[b)] 0.2 mmol TMA added as a scavenger.

SEM micrographs of **N2TS** catalyst and polymer particles are shown in Figure 3.6. The spherical shapes of the polymer particles resemble that of the catalyst particles, indicating good replication of the catalyst support morphology.

a)

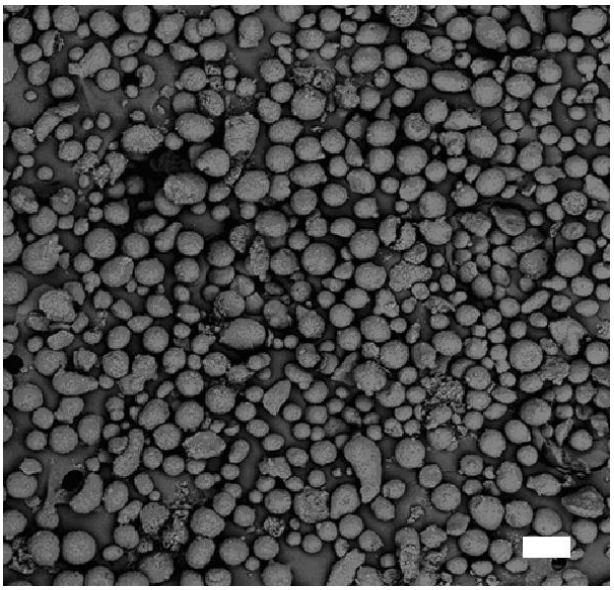

b)

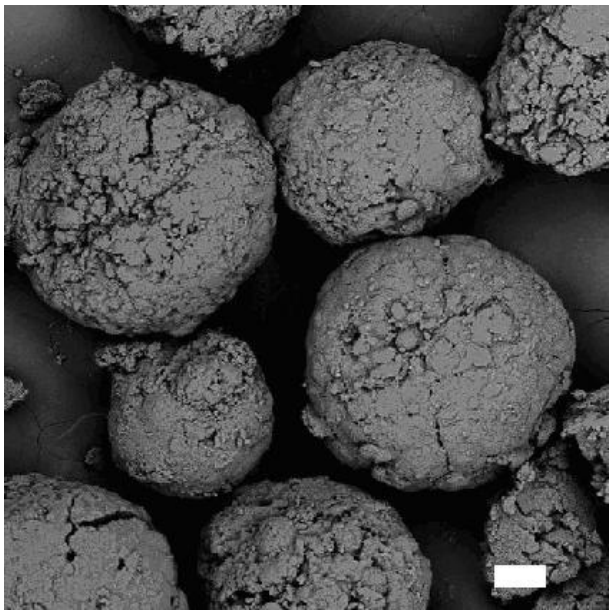

Figure 3.6. SEM micrographs (scale bar 100 μm): a) **N2TS** particle before polymerization; b) Polyethylene particles made with **N2TS** (Run 6, Table 3.4).

3.3.5. Ethylene Polymerization with Covalently-Attached Supported Nickel Diimine Catalysts with Borate Activator

In some cases, even if covalently-attached supported catalysts are used for slurry polymerization, there is the potential risk of reactor fouling when weakly attached catalyst molecules are abstracted from the support and activated by reaction with cocatalyst present in solution. In addition, in order to take advantage of existing heterogeneous polymerization plant infrastructure, supported catalysts pre-activated with internal activators are desirable to avoid costly modifications related to external activator feed and removal. To investigate these possible advantages, supported nickel diimine catalysts pre-activated with borate internal activators were synthesized. Table 3.6 summarizes the polymerization results using this catalyst system. Borates with poor solubility in hexane were successfully used as internal activators, resulting in good catalyst activity compared to Run 1 in Table 3.5 for **N2TS** without activator, even less than those of the **N2TS/**EASC system. **N2B1TS** shows the highest catalyst activity. **B1** appears to be a better activator than **B2**, and it is more efficient in mole ratio of **B2/N2** equal to 2 (Run 2 and 4 in Table 3.6).

Table 3.6. Ethylene polymerization results using supported nickel diimine catalysts with borate activators.

Run	Polymerization		Results			
	Catalyst	Temperature (^oC)	Activity [a)]	T_m (^oC)	M_w (g/mol $\times 10^{-3}$)	M_w/M_n
1	N2B1TS-a	60	6500	125.9	100	4.9
2	N2B1TS	60	10950	125.7	95	3.9
3	N2B1TS	30	1840	129.7	150	4.8
4	N2B2TS	60	7050	125.7	96	4.6
5	N3B1TS	60	9810	125.3	86	4.7
6	N3B1TS	30	3380	130.7	154	3.9

Polymerization conditions: catalyst 10 mg, ethylene pressure 150 psig, time 15 min., temperature 60°C, solvent 200 mL hexane, 0.2 mmol TMA added as a scavenger.

[a)] Activity in Kg PE/(mol Ni × hour)

Figure 3.7 shows the proposed structure for the supported nickel diimine catalyst using internal borate activators. The nickel diimine complex **N2** is supposed to be covalently attached onto the TMA-treated silica (Schrekker et al., 2006). Physisorbed borates are assumed to activate the **N2** complex, which was previously alkylated during treatment with TMA. Although the borate internal activator was physisorbed onto the silica support, it is unlikely to be abstracted easily due to the poor solubility of borates in the hexane diluents, creating a very favorable supported catalyst for ethylene polymerization in slurry reactors.

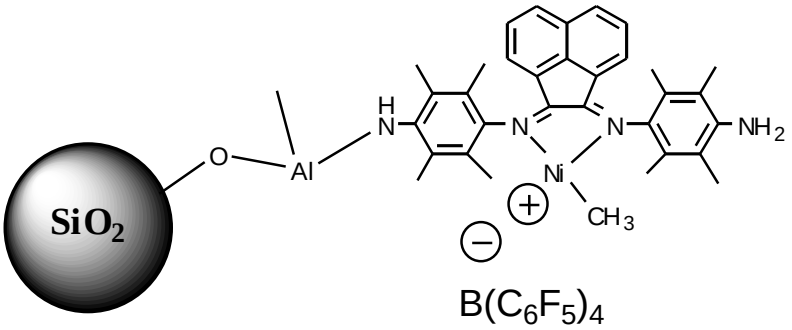

Figure 3.7. A proposed structure for **N2B1TS**.

SEM micrographs of polymer particles made with **N2B1TS** are shown in Figure 3.8. The shapes of the spherical polymer particles resemble that of the catalyst particles and have average diameters of about 250 μm.

a)

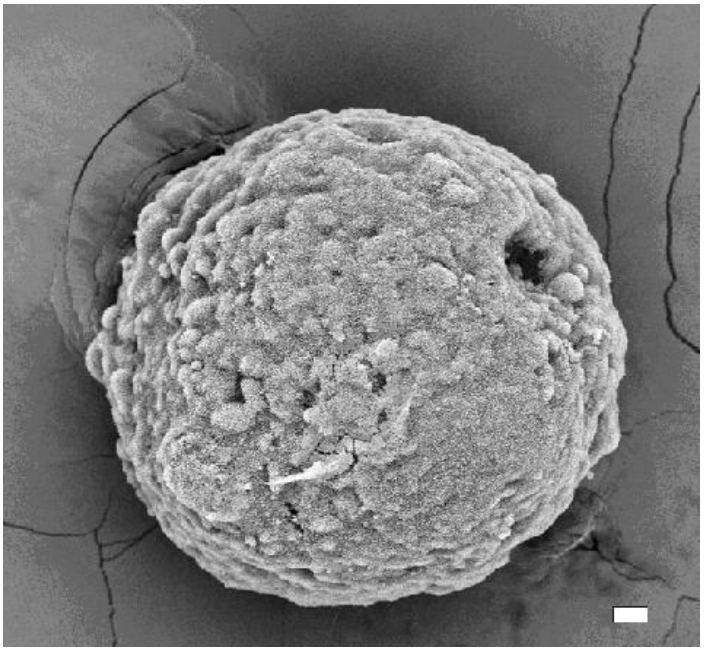

b)

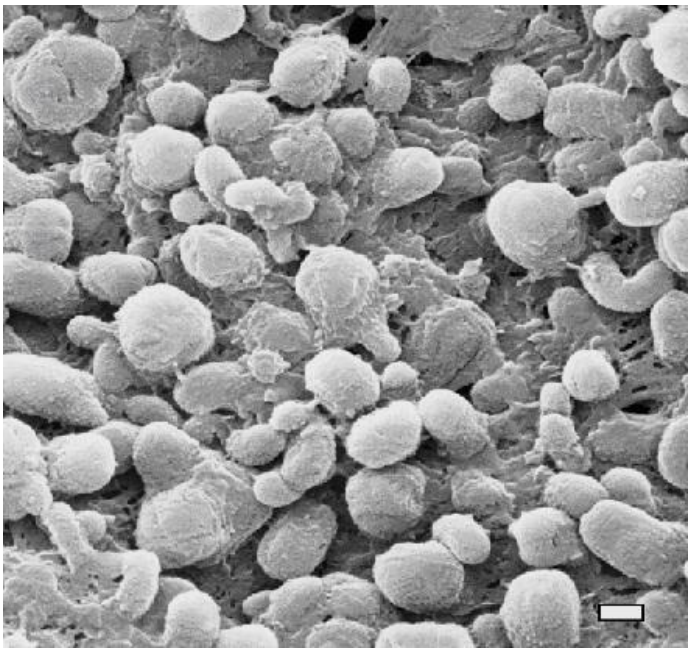

Figure 3.8. SEM micrographs (Run 2, Table 3.6): a) Polyethylene particles made with **N2B1TS (**scale bar 20 μm); b) A closer look at the external surface of a) (scale bar 0.4 μm).

3.4. Conclusion

Ethylene slurry polymerizations were performed using various supported nickel diimine catalysts. Compared with the equivalent homogeneous catalysts, the activities of physisorbed supported (**N1**) catalysts were significantly reduced and the morphologies of resultant polymer particles revealed that the nickel diimine complexes were weakly immobilized onto the silica support. On the other hand, the activities of covalently-attached supported catalysts (**N2** and **N3**) were much higher, producing polymer particles with good morphologies, supposedly due to the strong chemical bonding between the functionalized nickel diimine complexes and the alkylaluminum-treated support surface. Depending on the polymerization conditions, some supported catalysts had more stable active centers, resulting in enhanced catalyst activities and producing polymers with higher molecular weight averages. The use of borates as internal catalyst activators was also proposed as an excellent alternative to make supported catalysts with high activities and capable of producing polymer particles with well-controlled spherical morphology.

Chapter 4 : Ethylene Slurry Polymerization Using Nickel Diimine Catalysts Covalently-Attached onto $MgCl_2$-Based Supports

4.1. Introduction

Presently, the most common type of support for heterogeneous Ziegler-Natta catalysts is $MgCl_2$. These industrial catalysts are extremely active and produce polymer particles with high density and excellent morphology.

In this Chapter, $MgCl_2$/alcohol adducts were explored as an alternative catalyst support to SiO_2. They were crystallized by reaction with several alkylaluminums and used as supports for nickel diimine complexes functionalized with amine group (**N2** and **N3**). The **N2** catalyst was also supported on SiO_2 to serve as a reference for SiO_2-supported catalysts.

Ethylene polymerizations with $MgCl_2$-based supported catalysts were performed and the polymer properties were investigated by varying the polymerization conditions, the structure of the nickel diimine complexes, and the chemical components of the support.

4.2. Experimental

4.2.1. Materials

Anhydrous $MgCl_2$, methanol (99.8 %), isopropyl alcohol (99.5 %) and 2-ethyl hexanol (99.6 %) were purchased from Aldrich and used without further purification.

Other experimental materials are the same as described in Section 3.2.1.

4.2.2. Synthesis of $MgCl_2$-Based Supported Nickel Diimine Catalysts

An amount of 10 mmol of anhydrous $MgCl_2$, 30 mmol 2-ethyl hexanol, and 25 mL hexane were added to a dried 225 mL glass reactor equipped with a mechanical stirrer. After the mixture was maintained at 100°C overnight and cooled to room temperature, a clear $MgCl_2$/alcohol adduct solution was obtained. An amount of 50 mmol TMA was dropwised into the solution under 100 rpm. When 10 % of TMA was added, the $MgCl_2$/alcohol adduct began to crystallize. After complete addition of TMA for 1 hour, the mixture was allowed to react for 4 more hours. The stirring was stopped, the supernatant liquid was removed with a cannula, and the solid product was washed twice with 20 mL dichloromethane. An amount of 0.08 mmol **N2** was dissolved in 20 mL dichloromethane, added the precipitated solid, and allowed to react for 15 hours under 100 rpm. After the catalyst particles were precipitated, the black color of the **N2** solution disappeared, and a transparent solvent phase was separated. This indicated that **N2** was almost completely supported onto the $MgCl_2$-based support. The supported catalyst was filtered, washed with 20 mL dichloromethane, and then dried under vacuum. This supported catalyst was named $MgCl_2$-based supported **N2** catalyst (**N2Mg**). $MgCl_2$-based supported **N3** catalyst (**N3Mg**) was synthesized according to same procedure

using **N3**. Table 4.1 lists the chemical components of all supported catalysts made with this procedure.

One gram of silica (Grace Davison, XPO 2410) and 20 mL toluene were introduced in a same glass reactor. The reactor was heated to 60°C at a stirring rate of 100 rpm, then 20 mmol TMA was slowly added and reacted for 15 hours. After stopping the stirrer, the supernatant liquid was removed with a cannula, the product was washed two times with 20 mL toluene. An amount of 0.08 mmol **N2** was added to the product with 20 mL dichloromethane, and allowed to react for 15 hours under 100 rpm at room temperature. The produced supported catalyst (**N2Si**) was filtered and washed with 20 mL dichloromethane, and dried under vacuum. The analyzed Ni content was 0.65 wt.-%.

4.2.3. Characterization of Supported Nickel Diimine catalysts

Ni, Al and Mg contents on the supported catalysts were measured by inductively coupled plasma-optical emission spectroscopy (ICP). A LEO 1530 scanning electron microscope (SEM) combined energy dispersive X-ray (EDX) analysis was used to investigate the morphology of the catalysts and organic elements of the supported catalysts. For the SEM/EDX analysis, the supported catalysts particles were embedded onto an epoxy resin and cut into slices of 120 nm thicknesses with a diamond knife.

4.2.4. Polymerization

Polymerizations were carried out in a 300 mL semi-batch autoclave, equipped with a mass flow controller and a temperature control unit consisting of a cooling coil and an electric

heater. The polymerization temperature was maintained within ± 0.2^{o}C of the set point. Prior to each reaction, the reactor was purged several times with nitrogen, then heated to 120°C under vacuum and purged again to the set point temperature under nitrogen flow. A volume of 150 mL hexane and 1 mmol EASC or 0.1 mmol TIBA was transferred to the reactor. After introducing the supported catalyst in hexane slurry, polymerization took place under a continuous ethylene flow to meet the desired pressure. At the end of the polymerization time, the reactor was rapidly vented and the resultant polymer was precipitated and washed with acidified ethanol, then filtered and dried under vacuum.

4.2.5. Polymer Characterization

All polymerization characterization methods are the same as described in Section 3.2.6.

4.3. Results and Discussion

4.3.1. Structure of $MgCl_2$-Based Supported Nickel Diimine Catalysts

Scheme 4.1 describes the preparation steps for the synthesis of **N2Mg**. The reaction of TMA with $MgCl_2$/methanol adducts in hexane diluents leads to the precipitation of the $MgCl_2$-based support. The **N2** complex is likely supported through one or two of its amine functional groups, creating covalent bonds with the $MgCl_2$-based support.

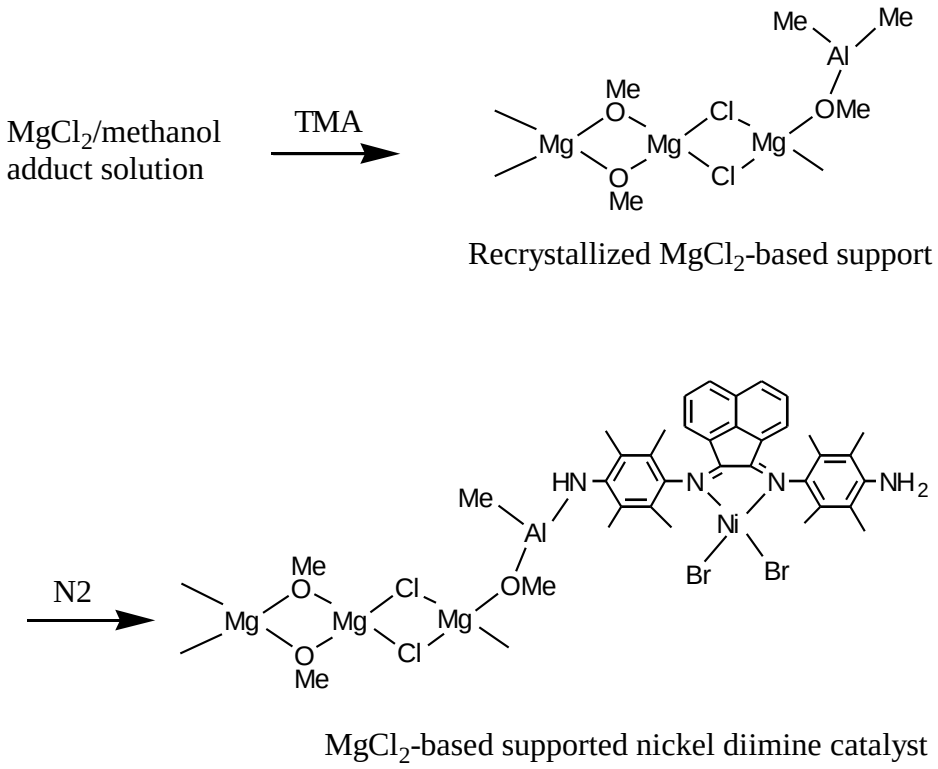

Scheme 4.1. Preparation of $MgCl_2$-based supported nickel diimine catalyst (**N2Mg**).

Figure 4.1 shows a SEM image of a spherical catalyst particle containing several wide cracks. These cracks may be formed when the epoxy-embedded particle was microtomed with the diamond knife, and indicates that its mechanical strength is not very high.

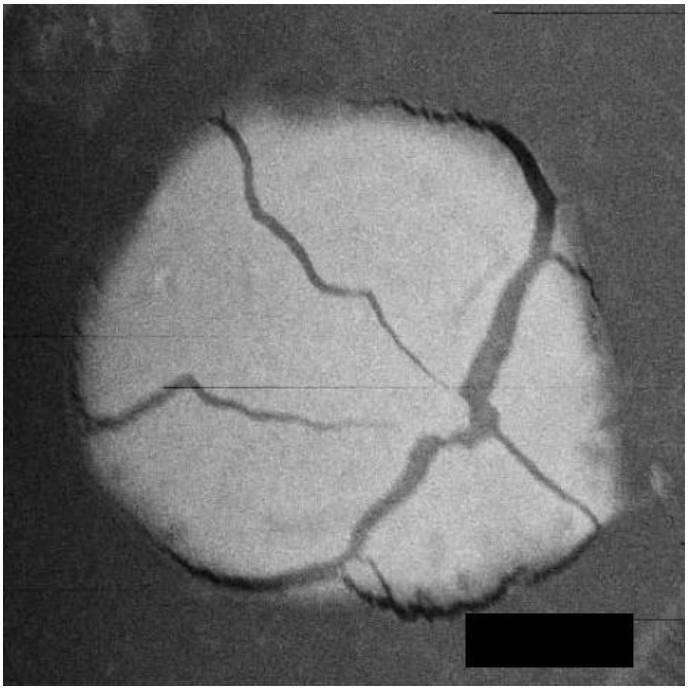

Figure 4.1. SEM micrograph of a **N2Mg** particle (Entry 1 in the Table 4.1, scale bar 5 μm).

Table 4.1 lists the chemical components and characterization results for $MgCl_2$-based supported catalysts investigated in this study. Compared with the content of other elements, the fraction of Al on the support is relatively low. It seems that the alkylaluminum acts mostly as a dealcoholation reagent, helping crystallize the $MgCl_2$/alcohol adducts, and that only a small fraction of the alkylaluminum molecules become physisorbed onto the $MgCl_2$-based support surface. It is also possible that excess alkylaluminum molecules are removed during the catalyst washing steps.

Table 4.1. Description of prepared $MgCl_2$-based supported nickel diimine catalysts.

Entry	Used Chemical Components				Characterization Results					Supporting Efficiency [a)]			
	Ni complex (mmol)	$MgCl_2$ (mmol)	Alcohol (mmol)	Alkyl aluminum (mmol)	Ni (mmol/g catalyst)	Mg (mmol/g catalyst)	Cl (mmol/g catalyst)	O (mmol/g catalyst)	Al (mmol/g catalyst)	Mg (wt.-%)	Cl (wt.-%)	O (wt.-%)	Al (wt.-%)
1	N2 0.08	10	2-ethyl hexanol 30	TMA 50	0.053	6.21	8.61	17.59	0.85	93.7	65.0	88.5	2.6
2	N2 0.08	10	2-ethyl hexanol 30	TIBA 50	0.049	5.09	6.91	16.23	1.11	83.1	56.4	88.3	3.6
3	N2 0.08	10	methanol 30	TMA 50	0.053	6.05	8.44	17.88	1.04	90.9	64.0	90.0	3.2
4	N2 0.08	10	methanol 30	TIBA 50	0.051	5.75	7.51	18.58	0.99	90.7	58.9	97.2	3.2
5	N2 0.08	10	isopropyl alcohol 30	TMA 50	0.049	5.76	9.60	19.81	0.73	94.2	78.4	92.6	2.4
6	N3 0.08	10	2-ethyl hexanol 30	TMA 50	0.055	6.14	7.74	16.89	0.82	91.4	56.2	81.9	2.4

[a)] Calculated assuming 100% Ni deposition.

4.3.2. Ethylene Polymerization

Ethylene polymerizations using homogenous and SiO_2-supported nickel diimine catalysts were conducted to serve as a reference for the polymerizations using $MgCl_2$-based supported nickel diimine catalysts. Table 4.2 summarizes these polymerization results.

Table 4.2. Comparison of ethylene polymerization results with homogeneous and supported nickel diimine catalysts.

Run	Polymerization Conditions		Results			
	Catalyst	Activator	Activity [a)]	T_m (°C)	M_w (g/mol ×10^{-3})	M_w/M_n
1	N2	EASC	41200	115.2	60	2.8
2	N3	EASC	6900	122.8	67	3.3
3	N2Si	EASC	29600	126.7	143	5.8
4	N2Si	Not used	1460	127.1	167	4.9
5	N2Mg	EASC	36450	125.5	127	5.5
6	N2Mg	Not used	12550	126.6	140	5.5
7	N3Mg	EASC	7250	123.5	154	5.8
8	N3Mg	Not used	4960	124.4	172	5.9

Polymerization conditions: homogeneous catalyst 0.5 μmol, supported catalyst 10-20 mg, EASC 1 mmol, TIBA 0.1 mmol in Runs 4, 6, 8; solvent 150 mL hexane, ethylene pressure 150 psig, temperature 60°C, time 15 min.; $MgCl_2$-based support: $MgCl_2$/2-ethyl hexanol/TMA.

[a)] Activity in kg PE/(mol Ni × h).

In general, a significant reduction in catalyst activity is observed when homogeneous catalysts are supported on several different carriers. This behavior has been attributed to catalyst poisoning by functional groups and impurities present on the catalyst surface, or

to steric hindrance caused by the support (Wilke, 1988). In the present investigation, however, the activities of the supported catalysts were comparable to those of the homogeneous catalysts. It seems that the **N2** and **N3** complexes are covalently bonded to the support through their amine groups, forming highly active and strongly immobilized metal centers as discussed in Chapter 3. The homogeneous **N2** catalyst was more active, and produced polymer with lower T_m, than the homogeneous **N3** catalyst; these trends were the same when **N2** and **N3** were supported on SiO_2 or $MgCl_2$-based supports.

Interestingly, the **N2Mg** had higher activity than **N2Si** (Runs 3 and 5, Table 4.2), and its activity was nearly 90% of the homogeneous catalysts (Runs 1 and 5, Table 4.2). The activity of **N3Mg** was even slightly higher than that of the homogeneous **N3** complex (Runs 2 and 7, Table 4.2). Both **N2Mg** and **N3Mg** also had considerable high activities in the absence of the EASC activator. The Lewis acidic $MgCl_2$-based supports may be able to activate nickel diimine complexes, as reported by T. J. Marks and coworkers (Finch et al., 1990). The T_m and M_w of the polymer made with the supported catalysts without activator were also a little higher than those made in the presence of the EASC, indicating that EASC favored β-hydride elimination and chain walking.

Comparative CRYSTAF results are shown in Figure 4.2. Polyethylenes made with **N2Mg** and **N2** had different microstructures. The polymer made with **N2** (Run 1, Table 4.2) had a broader SCBD in the temperature range 40-75°C, while polymer made with **N2Mg** (Run 5, Table 4.2) had a narrower SCBD (80-90°C) with a high crystallization temperature peak (>85°C). It seems that steric effects between support and **N2** depress chain walking rates and, therefore, produce polymer chains having lower SCB content

and higher T_m. This is also a clear indication that the catalyst is firmly anchored onto the support surface.

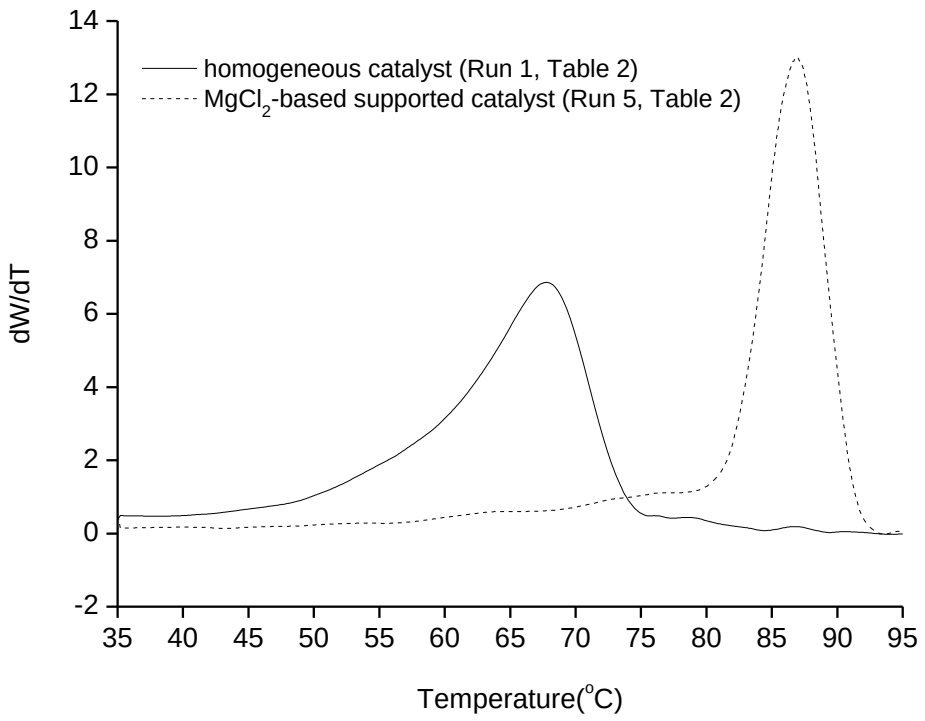

Figure 4.2. Cyrstaf (SCBD) profiles of polyethylene made with **N2** and **N2Mg**.

Ethylene polymerization results under different polymerization conditions in the absence of activator are shown in Table 4.3. As the polymerization temperature increases, a maximum activity is reached at 60°C, and then decreases for **N2Mg**. On the other hand, the catalyst activity is not very sensitive to temperature variations for **N3Mg**. Increasing ethylene pressure, or decreasing temperature, led to polymer with higher T_m and higher M_w, as expected, due to the chain walking mechanism.

Table 4.3. Ethylene polymerization results using $MgCl_2$-based supported nickel diimine catalysts in the absence of activator.

Run	Polymerization Conditions				Results		
	Catalyst	Pressure (psig)	Temperature (^oC)	Activity [a)]	T_m (^oC)	M_w (g/mol $\times 10^{-3}$)	M_w/M_n
1	N2Mg	150	30	4590	129.6	202	4.4
2	N2Mg	150	60	12550	126.6	140	5.5
3	N2Mg	150	80	7690	124.1	84	5.3
4	N2Mg	50	60	4400	123.8	110	5.3
5	N3Mg	150	30	3620	129.0	334	5.2
6	N3Mg	150	60	4960	124.4	172	5.9
7	N3Mg	50	30	1470	126.4	211	5.8

Polymerization conditions: catalyst 30-40 mg, TIBA 0.1 mmol, solvent 150 mL hexane, time 15 min.; $MgCl_2$-based support: $MgCl_2$/2-ethyl hexanol/TMA.

[a)] Activity in kg PE/(mol Ni × h).

To compare the effect of support structure on catalyst activity, various alcohols and alkylaluminums were used to synthesize $MgCl_2$-based supported nickel diimine catalysts; these polymerization results are shown in Table 4.4. $MgCl_2$-based supports, in combination with methanol/TMA, produced catalysts with the highest activity. It seems that a favorable electronic environment, based on the acidic nature of the support, was generated when methanol/TMA was used. The supported catalyst, in combination with 2-ethyl hexanol/TIBA, made polymer with the highest M_w. It is likely that TIBA, with bulky alkyl groups, has a lower chain transfer rate than TMA, and therefore produces polyethylene with higher M_w (Jamjah et al., 2008). Regardless of the support type, the catalysts activities at 60°C were higher than at 30°C, but T_m and M_w were lower.

Table 4.4. Effect of the support components using **N2** complex on ethylene polymerization.

Run	Polymerization Conditions			Results			
	$MgCl_2$-based Support		Temp. (°C)	Activity [a)]	T_m (°C)	M_w (g/mol ×10^{-3})	M_w/M_n [b)]
	Alcohol	Alkyl Aluminum					
1	2-ethyl hexanol	TMA	30	7590	129.6	204	5.4
2	2-ethyl hexanol	TIBA	30	7290	130.8	273	5.8
3	methanol	TMA	30	12890	131.1	199	5.6
4	methanol	TIBA	30	8970	129.7	213	5.1
5	isopropyl alcohol	TMA	30	8300	129.9	198	5.3
6	2-ethyl hexanol	TMA	60	12550	126.5	140	5.5
7	2-ethyl hexanol	TIBA	60	11080	128.0	154	6.3
8	methanol	TMA	60	18200	128.2	144	6.4
9	methanol	TIBA	60	14290	126.9	152	5.7
10	isopropyl alcohol	TMA	30	13150	127.0	145	5.6

Polymerization conditions: catalyst 30-40 mg, TIBA 0.1 mmol, solvent 150 mL hexane, time 15 min.

[a)] Activity in kg PE/(mol Ni × h).

[b)] Polydispersity index (M_w/M_n)

SEM micrographs of the polymer particles made with both the $MgCl_2$-based supported catalyst and the SiO_2-supported catalyst are compared in Figure 4.3. There was no reactor fouling during the polymerizations, and free-flowing polymer particles were always obtained. Figure 4.3.a shows the polymer particles made using **N2Mg** (Run 5, Table 4.2) had rough and apparently frail surfaces, resulting in particles with irregular shapes and debris. In Figure 4.3.c, the expanded view of Figure 4.3.a, the primary particles that compose the larger secondary particles appear as relatively flat stacks with high porosity, which lowers the bulk density of the secondary particles. On the other

hand, Figure 4.3.b depicts polymer particles made with **N2Si** (Run 3, Table 4.2), where denser and roughly spherical primary and secondary particles (Figure 4.3.d) are apparent.

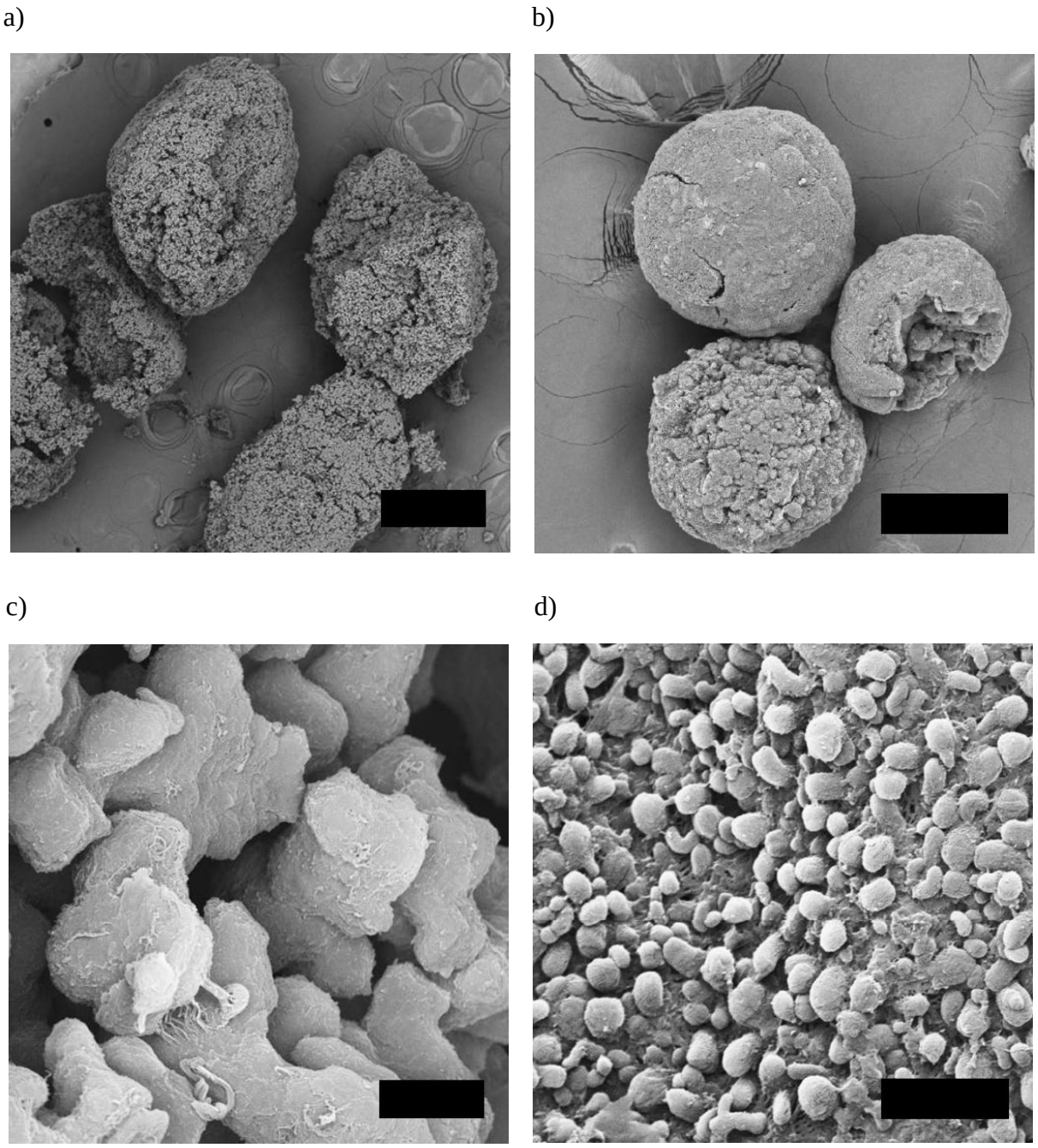

Figure 4.3. SEM micrographs of polymer particles: a) Polyethylene particles using **N2Mg (**Run 5 in Table 4.2, scale bar 200 μm); b) Polyethylene particles made with **N2Si (**Run 3 in Table 4.2, scale bar 200 μm); c) A closer look at the external surface of a) (scale bar 2 μm); d) A closer look at the external surface of b) (scale bar 2 μm).

4. 4. Conclusion

Ethylene slurry polymerizations were performed using various $MgCl_2$-based supported nickel diimine catalysts. Nickel diimine complexes having amine functional groups were covalently attached onto $MgCl_2$-based supports, producing highly active and strongly immobilized nickel diimine complexes. The Lewis acidic $MgCl_2$-based supports were able to act as activators for the nickel diimine complexes, leading to active polymerization catalysts even in the absence of external alkylaluminum activators. The chemical structure of the support had an influence on catalyst activity and microstructure of the resultant polymers. The polymers made with $MgCl_2$-based supports resulted in free-flowing particles that did not cause reactor fouling, but were weaker and more porous than the ones made with the equivalent SiO_2-supported catalyst.

Chapter 5 : Supported Hybrid Early and Late Transition Metal Catalysts for the Synthesis of Polyethylene with Tailored Molecular Weight and Chemical Composition Distributions

5. 1. Introduction

Because single-site catalysts such as metallocene produce polymers with narrow MWD and constant SCB averages across the MWD, combining a metallocene that makes high molecular weight polymer with higher comonomer content and another metallocene that produces low molecular weight polymer with low comonomer content is an evident way to produce a polymer with bimodal MWD and inverse comonomer composition distribution.

In this chapter, the supported hybrid early and late transition metal catalysts were synthesized and used to polymerize ethylene and to copolymerize ethylene and 1-hexene in a slurry reactor. The metallocene components were supported on SiO_2 to make high molecular weight polymer with controlled SCBs by addition of 1-hexene. The nickel diimine catalyst was supported on the same SiO_2-support to produce low molecular

weight polymer with controllable SCB frequency by the chain walking mechanism. These hybrid catalysts could make polymers with precisely tailored SCBs frequencies, especially inverse SCBDs, as well as broad MWD. The resultant polyethylene particles were spherical and free-flowing, ideally suited for slurry and gas-phase processes.

5.2. Experimental

5.2.1. Materials

The metallocenes, bis(6-t-butoxyhexylcyclopentadienylide)zirconium dichloride (named **Z**), and methyl(6-t-butoxyhexyl)silyl(η^5-tetramethylcyclopentadienyl)(t-butylamido)titanium dichloride (named **T**) were provided by LG Chem (US 7294600, 2007). Silica (Sylopol 948, Grace Davison, average particle size 55 µm, total volatiles 10.0 %, surface area 280-355 m^2/g, pore volume 1.55 cc/g) was used as the catalyst support after drying under vacuum overnight at 150°C.

Other experimental materials are the same as described in Section 3.2.1.

The structure of catalysts and the borate activator used in the experiments described in this chapter are shown in Figure 5.1.

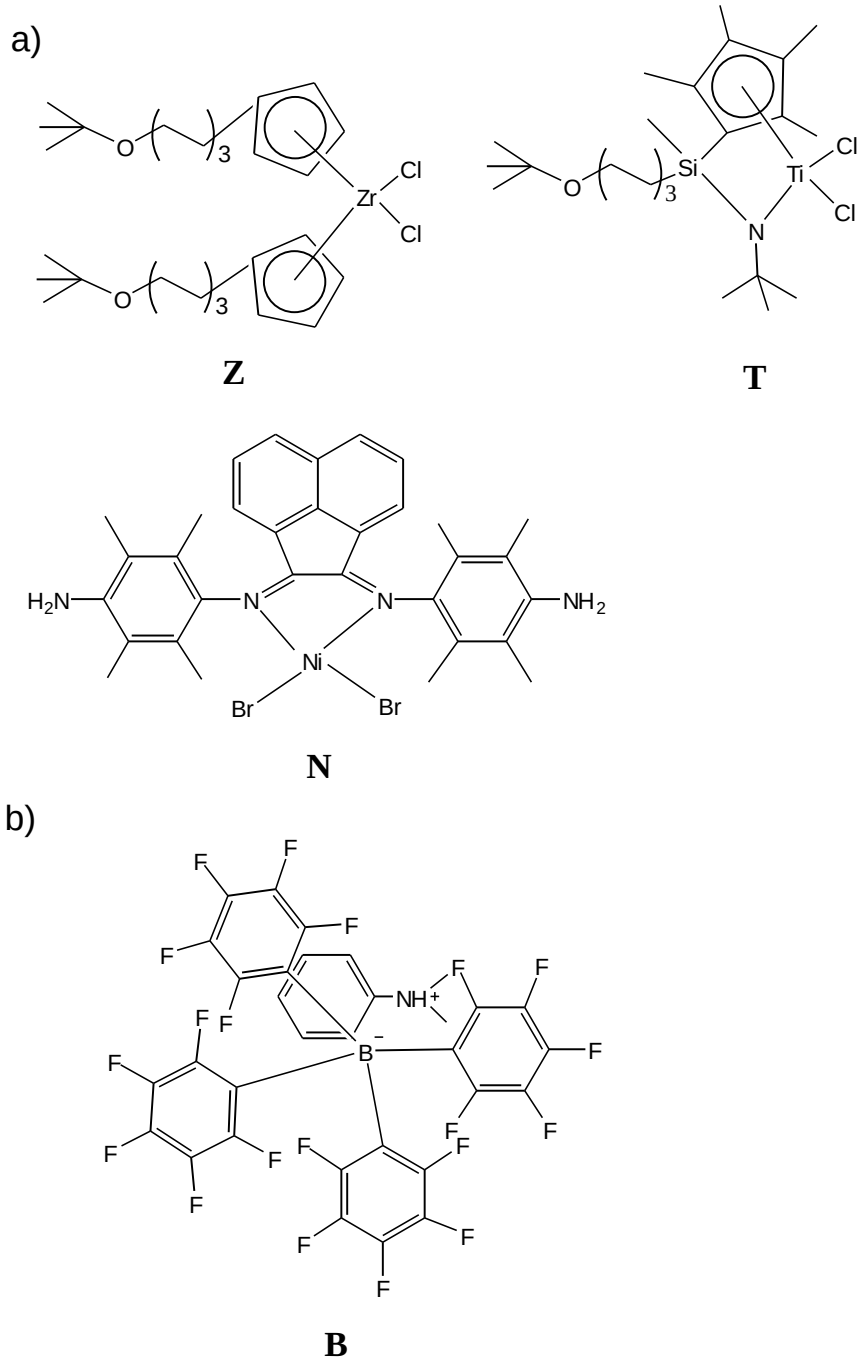

Figure 5.1. a) Catalysts: bis(6-t-butoxyhexylcyclopentadienylide)zirconium dichloride (**Z**), methyl(6-t-butoxyhexyl)silyl(η^5-tetramethylcyclopentadienyl)(t-butylamido)titanium dichloride (**T**), and bis(4-amino-2,3,5,6-tetramethylimino)acenaphtene nickel(II) dibromide (**N**); and b) Activator: dimethylanilium tetrakis(pentafluorophenyl)borate (**B**).

5.2.2. Synthesis of Supported Catalysts

5.2.2.1. Supported Single Catalysts ($_S$N, $_S$Z, $_S$T)

One gram of dried Sylopol 948 and 20 mL toluene were introduced in a dried 225 mL glass reactor equipped with a mechanical stirrer. An amount of 20 mmol TMA (2M toluene solution) was slowly added to the reactor at 60°C with a stirring rate of 200 rpm and reacted overnight. After stopping the stirrer, the supernatant liquid was removed with a cannula, the product was washed three times with 20 mL dichloromethane, and finally heated at 30°C under 200 rpm. An amount of 0.07 mmol **N** was added with 20 mL dichloromethane to the reactor, and reacted overnight. The product was filtered, washed with 20 mL toluene, and heated at 30°C under 200 rpm. An amount of 0.14 mmol **B** was added to the reactor with 20 mL dichloromethane and reacted for 3 hours, then dried under vacuum without washing. This final supported catalyst was named $_S$**N**.

Other supported catalysts using single catalysts, $_S$**Z** and $_S$**T**, were synthesized according to a similar procedure, but toluene was used instead of dichloromethane as solvent.

5.2.2.2. Supported Hybrid Catalysts ($_S$ZN, $_S$TN)

The procedure for making the hybrid catalysts was similar to that used for the single catalysts. After supporting 0.035 mmol of **Z** onto SiO_2, filtering, and washing, 0.035 mmol of **N** was supported following the same procedure, and then 0.14 mmol **B** was added to the support and dried without further treatment. The final supported catalyst was named $_S$**ZN**.

The hybrid catalyst $_S$**TN** was synthesized according to the same procedure, but 0.175 mmol of **T** and 0.42 mmol of **B** were used.

5.2.3. Characterization of the Supported Catalysts

Zr, Ti, Ni, and Al contents on the supported catalysts were measured by inductively coupled plasma-optical emission spectroscopy (ICP).

5.2.4. Polymerization

All polymerization procedures were the same as described in Section 4.2.5.

5.2.5. Polymer Characterization

The CCD was measured with crystallization elution fractionation (CEF, Polymer Char). Samples were dissolved at 160°C for 60 min, followed by 5 min of equilibration at 95°C. The cooling rate during crystallization was 3°C/min, from 95°C to 35°C, and then the heating rate during elution was 3°C/min, from 35°C to 140°C with 1 mL/min elution flow. The SCB frequency was analyzed by ^{13}C NMR spectroscopy (Bruker 500 MHz). The polymer was first made into a film using a hot press and was cut about 4.2 cm × 0.3 cm. A sample mass of 0.1 g and 0.7 g of tetrachloroethane-d_2 solvent were transferred into the 5 mm NMR tube, and the sample was allowed to dissolve at 130°C. The NMR spectra were acquired at 120°C with 2000 scanning number. Other polymerization characterization methods are the same as described in Section 3.2.6.

5.3. Results and Discussion

5.3.1. Supported Catalyst Structure

Scheme 5.1 shows the proposed structures for the supported hybrid catalysts, including the borate activator. The metallocenes (**Z** and **T**) with functional *t*-butoxy groups, and the nickel diimine catalyst (**N**) with functional amine groups, are likely to be covalently attached onto the TMA-treated SiO_2-support. These chemical bonds tether the catalysts onto the SiO_2 surface, resulting in minimal active site leaching during polymerization. The borate, which is used to activate the catalyst, is physisorbed onto the SiO_2-support. These pre-activated supported catalysts avoid costly process modification for external activator supply and elimination. In addition, they enhance the polymer particle morphology by reducing reactor fouling that happens when abstracted catalyst molecules become active for polymerization by reaction with activator present in solution.

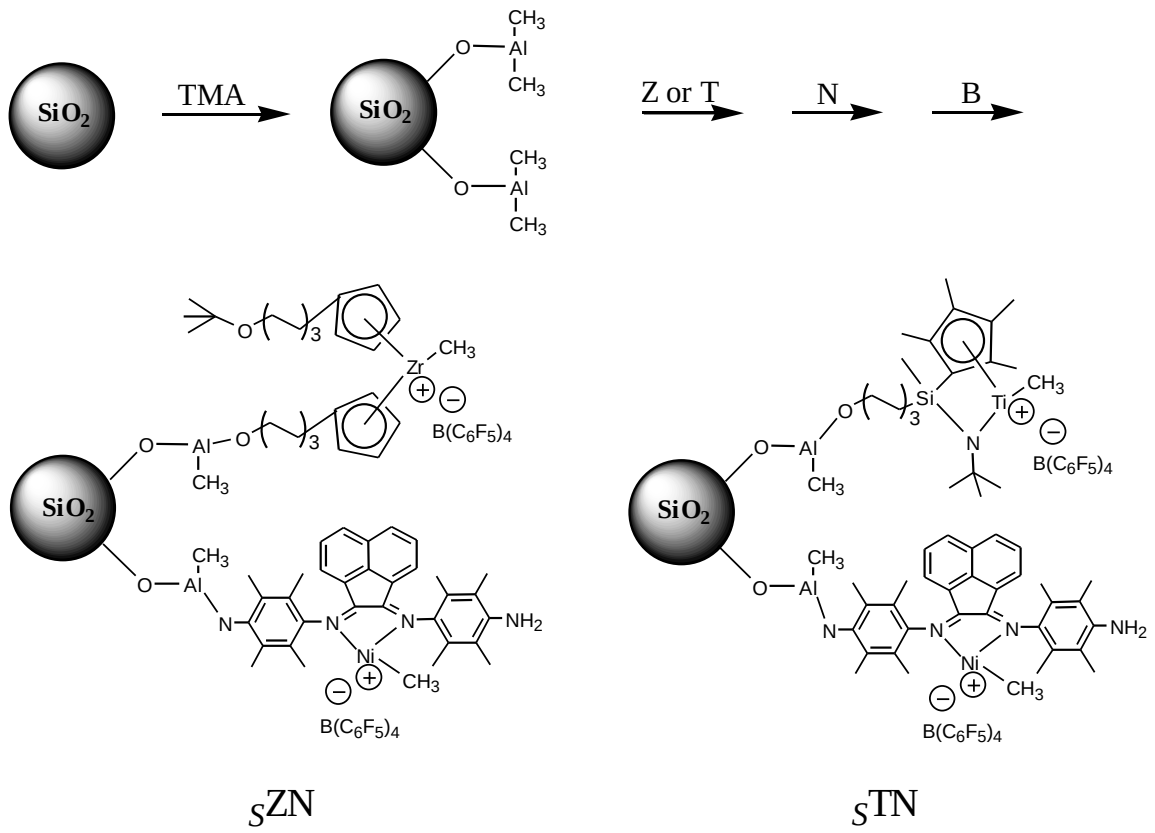

Scheme 5.1. Synthesis steps for supported hybrid catalysts (***s*ZN** and ***s*TN**).

Table 5.1 summarizes the components and the ICP results of all supported catalysts. Most of the catalyst metal components were deposited onto the SiO_2-support, but supporting efficiencies for Al were much lower. It is reasonable to assume that the alkylaluminum molecules first react with the hydroxyl groups available on the SiO_2-support and the remaining excess molecules are then physically adsorbed onto the surface.

Table 5.1. Description of the supported catalysts.

Name	Components			ICP results		Supporting efficiency [a)]	
	Catalyst (mmol)	TMA (mmol)	Borate (mmol)	Zr, Ti, Ni (mmol/g catalyst)	Al (mmol/g catalyst)	Zr, Ti, Ni (wt.-%)	Al (wt.-%)
$_S$Z	Z 0.07	20	0.14	Zr 0.054	1.421	Zr 96.4	14.8
$_S$T	T 0.07	20	0.14	Ti 0.053	1.425	Ti 92.9	15.0
$_S$N	N 0.07	20	0.14	Ni 0.055	1.429	Ni 98.2	15.1
$_S$ZN	Z 0.035 N 0.035	20	0.14	Zr 0.026 Ni 0.027	1.318	Zr 96.3 Ni 96.3	14.6
$_S$TN	T 0.175 N 0.035	20	0.42	Ti 0.101 Ni 0.022	1.420	Ti 91.1 Ni 95.7	14.7

SiO_2-Support: Sylopol 1g.

[a)] Calculated on ICP results of Al deposition, and assumption of 100 % borate deposition.

5.3.2. Polymerization

5.3.2.1. Supported Single Catalysts ($_S$Z, $_S$T, $_S$N)

Ethylene homopolymerization and copolymerization with 1-hexene using $_S$**Z** and $_S$**T** were conducted under various polymerization conditions (Table 5.2). The catalyst activity is higher at higher temperatures, but decreases with increased 1-hexene concentration in the reactor. Increasing temperature or increasing 1-hexene concentration leads to polymer with lower M_w. Catalyst $_S$**T** made polymer with higher M_w than $_S$**Z**, but its activity is much lower than that of $_S$**Z**. As expected, the T_m of the polymer was in inverse proportion to 1-hexene reactor concentration, and this effect is more pronounced at higher temperatures. Catalyst $_S$**T** made polymer with lower T_m than $_S$**Z** under the same

conditions, indicating that **T** is more reactive towards α-olefin incorporation due to its constrained geometric ligand structure (Mehdiabadi and Soares, 2008).

Table 5.2. Results for ethylene homopolymerization and ethylene/1-hexene copolymerization using supported single catalysts $_S$**Z** and $_S$**T**.

Run	Polymerization Conditions			Results				
	Catalyst	Temp. (°C)	1-Hexene (C6/C2) [a)]	Yield (g)	Activity [b)]	T_m (°C)	M_w (g/mol ×10^{-3})	M_w/M_n
1	$_S$Z	40	0	0.8	3250	133.3	382	3.6
2	$_S$Z	40	0.2	0.8	2110	128.0	247	3.8
3	$_S$Z	40	0.4	0.8	2030	124.7	215	3.1
4	$_S$Z	60	0	2.8	11280	134.4	178	3.3
5	$_S$Z	60	0.2	2.1	7660	127.0	133	3.0
6	$_S$Z	60	0.4	1.3	4750	122.8	118	3.9
7	$_S$Z	70	0	4.4	17630	133.0	150	3.9
8	$_S$Z	70	0.2	3.0	11460	124.3	79	3.3
9	$_S$Z	70	0.4	3.0	9290	122.4	81	4.3
10	$_S$T	40	0	0.4	1560	133.4	1512	3.5
11	$_S$T	60	0	1.0	3760	133.5	1636	2.7
12	$_S$T	60	0.2	0.7	2670	120.6	978	3.7
13	$_S$T	60	0.4	0.9	2250	118.7	686	4.1
14	$_S$T	70	0	1.2	3940	131.4	1487	3.2
15	$_S$T	70	0.2	0.5	2920	116.8	865	3.9
16	$_S$T	70	0.4	0.5	2440	116.1	600	4.2

Polymerization conditions: supported catalyst 20-30 mg, TMA 0.1 mmol, solvent 150 mL hexane, ethylene pressure 150 psig, time 15 min.

[a)] Mole ratio of 1-hexene/ethylene.

[b)] Activity in kg PE/(mol Zr or Ti × h).

Figure 5.2 shows the GPC-IR plot for an ethylene and 1-hexene copolymerization using $_S$**Z** (Run 9, Table 5.2). The SCB frequency across the MWD is practically the same; this is a well-known characteristic of copolymers made with metallocenes and other single-site catalysts, as opposed to heterogeneous Ziegler-Natta polymers (Bubeck, 2002).

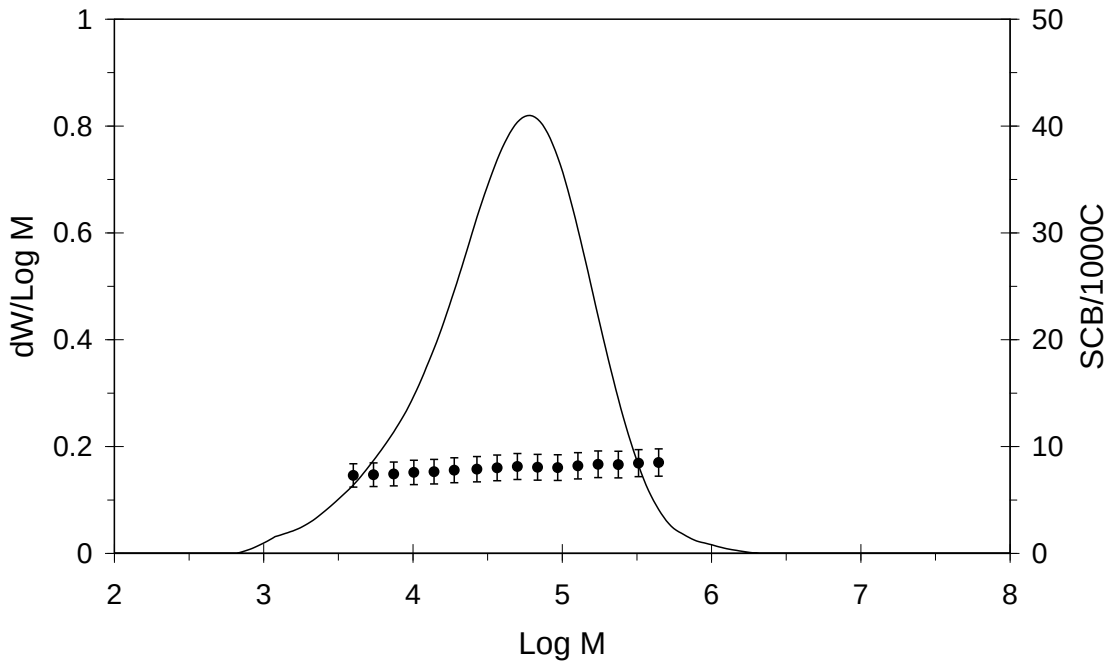

Figure 5.2. MWD and SCB frequency profiles of poly(ethylene-*co*-1-hexene) made with $_S$**Z** (Run 9, Table 5.2).

Comparative CEF results for copolymers made with $_S$**Z** at 70°C with different 1-hexene concentrations are shown in Figure 5.3. CEF is a new technique that achieves excellent fractionation results based on the crystallizabilities of copolymer chains in solution, combines aspects of crystallization analysis fractionation (CRYSTAF) and temperature rising elution crystallization (TREF) (Monrabal et al., 2007). In the CEF profiles shown in Figure 5.3, as the 1-hexene concentration in the reactor increases, the

CCD peak shifts to lower temperatures (A: 99.0°C; B: 94.2°C; C: 93.2°C), indicating higher 1-hexene incorporation in the copolymer. The high crystallization temperature peak shown for the homopolymer sample A is related to crystallization kinetics in CEF and should not be interpreted as differences in 1-hexene content, which is nil for this particular sample.

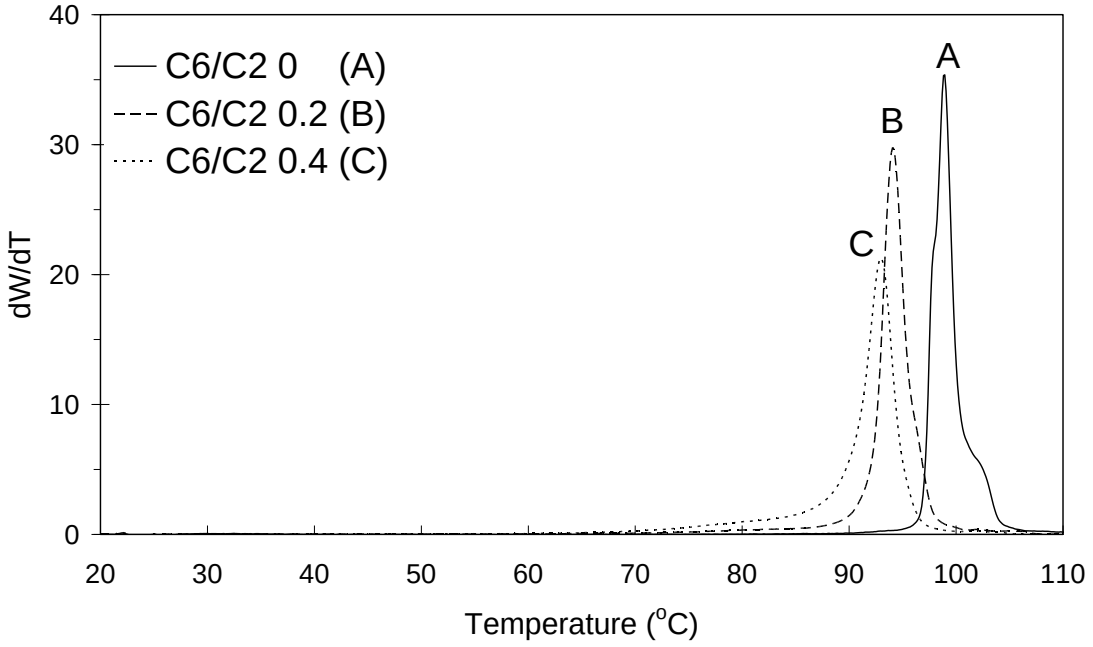

Figure 5.3. CEF (CCD) profiles of poly(ethylene-*co*-1-hexene) made with $_S$**Z:** A (Run 7, Table 5.2), B (Run 8, Table 5.2) and C (Run 9, Table 5.2).

For the ethylene slurry polymerization, all polymer particles were obtained in the form of free-flowing powders, except one sample made with $_S$**T** with high 1-hexene content (Run 16, Table 5.2). Representative pictures of polymer particles are shown Figure 5.4. The samples were transferred to round bottom glass tubes with 10 mm diameter that became filled with free-flowing polymer particles. This indicated that

metallocenes **Z** and **T**, having *t*-butoxy functional groups, were strongly supported on SiO_2, likely through covalent chemical bonding without any apparent abstraction of active sites during polymerization, resulting in excellent polymer particle morphologies. Moreover, these long alkyl groups bonding support and active site might provide enough space to reduce steric hindrance between the bulky SiO_2 surface and the active sites, thus favoring high catalyst activity. The copolymer with the high α-olefin incorporation was the only exception to the rule (Figure 5.4c), not because of site extraction, but due to the low crystallinity, "sticky" copolymer made during this copolymerization which led to particle agglomeration.

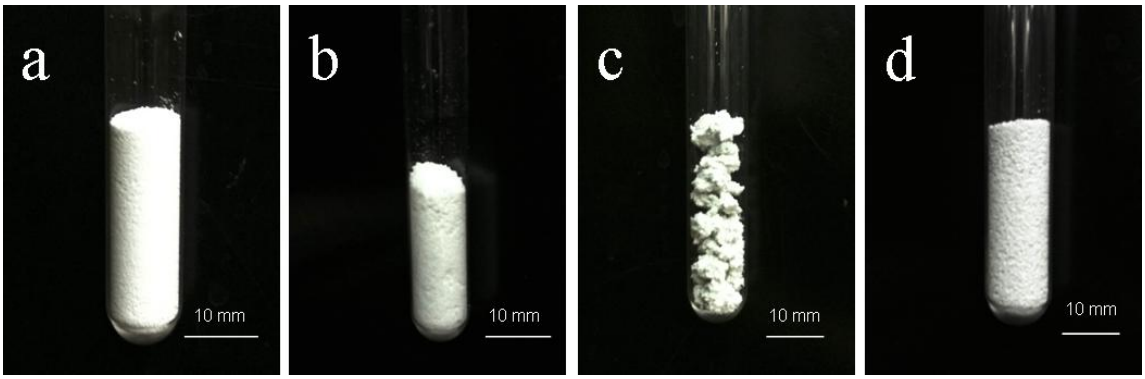

Figure 5.4. Representative pictures of polymer particles made with a: $_S$**Z** (Run 9, Table 5.2), b: $_S$**T** (Run 14, Table 5.2), c: $_S$**T** (Run 16, Table 5.2), and d: $_S$**N** (Run 9, Table 5.3).

Table 5.3 shows the polymerization results using $_S$**N**. In contrast to $_S$**Z** and $_S$**T**, the activities of $_S$**N** are the highest at 60°C. The catalyst activity for $_S$**N** is higher than for $_S$**Z** and $_S$**T** at the same 1-hexene concentration at 40°C and 60°C. Catalyst $_S$**N** made polymer with lower M_w, and slightly broader MWD than $_S$**Z** and $_S$**T**. It seems that the 1-hexene concentration does not affect much the catalyst activity and the T_m of the polymer. Higher

polymerization temperatures, however, lead to polymers with lower T_m by increasing the frequency of SCB formed by the chain walking mechanism. The low α-olefin reactivity of the nickel diimine catalyst is partially caused by active sites that are sterically hindered by bulky ligands, which limits α-olefin insertion onto the growing polymer chain. At the same time, these ligands make it possible to produce polymer with high M_w by depressing chain transfer reaction (Johnson et al., 1995).

Table 5.3. Results for ethylene homopolymerization and ethylene/1-hexene copolymerization with $_S$**N**.

Run	Polymerization Conditions			Results				
	Catalyst	Temp. (°C)	1-Hexene (C6/C2) [a)]	Yield (g)	Activity [b)]	T_m (°C)	M_w (g/mol ×10^{-3})	M_w/M_n
1	$_S$N	40	0	1.7	6810	128.5	98	3.7
2	$_S$N	40	0.2	1.7	6230	127.5	85	4.2
3	$_S$N	40	0.4	1.9	6940	126.6	87	4.3
4	$_S$N	60	0	4.0	16200	125.4	96	4.2
5	$_S$N	60	0.2	3.4	13670	124.3	73	4.7
6	$_S$N	60	0.4	3.6	11550	123.6	66	4.1
7	$_S$N	70	0	2.4	9610	123.0	86	4.1
8	$_S$N	70	0.2	2.1	6500	121.9	61	4.2
9	$_S$N	70	0.4	1.2	4140	121.3	67	4.5

Polymerization conditions: supported catalyst 20-30 mg, TMA 0.1 mmol, solvent 150 mL hexane, ethylene pressure 150 psig, time 15 min.

[a)] Mole ratio of 1-hexene/ethylene.

[b)] Activity in kg PE/(mol Ni × h).

Figure 5.5 shows the GPC-IR plot for the ethylene homopolymer made with $_S$**N**. The SCB frequency across the MWD decreases slightly at the highest molecular weights. Theoretically the SCB profile should be flat as well. This deviation from the theoretically predicted profile is probably due to some non-ideal behavior of the supported catalyst, but it may also be related to GPC fractionation: more highly branched chains are more compact in solution, and therefore elute at higher elution volumes and are "perceived" by the calibration curve as having lower molecular weights.

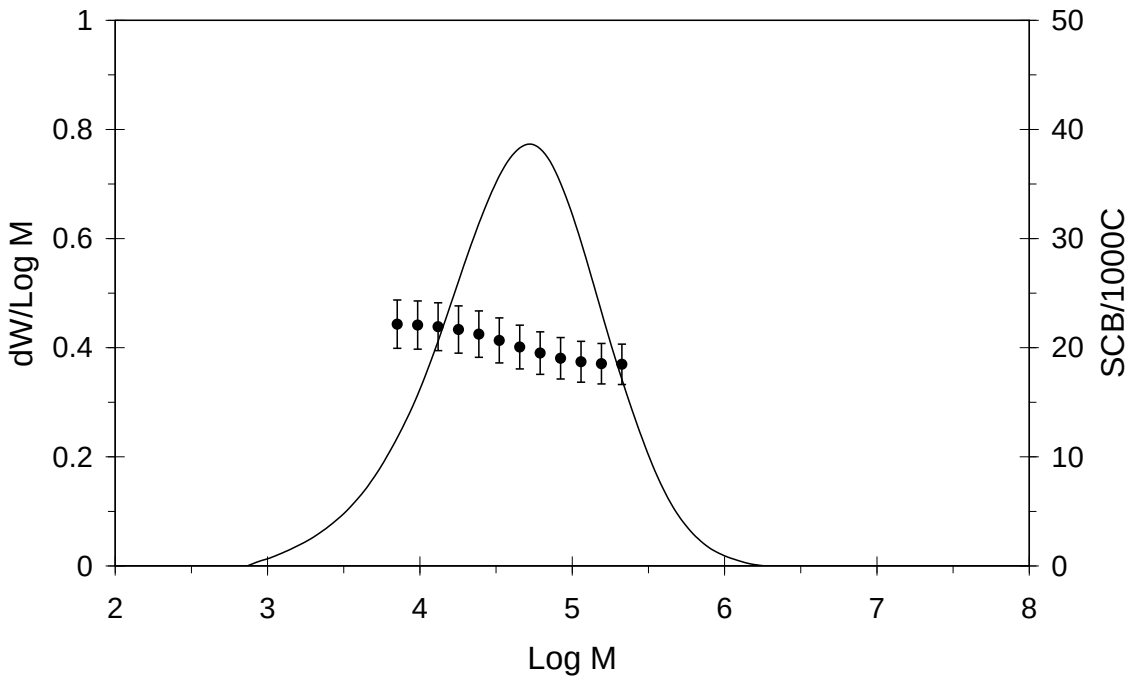

Figure 5.5. MWD and SCB frequency profiles of polyethylene made with $_S$**N** (Run 7, Table 5.3).

The CEF profiles in Figure 5.6.a show that narrow peaks are obtained for polymers made at 40°C; they are similar to those made with $_S$**Z**, as shown in Figure 5.3. Addition of 1-hexene shifts the CEF peak temperature from 95.4^{o}C to 94.1^{o}C (compare with Figure 5.3, where a much more pronounced change is observed when $_S$**Z** is used). Interestingly,

the CEF profiles for polymers made at 70°C (Figure 5.6.b) have two well defined peaks (93.2^{o}C and 79.0^{o}C), regardless of the 1-hexene concentration that varies slightly in relative amount as the concentration of 1-hexene in the reactor changes. These results are unusual, since $_{S}$**N** was expected to make polymers with unimodal SCBD due to its single-site nature; however, the CEF profiles look like those of LLDPE made with multiple-site systems such as heterogeneous Ziegler-Natta catalysts. As shown in Figure 5.4.d, this bimodality is not caused by the partial extraction of active sites out of the SiO_2-support, since free-flowing, high bulk density particles are produced during polymerization. Instead, it is likely that the supported nickel diimine catalyst $_{S}$**N** has at least two types of active sites that depend on specific site environments such as different configurations or locations on the SiO_2-support. One active site type seems to be more prone to chain walking, making polymers with lower CEF elution temperatures (79°C) at the higher polymerization temperature of 70°C. This difference is not as apparent for polymers made at 40°C (Figure 5.6.a) because the chain walking frequency decreases significantly when the polymerization temperature is reduced.

a)

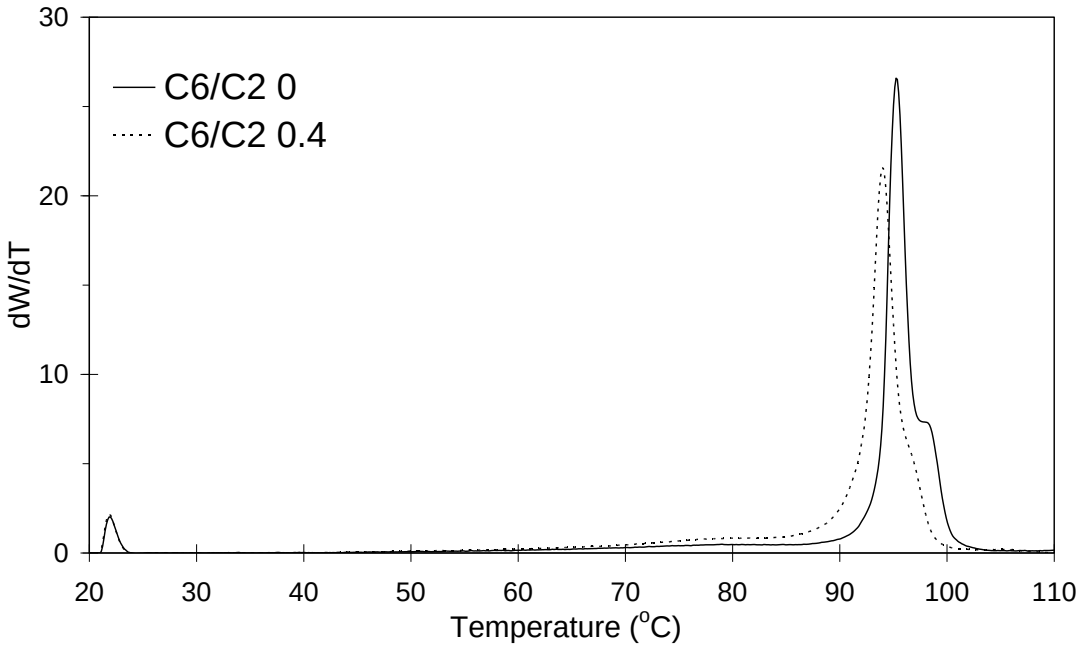

b)

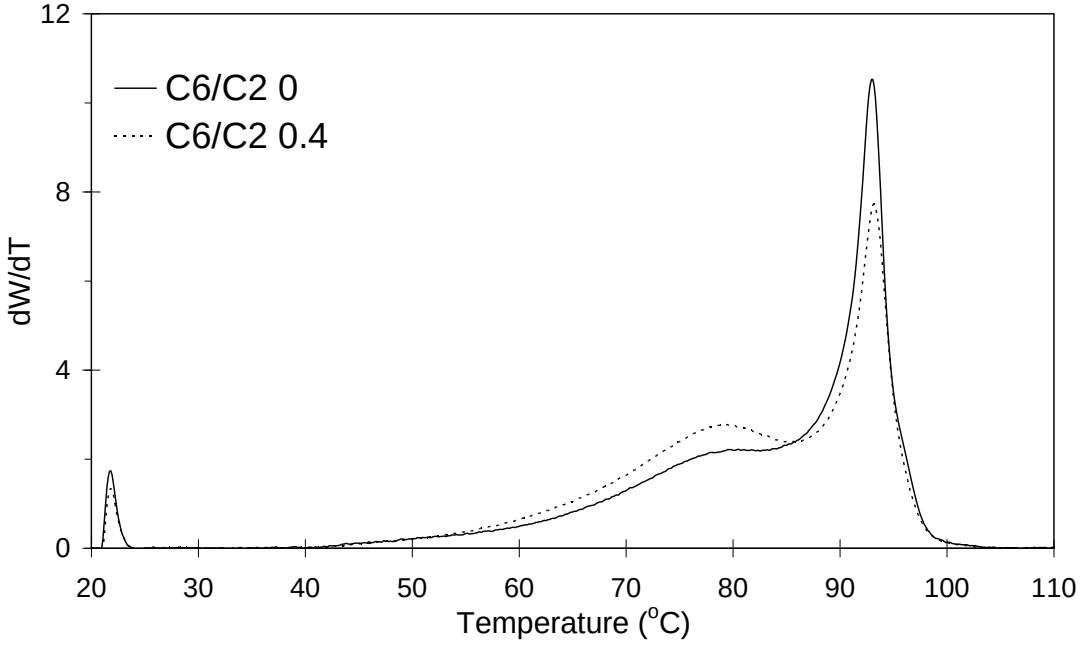

Figure 5.6. CEF profiles for poly(ethylene-*co*-1-hexene) made with $_{S}$**N**: a) (Run 1 and 3, Table 5.3) and b) (Run 7 and 9, Table 5.3).

5.3.2.2. Supported Hybrid Catalysts ($_S$ZN, $_S$TN)

Ethylene homopolymerization and ethylene/1-hexene copolymerization using $_S$**ZN** were conducted under the same polymerization conditions with supported single catalysts, and the results are summarized in Table 5.4. The catalyst activity, polymer T_m, and M_w fall between the values obtained for the single catalysts $_S$**Z** and $_S$**N**. As expected, all polymers have broader MWD than polymers made with supported single catalysts. Therefore, it seems that each active site type, **Z** and **N**, behaves independently of each other on the hybrid $_S$**ZN**.

The SCB frequency across the MWD is shown in Figure 5.7. Two polymer populations are present in the overall resin: the lower molecular weight population is made with the **N** catalyst and the high molecular weight polymer is made with the **Z** catalyst. The SCB frequency of the lower molecular weight polymer increases when the temperature changes from 40°C to 70°C (compare Figure 5.7.a and 5.7.b) because the chain walking frequency for the **N** catalyst increases at higher temperatures. No SCBs are detected in the higher molecular weight population in absence of 1-hexene (Figure 5.7.b), since SCBs are formed by 1-hexene incorporating by the **Z** catalyst. Accordingly, as the 1-hexene concentration in the reactor increases, the SCB frequency of the higher molecular weight population increases, becoming higher than that of the lower molecular weight polymer, as shown in Figure 5.7.c.

Table 5.4. Results for ethylene homopolymerization and ethylene/1-hexene copolymerization with $_S$**ZN**.

Run	Polymerization Conditions			Results				
	Catalyst	Temp. (°C)	1-Hexene (C6/C2) [a)]	Yield (g)	Activity [b)]	T_m (°C)	M_w (g/mol ×10^{-3})	M_w/M_n
1	$_S$ZN	40	0	1.0	4300	130.1	206	6.2
2	$_S$ZN	40	0.2	1.1	4110	128.1	141	5.5
3	$_S$ZN	40	0.4	1.0	4150	126.1	136	6.2
4	$_S$ZN	60	0	3.3	13260	128.7	124	7.1
5	$_S$ZN	60	0.2	2.6	10430	124.7	83	6.0
6	$_S$ZN	60	0.4	1.9	6120	122.5	96	7.8
7	$_S$ZN	70	0	3.7	14160	130.6	131	7.1
8	$_S$ZN	70	0.1	2.4	8710	125.5	106	5.1
9	$_S$ZN	70	0.2	1.7	6870	123.9	100	4.6
10	$_S$ZN	70	0.4	1.1	6440	120.2	77	6.4

Polymerization conditions: supported catalyst 20-30 mg, TMA 0.1 mmol, solvent 150 mL hexane, ethylene pressure 150 psig, time 15 min.

[a)] Mole ratio of 1-hexene/ethylene.

[b)] Activity in kg PE/(mol Zr and Ni × h).

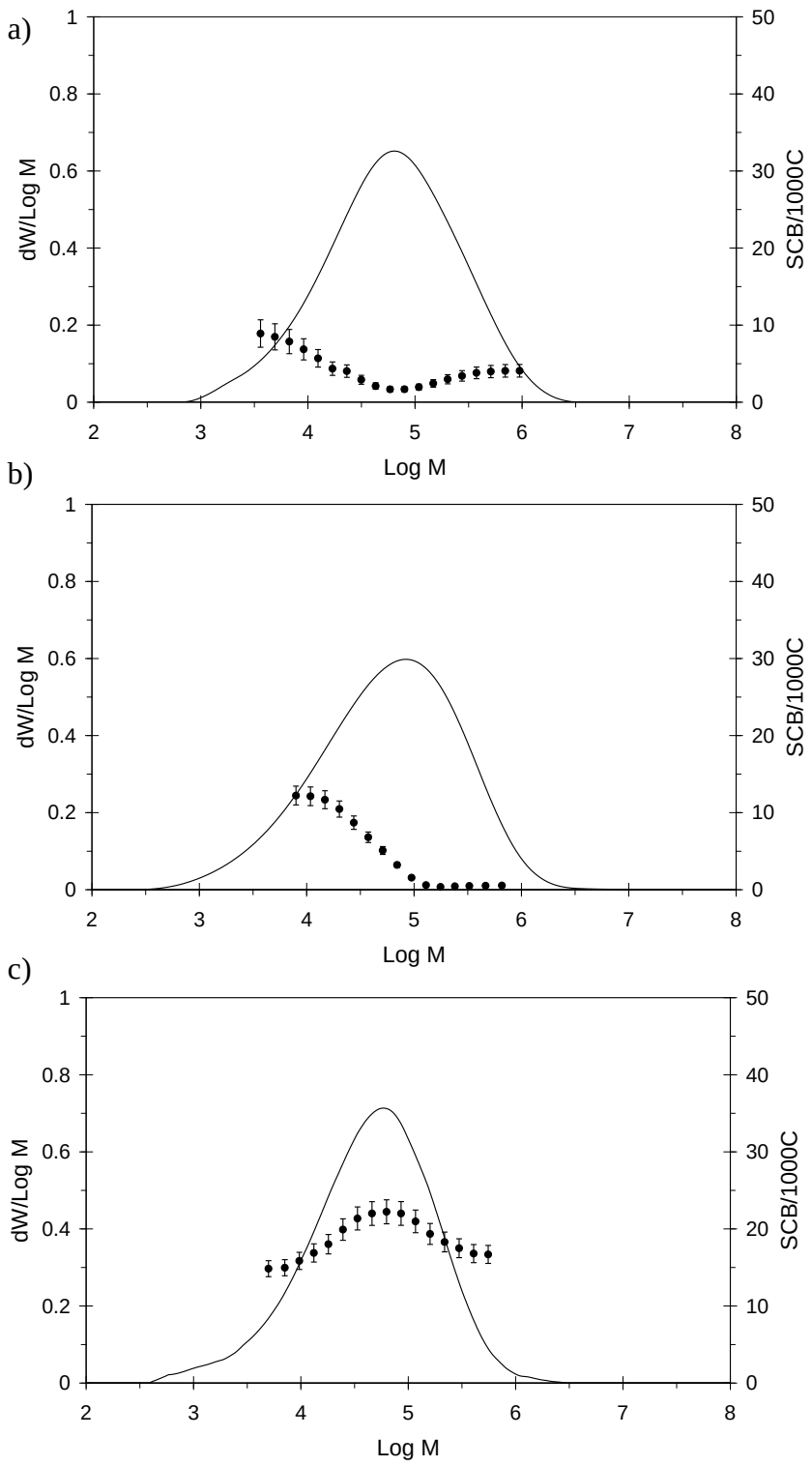

Figure 5.7. MWD and SCB frequency of polyethylene made with $_s$**ZN**. Polymerization conditions: a) 40°C, C6/C2 0.4 (Run 3, Table 5.4); b) 70°C, C6/C2 0 (Run 7, Table 5.4); c) 70°C, C6/C2 0.4 (Run 10, Table 5.4).

Short chain branches of various lengths (but predominantly methyl SCBs) are made by chain walking in the lower molecular weight population, and their frequency can be controlled by changing the polymerization temperature. At the same time, the amount of butyl branches of the higher molecular weight population is easily controlled by 1-hexene addition to the reactor. Therefore, this novel polyolefin has a rather unique microstructure that can be controlled by 1-hexene concentration, polymerization temperature, and **N/Z** ratio to optimize the polymer microstructure for a particular application. Moreover, $_S$**ZN** makes polymer with broad MWD, good processability (as attested by $M_w/M_n > 4.5$), and free-flowing particles (Figure 5.8.a) without reactor fouling.

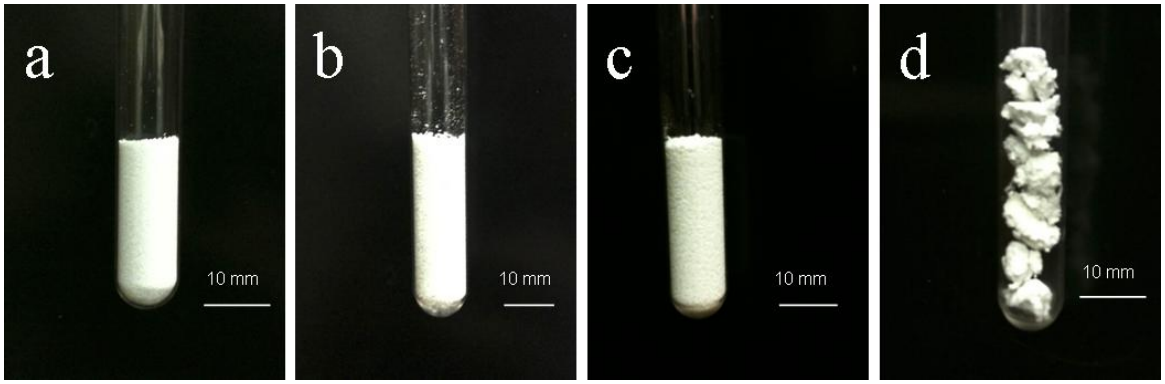

Figure 5.8. Representative pictures of polymer particles made with a: $_S$**ZN** (Run 10, Table 5.4), b: $_S$**TN** (Run 3, Table 5.6), c: $_S$**TN** (Run 7, Table 5.6), and d: $_S$**TN** (Run 9, Table 5.6).

To verify whether the **Z** and **N** catalysts behaved independently of each other in the $_S$**ZN** catalyst, we calculated the catalyst activity and M_w for $_S$**ZN** based on the values of $_S$**Z** and $_S$**N** at similar conditions. First, the molar fractions of polymers made with **Z** and

N, m_Z and m_N, respectively, in the combined $_S$**ZN** catalyst were estimated using Equations (5.1) and (5.2),

$$m_Z = \frac{\text{Activity of the } \mathbf{Z} \text{ catalyst}}{\text{Combined activity of the } \mathbf{Z} \text{ and } \mathbf{N} \text{ catalysts}} = \frac{x_Z A_{S\,Z}}{x_Z A_{S\,Z} + x_N A_{S\,N}} \tag{5.1}$$

$$m_N = 1 - m_Z \tag{5.2}$$

where x_Z and x_N are the molar fractions of **Z** and **N** in $_S$**ZN**, respectively, $A_{S\,Z}$ and $A_{S\,N}$ are the polymerization activities of **Z** and **N**, respectively, based on their activities when supported alone as $_S$**Z** and $_S$**N**.

For example, for Run 1 in Table 5.5,

$$m_Z = \frac{0.5 \times 3250}{0.5 \times 3250 + 0.5 \times 6810} = 0.32 \tag{5.3}$$

$$m_N = 1 - 0.32 = 0.68 \tag{5.4}$$

Overall catalyst activity, $A_{S\,ZN}$, and M_w for the whole polymer, $M_{w_S\,ZN}$, were estimated using Equations (5.5) and (5.6)

$$A_{S\,ZN} = m_Z A_{S\,Z} + m_N A_{S\,N} \tag{5.5}$$

$$M_{w_S\,ZN} = m_Z M_{w_S\,Z} + m_N M_{w_S\,N} \tag{5.6}$$

Table 5.5 compares predicted and experimental catalyst activities and weight average molecular weights for the polymers made with the $_S$**ZN** catalyst. The experimental activities are slightly lower than the calculated results, while the experimental M_w are generally higher than the predicted values. However, considering batch-to-batch variation among the supported catalysts, and considering that the **N** and **Z**

catalysts have different sensitivity to polar poisons that may be present on the support and in the reactor during polymerization, the agreement between predictions and experimental results is acceptable and indicates that the catalysts sites most likely act independently when co-supported on the same carrier.

Table 5.5. Theoretically calculated catalyst activity and M_w for $_S$**ZN** using results for $_S$**Z** and $_S$**N**.

Entry	Polymerization Conditions			Results				
	Cat.	Temp. (°C)	1-Hexene (C6/C2) [a]	(Z:N) [b]	Activity [c]		M_w (g/mol ×10^{-3})	
					Calc.	Exp.	Calc.	Exp.
1	$_S$ZN	40	0	32:68	5570	4300	189	206
2	$_S$ZN	40	0.2	25:75	5200	4110	126	141
3	$_S$ZN	40	0.4	23:77	5810	4150	116	136
4	$_S$ZN	60	0	41:59	14180	13260	130	124
5	$_S$ZN	60	0.2	36:64	11510	10430	95	83
6	$_S$ZN	60	0.4	29:71	9580	6120	79	96
7	$_S$ZN	70	0	65:35	14820	14160	128	131
8	$_S$ZN	70	0.2	64:36	9640	6870	73	100
9	$_S$ZN	70	0.4	69:31	7690	6440	80	77

[a] Mole ratio of 1-hexene/ethylene.

[b] Contributed mole fraction of **Z** and **N** on activity and M_w.

[c] Activity in kg PE/(mol Zr and Ni × h).

CEF analysis results are shown in Figure 5.9. The CCD of the polymer made with $_S$**ZN** has unique characteristics. The homopolymer (no 1-hexene comonomer added) has a trimodal CCD (A). The polymer in the high crystallinity peak (102.1°C) was made with

the **Z** catalysts, and the polymer composing the two other peaks (97.2^{o}C and 79.7^{o}C) containing SCBs produced via the chain walking mechanism was made by catalyst **N**. According to the theoretically calculated result in Entry 7 (Table 5.5), 65 % of the polymer was made by **Z**. However, the area under the high temperature peak in Figure 5.9A does not correspond to 65 % of the total polymer. Although the position of the $_{S}$**ZN** peak with the lowest elution temperature (79.7^{o}C) coincides with that for the polymer made with $_{S}$**N** (compare with Figure 5.6), the intermediate peak (97.2^{o}C) is shifted to a higher temperature. This shift indicates that cocrystallization takes place between the high-crystallinity component made by **N** and the polymer made by **Z**, as cocrystallization is commonly observed, especially for peaks with similar high crystallizabilies, in this type of analytical techniques.

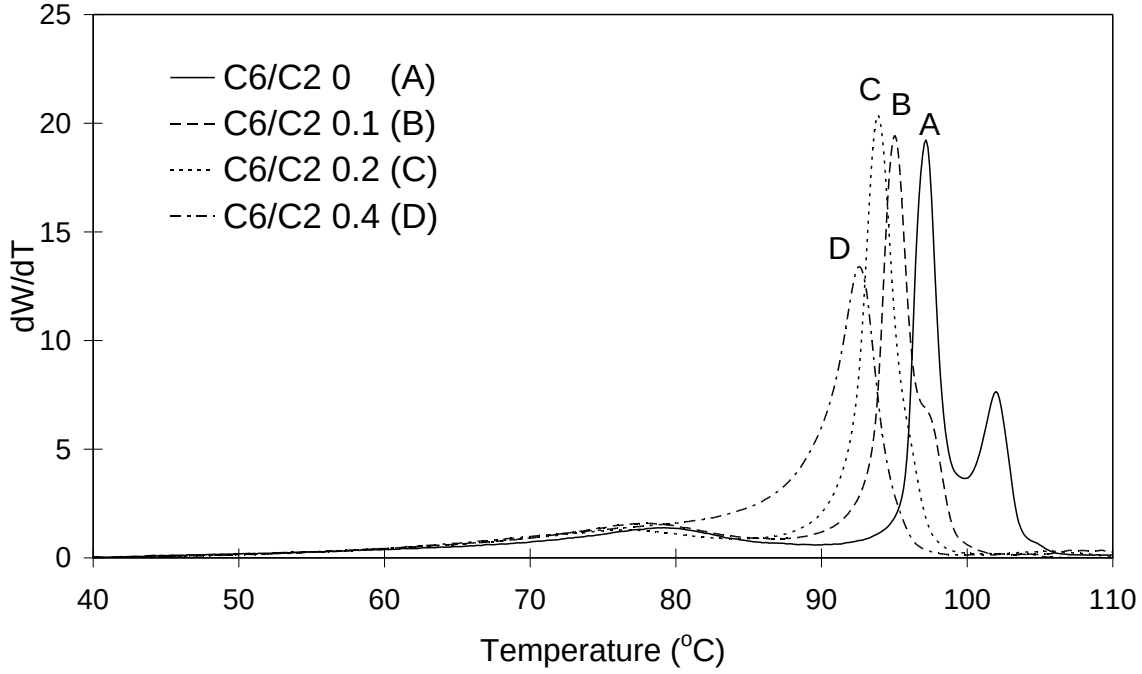

Figure 5.9. CEF (CCD) profiles of polyethylene made with $_{S}$**ZN**: A (Run 7, Table 5.4), B (Run 8, Table 5.4), C (Run 9, Table 5.4) and D (Run 10, Table 5.4).

The **Z** active sites incorporate more α-olefins than the **N** sites. As a consequence, the CEF elution temperature of the polymer made with **Z** decreases much more significantly as the 1-hexene concentration in the reactor increases. Observing how the two highest elution temperature peaks vary from A to D in Figure 5.9, we notice that the peak attributed to **Z**, initially appears well resolved in A, becomes a shoulder of the **N** peak in B, completely overlaps the **N** peak in C, and finally seems to "appear" again at a lower elution temperature in D. Interestingly, the peak located at 80°C, also attributed to catalyst **N**, hardly changes in size or shape as 1-hexene concentration is increased. This indicates that most, if not all, of the SCBs are caused by chain walking and are not affected by the presence of 1-hexene during the polymerization. Based on these CEF results, it can be hypothesized that at least three kinds of active sites are present on $_{S}$**ZN**, each with its own characteristics and contributing to make polyethylene with unique microstructural properties.

Results for ethylene polymerizations using $_{S}$**TN** are shown in Table 5.6. The catalyst activity and T_{m} of polymer are lower than for polymers made with $_{S}$**ZN** at the same polymerization conditions. On the other hand, $_{S}$**TN** made polymers with higher M_{w} and bimodal MWDs due to the presence of the **T** sites. As seen from the GPC-IR results in Figure 5.10, polymers with bimodal MWD and reverse comonomer incorporation can be made with this hybrid catalyst. A high amount of SCBs were incorporated in the higher molecular weight region of the distribution, resulting in polymers with inverse SCBD even at 40°C (Run 3, Table 5.6, and Figure 5.10a). At higher polymerization temperatures (70°C), the polymer becomes even more branched (Figure 5.10b).

Table 5.6. Results for ethylene homopolymerization and ethylene/1-hexene copolymerization using $_S$**TN**.

Run	Polymerization Conditions			Results				
	Catalyst	Temp. (°C)	1-Hexene (C6/C2) [a)]	Yield (g)	Activity [b)]	T_m (°C)	M_w (g/mol ×10^{-3})	M_w/M_n
1	$_S$TN	40	0	0.5	800	131.0	633	19.1
2	$_S$TN	40	0.2	0.6	1000	124.5	351	7.5
3	$_S$TN	40	0.4	0.5	500	122.4	301	6.8
4	$_S$TN	60	0	1.5	2300	128.2	682	29.0
5	$_S$TN	60	0.2	1.2	1800	120.8	491	16.9
6	$_S$TN	60	0.4	1.4	1700	119.3	375	12.9
7	$_S$TN	70	0	1.8	2800	128.3	595	29.8
8	$_S$TN	70	0.2	1.5	2300	119.5	345	15.6
9	$_S$TN	70	0.4	1.2	1800	119.0	309	11.3

Polymerization conditions: supported catalyst 20-30 mg, TMA 0.1 mmol, solvent 150 mL hexane, ethylene pressure 150 psig, time 15 min.

[a)] Mole ratio of 1-hexene/ethylene.

[b)] Activity in kg PE/(mol Ti and Ni × h).

a)

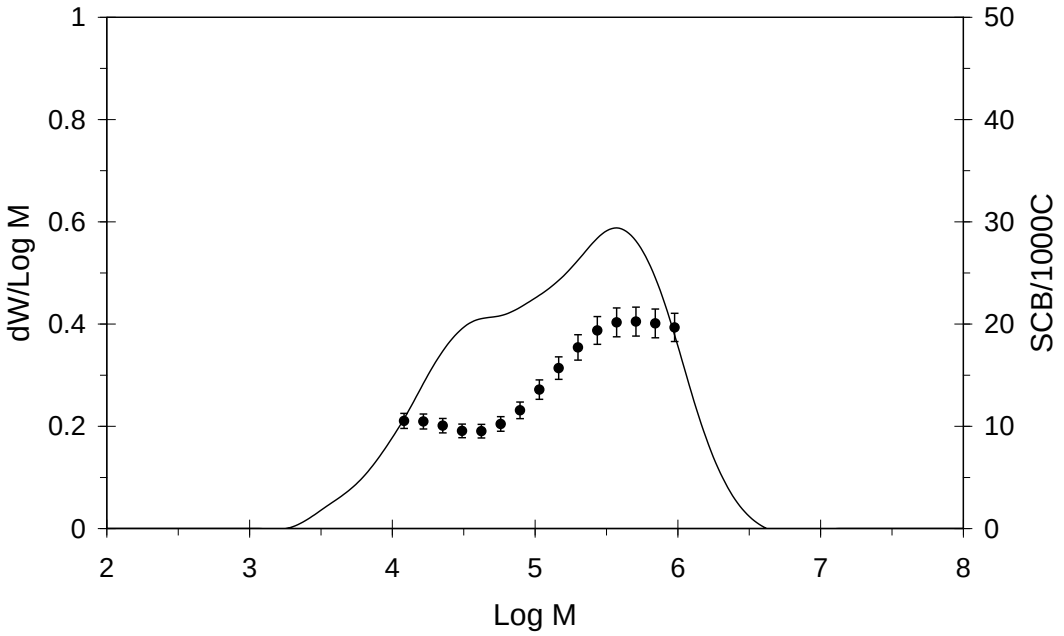

b)

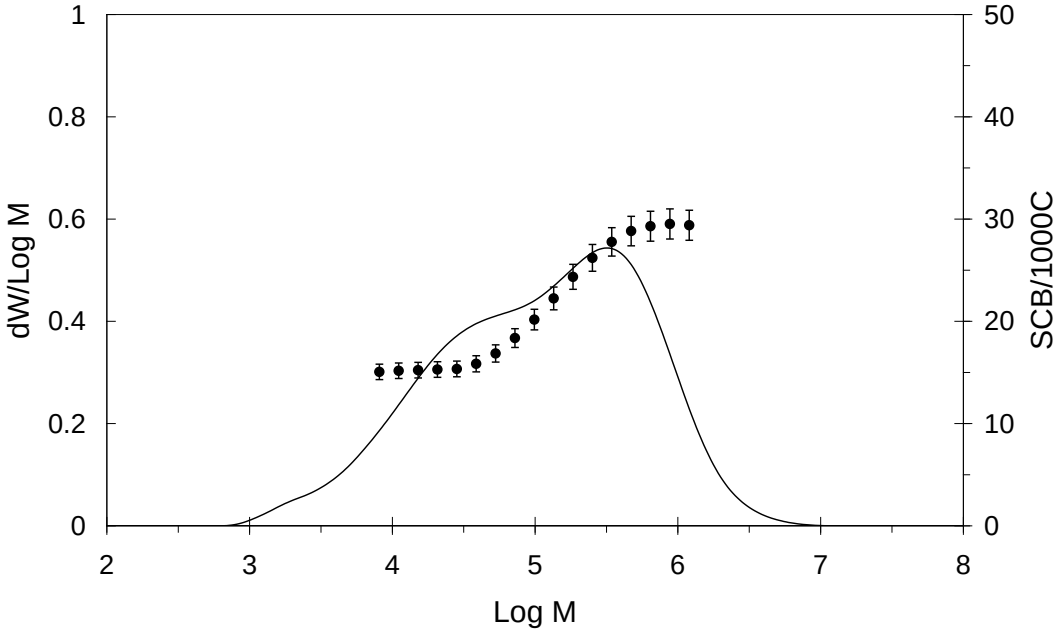

Figure 5.10. MWD and SCB frequencies for polyethylene made with $_S$**TN**. Polymerization conditions: a) 40°C, C6/C2 0.4 (Run 3, Table 5.6); b) 70°C, C6/C2 0.4 (Run 9, Table 5.6).

Figure 5.11 shows various MWD profiles of polymers made using $_S$**TN**. As the concentration of 1-hexene increases, the area under the peak corresponding to catalyst **T** increased and gradually shifted to lower molecular weight averages, but the peak location for the **N** catalyst did not change appreciably. The **T** active sites have higher reactivity ratio towards 1-hexene incorporation, and therefore the relative mass of polymer made on these sites increases as the concentration of 1-hexene is raised; however, due to transfer to comonomer, the MWD for polymer made on these sites also decreases. Site **N**, with a much lower 1-hexene incorporation ratio, is not significantly affected by the presence of the α-olefin comonomer. Thus, the MWD becomes narrower with increasing 1-hexene concentration. Most of polymers are free-flowing particles, but the polymers with the highest 1-hexene feed at 70°C are agglomerated, as seen in Figure 5.8.d.

a)

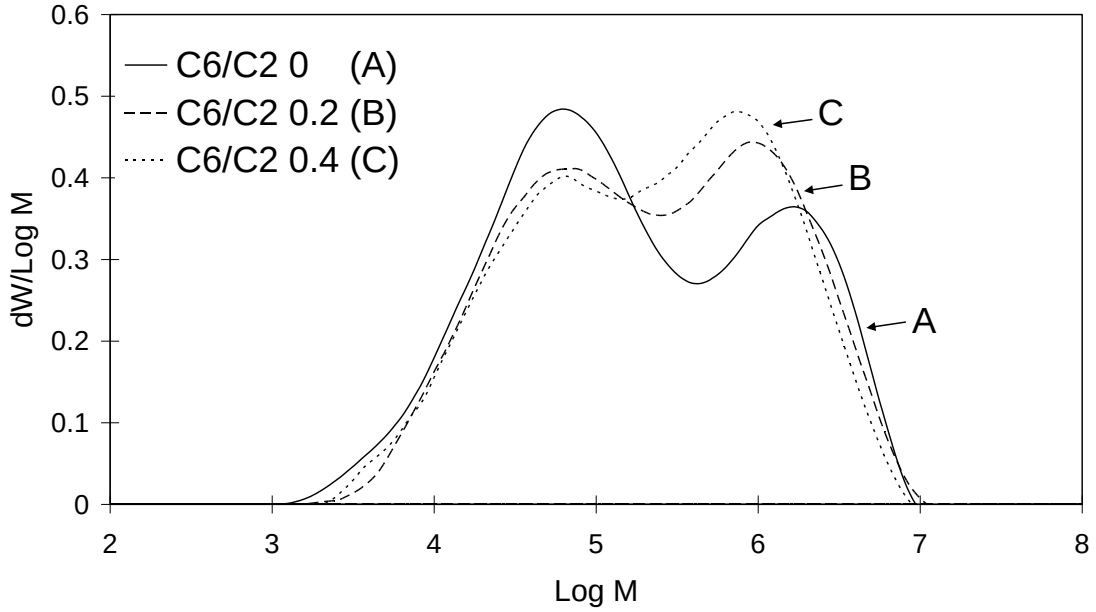

b)

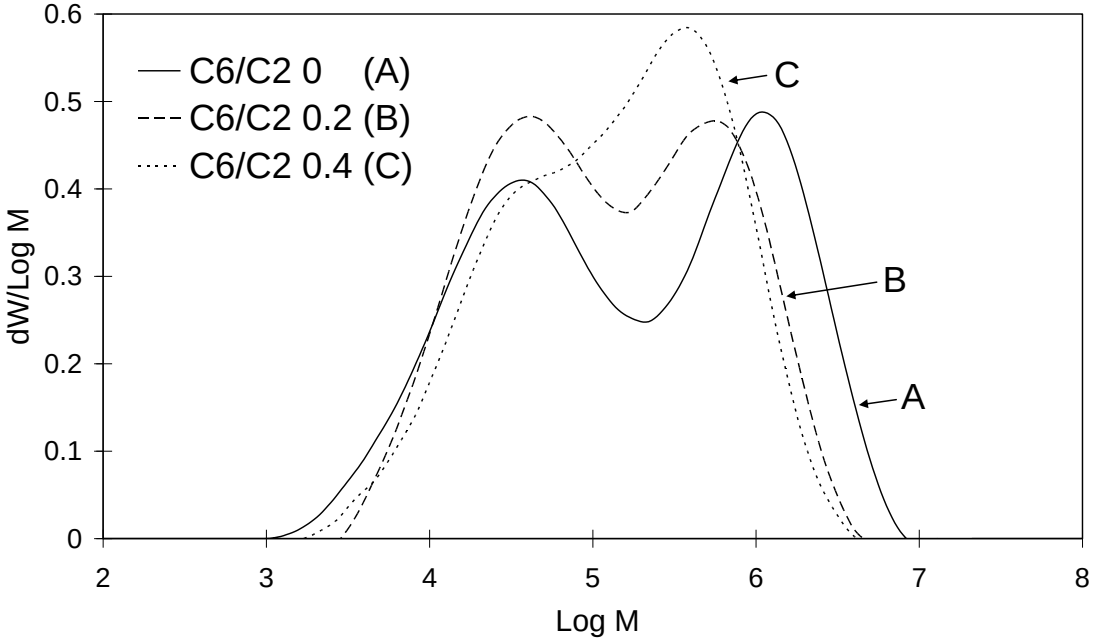

Figure 5.11. Comparison of MWDs for polyethylene samples made with $_s$**TN** at: a) 40°C (Runs 1-3, Table 5.6) and b) 70°C (Runs 7-9, Table 5.6).

Figure 5.12 shows the CEF results for the polymers made with $_S$**TN**. The CCD for the homopolymer (A) is similar to that for $_S$**ZN**. The polymer with the highest elution peak (102.1^{o}C) is made on the **T** sites (compare with CEF of polymers made with $_S$**Z** in Figure 5.3). The other two peaks at lower temperatures are for polymer made with the **N** catalyst. Adding 1-hexene to the reactor makes the peak with the highest comonomer incorporation ability (**T**) move to lower temperatures, while the peaks corresponding to the **N** catalyst are less affected, similar to what had been observed for copolymer made with the $_S$**ZN** system.

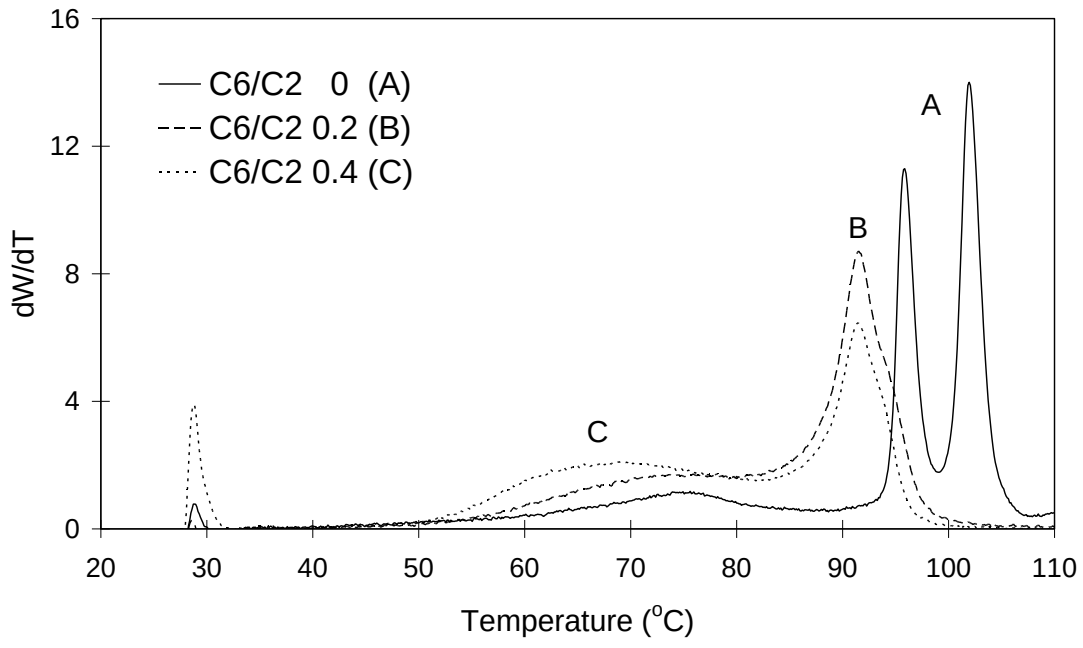

Figure 5.12. CEF (CCD) profiles for polyethylene samples made with $_S$**TN**: A (Run 7, Table 5.6), B (Run 8, Table 5.6), C (Run 9, Table 5.6).

5.3.3. SCB Characterization

The SCB distribution of these polymers was further characterized by ^{13}C NMR spectroscopy. The assignments of each characteristic chemical shifts at 20.15($1B_1$), 11.32($1B_2$), 14.75($1B_3$), 23.42($2B_4$), 22.92($2B_5$) and 31.77($3B_n$) ppm for the resultant polymers are based on chemical shift calculations according to the Lindeman and Adams method (Lindeman and Adams, 1971). Representative ^{13}C NMR results are shown in Figure 5.13. Equations used to calculate SCB/1000 C atoms and their relative ratios are given by the following equations (Usami and Takayama, 1984),

$$N(\text{total branches}/1000\text{C}) = \frac{1000(I_{Me}/0.90 + I_{Et}/0.84 + I_{Pr}/0.83 + I_{Bu}/0.90 + I_{Pe}/0/90 + I_{Lg}/0.8)}{I_{main} + 5.5(I_{Et}/0.84) + I_{Pr}/0.83 + 8.0(I_{Bu}/0.90 + I_{Pe}/0/90 + I_{Lg}/0.8)} \quad (5.7)$$

$$\text{Me:Et:Pr:Bu:Pe:Lg} = (I_{Me}/0.90):(I_{Et}/0.84):(I_{Pr}/0.83):(I_{Bu}/0.90):(I_{Pe}/0.90):(I_{Lg}/0.80) \quad (5.8)$$

where, I_{Me}, I_{Et}, I_{Pr}, I_{Bu}, I_{Pe} and I_{Lg} are the ^{13}C NMR integral intensities corresponding to $1B_1$, $1B_2$, $1B_3$, $2B_4$, $2B_5$ and $3B_n$, respectively.

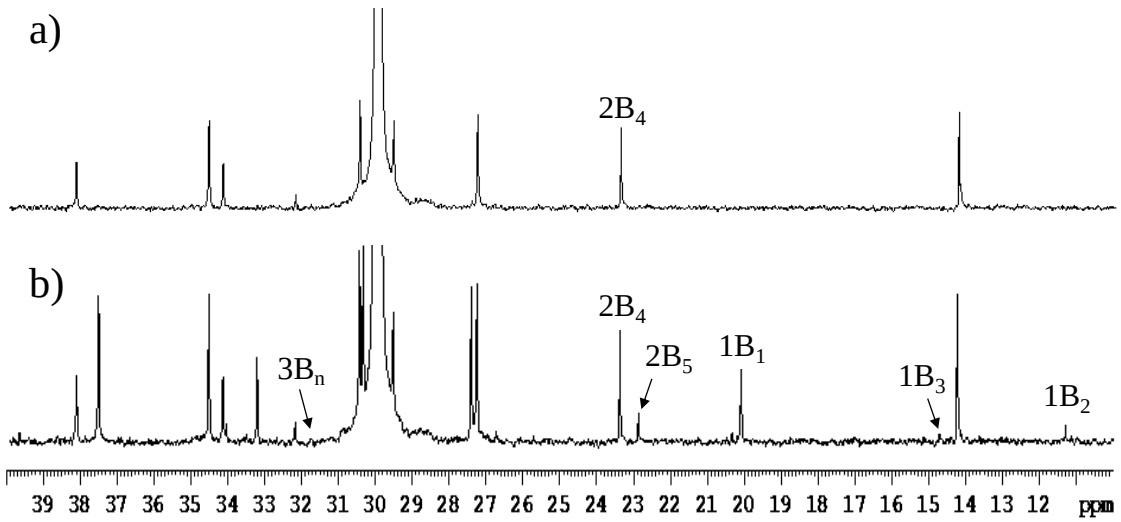

Figure 5.13. High-temperature ^{13}C NMR spectra for polyethylenes made with: a) $_{S}$**Z** (Run 9, Table 5.2), and b) $_{S}$**ZN** (Run 10, Table 5.4).

Table 5.7 shows the SCB distribution of some polymers synthesized in this study. The catalyst $_{S}$**N** makes highly branched polymers with a distribution of SCB lengths, as characteristic of the chain walking mechanism. Methyl branches predominate, but 1-hexene incorporation onto the polymer chains is much lower than that for $_{S}$**Z** (Entries 1 and 2, Table 5.7), as already observed in the several CEF profiles discussed above. The SCBs of polymers made with $_{S}$**ZN** are intermediate between the results for polymers made with $_{S}$**Z** and $_{S}$**N** (Entries 1, 2 and 5, Table 5.7), as expected. The $_{S}$**TN** catalyst makes chains with the largest SCB frequency, due to the high comonomer incorporation rate of the **T** component. As expected, butyl branches are mostly controlled by the contribution of the metallocene component (**Z** or **T**), while **N** adds an additional component with a distribution of SCB lengths, but mostly methyl branches. When **Z** is replaced with **T**, polyethylene with the highest butyl branch frequency is obtained for a given set of polymerization conditions (Entries 5 and 8, Table 5.7). In addition, the amount and types

of SCBs can be modified by changing the polymerization temperature (Entries 3 and 5, Entries 6 and 8, Table 5.7).

Table 5.7. Influence of catalyst structures and polymerization conditions on SCBD.

Entry	Polymerization Conditions			SCBs /1000C	SCBD (%)					
	Cat.	Temp. (°C)	1-Hexene (C6/C2)[a)]		Methyl	Ethyl	Propyl	Butyl	Pentyl	(n≥6)
1	$_S$Z	70	0.4	7.33	0	0	0	100	0	0
2	$_S$N	70	0.4	27.65	55.9	10.0	8.0	14.4	6.3	5.4
3	$_S$ZN	40	0.4	4.48	84.0	0	0	16.0	0	0
4	$_S$ZN	70	0	11.38	65.2	11.0	6.2	5.4	5.1	7.1
5	$_S$ZN	70	0.4	16.24	29.9	6.2	4.5	42.2	9.5	7.7
6	$_S$TN	40	0.4	14.84	25.9	0	0	74.1	0	0
7	$_S$TN	70	0	8.23	51.8	7.1	8.2	12.9	7.1	12.9
8	$_S$TN	70	0.4	28.13	13.0	2.3	2.1	71.1	4.9	6.6

[a)] Mole ratio of 1-hexene/ethylene.

5.3.4. Polymer morphology

SEM micrographs of polymer particles made with $_S$**ZN** (Run 7, Table 5.4) are shown in Figure 5.14. Two distinct particle morphologies are observed, as illustrated in Figure 5.14.a (around 80 % of total particles) and 5.14.d (around 20 % of total particles). In Figure 5.14.a, the polymer particle has a smooth surface and apparent high bulk density, while in Figure 5.14.d the particle appears more porous. Figures 5.14.b and 5.14.c zoom into a particular section of the particles, as indicated by the square box in Figure 5.14.a.

The primary particles (also called microparticles or sub-particles) consist of round fragments with diameters bellow 1 μm, and are connected through polymer fibrils. These polymer particles seem to fit the description of the multigrain model, in which secondary particles (also called macroparticles) are constituted of agglomerates of near spherical primary particles, each containing a catalyst/support grain at its center (McKenna et al., 2010).

a) b)

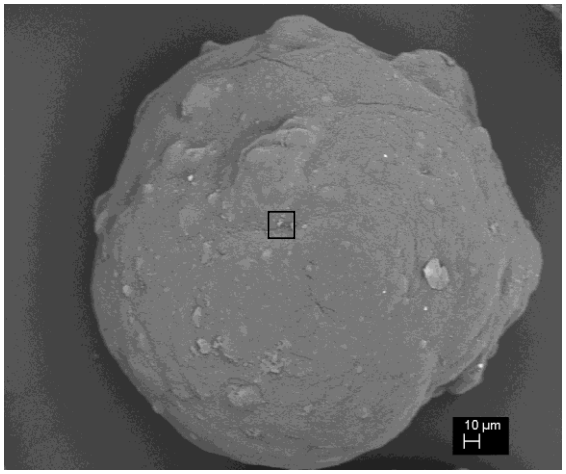

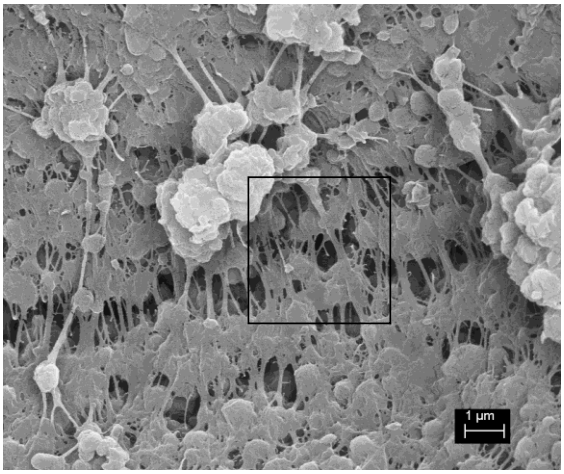

c) d)

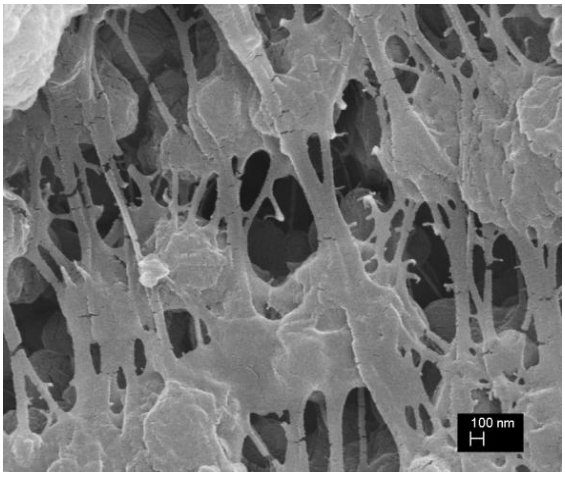

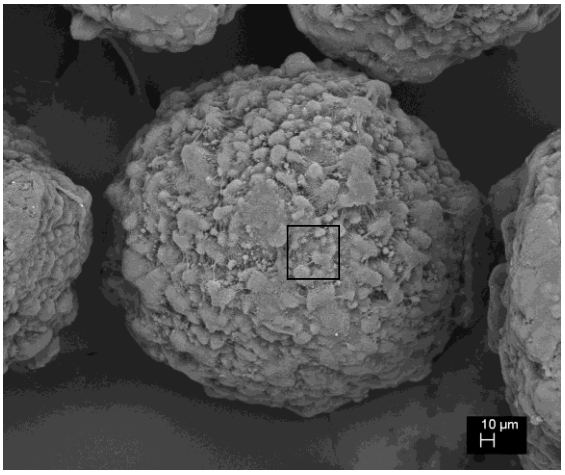

e)

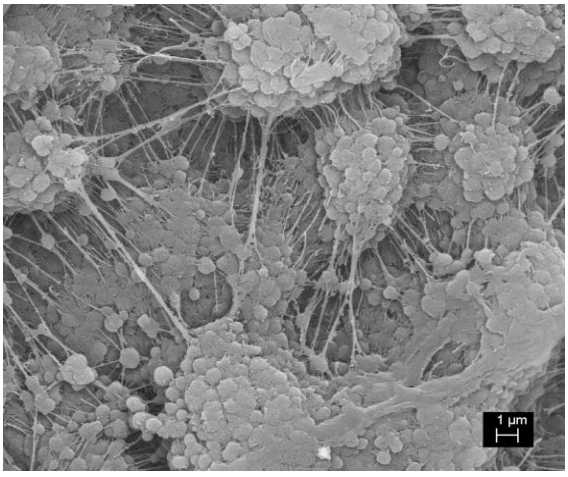

Figure 5.14. SEM micrographs of polymer particles made with $_S$**ZN** (Run 7, Table 5.4): a) External surface (scale bar 10 µm); b) A closer look at the region indicated with a square box on a) (scale bar 1 µm); c) A closer look at the region indicated with a square box on b) (scale bar 100 nm); d) Particle with different morphology from a) (scale bar 10 µm); e) A closer look at the region indicated with a square box on d) (scale bar 1 µm).

Polymer particles with the morphology shown in Figure 5.14.d were embedded in an epoxy resin and cut into 15 μm thick slices with a diamond knife. Figure 5.15.a shows the SEM micrograph of such a slice (within the white circle), and Figure 5.15.b zooms in the square box depicted in Figure 5.15.a. Irregular cluster shapes of 10-20 μm diameter replicate the external morphology shown in Figure 5.14.e. The region indicated by a square box in Figure 5.15.b is seen in higher magnification in Figure 5.15.c, showing that some of the observed clusters have slightly different morphologies. The polymer shown in the upper part of the figure looks denser, and polymer fibrils are not observed. On the other hand, polymer fibrils are seen at the lower portion of the figure, which also looks less dense. This non-uniformity may be caused by non-uniform distribution of **Z** and **N** sites in the polymer particle.

a) b)

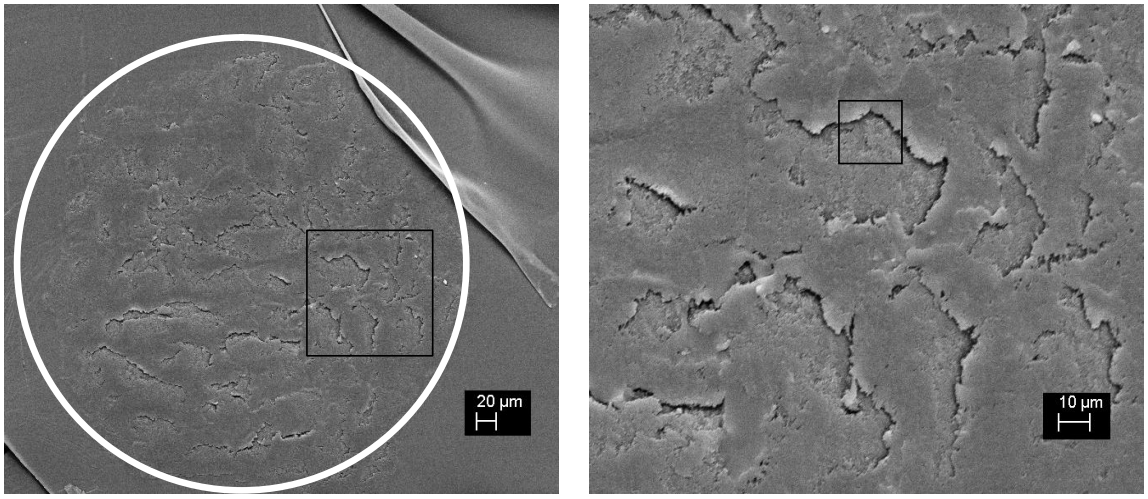

c)

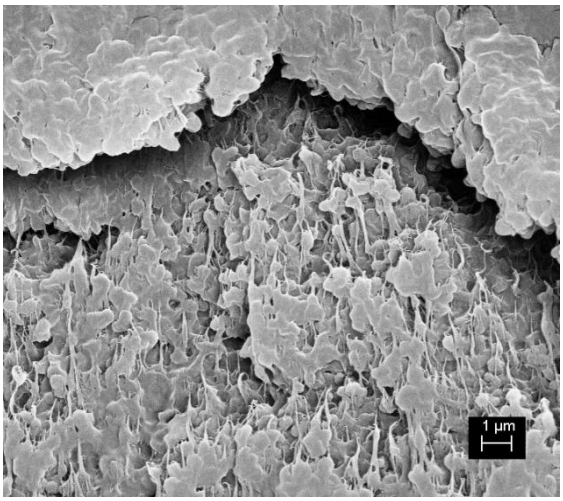

Figure 5.15. SEM micrographs of a microtomed slice of a polymer particle made with $_{S}$**ZN** (Run 7, Table 5.4): a) A sliced particle (inside white circle, scale bar 20 µm); b) A closer look at the region indicated with a square box on a) (scale bar 10 µm); c) A closer look at the region indicated with a square box on b) (scale bar 1 µm).

5.4. Conclusion

Functionalized early and late transition metal catalysts were supported onto SiO_2 and used for ethylene homopolymerization and ethylene/1-hexene copolymerization. GPC-IR and CEF results revealed that when these catalysts were co-supported, they behaved independently of each other. The hybrid supported catalyst systems were very effective for tailoring the polyethylene microstructure. Polymers with a distribution of SCB lengths were produced without addition of α-olefin by the nickel diimine catalyst via the chain walking mechanism, while the metallocene component needed α-olefin to produce short chain branched macromolecules. The combination of **Z**, **T** and **N** catalysts having unique characteristics led to polymers having broad and bimodal MWD and trimodal CCD. Depending on the polymerization conditions, an inverse distribution of SCBs across the MWD, where the SCB frequency increases with increasing molecular weight, could be obtained.

The formation of free-flowing polymer particles confirms that the catalyst sites were strongly supported onto SiO_2. Furthermore, SEM micrographs showed that the polymer particles had spherical morphology and apparent high bulk density. Thus, these hybrid catalysts seem to be adequate for “drop-in” operations and may be used directly in most commercially available slurry or gas-phase processes.

Chapter 6 : Preparation of Polyethylene/MMT Nanocomposites Through In Situ Polymerization Using a Montmorillonite-Supported Nickel Diimine Catalyst

6.1. Introduction

Nanocomposites made with layered silicates such as montmorillonite (MMT) have been studied extensively since polyamide/layered silicate nanocomposites were found to have remarkably improved properties, such as increased tensile strength, heat resistance, and gas barrier properties, as compared with those of the equivalent virgin polymers or their conventional composites (Ray and Okamoto, 2003; Usaki et al., 1997). More recently, the success on these nanocomposites has been extended to high performance polyolefin nanocomposites, resulting in sizeable improvements in mechanical performance (Mishra et al., 2005). However, polyolefins such as polyethylene and polypropylene are hydrophobic and do not mix well with hydrophilic MMT layered silicates. To render MMT more miscible with hydrophobic polymers, one must transform the normally hydrophilic clay surface to an organophilic surface.

Polyolefin/MMT nanocomposites, prepared by conventional melt compounding, generally form MMT agglomerates that lead to the premature breakdown of the material because of the tendency of the MMT particles to phase-separate from the polymer matrix. Compounding processes for the production of polyolefin/MMT nanocomposites require the use of expensive maleated polyolefins and surfactant-intercalated MMTs, which are utilized to overcome the incompatibility between polyolefins and MMTs. Nevertheless, not only costly changes in plant infrastructure are required, but also the thermal stability of intercalated MMT is taken into consideration in the melt compounding process (Usaki et al., 1997; Sun and Graces, 2002).

In situ polymerization, which employs the dispersion of nanoscale fillers in the reaction medium before and during polymerization, has been investigated as a more efficient way of making nanocomposites than melt compounding (Bergman et al., 1999; Dubois et al., 2003; Heinemann et al., 1999).

This chapter describes the preparation of polyethylene nanocomposites using MMT-supported nickel diimine catalysts. The principle of catalyst intercalation is similar to those used in traditional supporting methods for olefin polymerization catalysts: firstly, it is necessary to immobilize the catalyst on the MMT support; then, the formation and dispersion of MMT nanophase layers in the polyethylene matrix is made by in situ polymerization.

6.2. Experimental

6.2.1. Materials

Three kinds of MMTs (Cloisite Na^+, Cloisite 30B, and Cloisite 93A) were purchased from Southern Clay Products and used after drying under vacuum at 60°C overnight. The structures of the organic modifiers used in Cloisite 30B and Cloisite 93A are shown in Figure 6.1.

The other experimental materials used in the experiments described in this chapter are the same as described in Section 3.2.1.

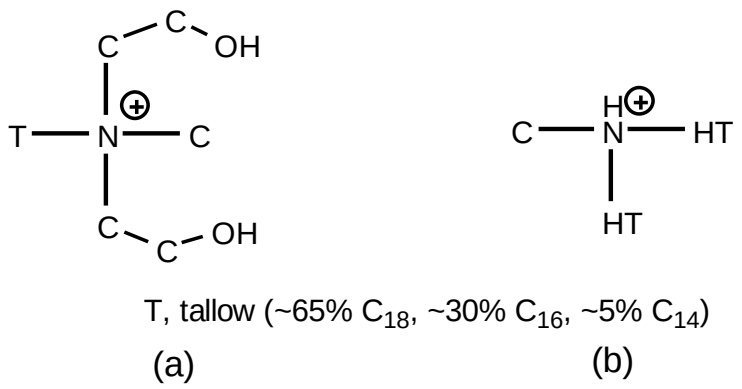

Figure 6.1. Structure of organic modifiers: a) Methyl tallow bis-2-hydroxyethyl ammonium (Cloisite 30B); b) Methyl di-hydrogenated tallow ammonium (Cloisite 93A).

6.2.2. Nanocomposite Characterization

Thermogravimetric analysis (TGA, Q500, TA Instruments) was done under nitrogen atmosphere with a heating rate of 10°C/min and used to determine the maximum decomposition temperature (T_d) of the modified MMTs and nanocomposites. The *d*-spacing information was obtained with an X-ray diffractometer (XRD, D8-Focus, Bruker)

using a Cu K_α radiation (λ = 0.154 nm) beam. A LEO 1530 scanning electron microscope (SEM) and a transmission electron microscope (TEM, CM12, Phillips) were used to investigate the morphology and the dispersion of MMT layers in the nanocomposites. For the TEM analysis, the produced nanocomposite particles were embedded onto an epoxy resin and cut into slices of 80 nm thicknesses with a diamond knife. Other characterization methods are the same as described in Section 3.2.6.

6.2.3. Synthesis of the MMT-supported nickel diimine catalysts

A mass of 2.5 g of dried Cloisite Na^+ and 7.4 mmol of TMA were introduced sequentially into a dried 225 mL glass reactor equipped with a mechanical stirrer. The reactor was heated at 40°C under a stirring rate of 200 rpm and the reagents were allowed to react for 15 hours. At the end of the reaction, the supernatant was removed with a cannula. A volume of 50 mL toluene was introduced to the particles, stirred for 5 minutes, and then the liquid phase was removed with a cannula. After one more washing with 50 mL toluene, the particles were washed with 50 mL dichloromethane. A mass of 80 mg of **N2** was then dissolved in 20 mL dichloromethane, added to the TMA-treated MMT particles, and allowed to react for 15 hours. After the catalyst particles were precipitated, the black color of **N2** solution disappeared and the transparent solvent phase separated. This procedure confirmed that **N2** was completely supported onto MMT. The supported catalyst was filtered, washed with 20 mL dichloromethane, and then dried under vacuum. The final supported catalyst was named **CNa**. Supported catalysts **C30B** and **C93A** were synthesized according to the same procedure, using Cloisite 30B and Cloisite 93A in place of Cloisite Na^+, respectively.

6.2.4. In Situ Polymerization

Polymerizations procedures were the same as described in Section 4.2.5.

6.3. Results and Discussion

6.3.1. Structure of MMT-supported Nickel Diimine Catalysts

Scheme 6.1 describes the proposed steps for the synthesis of **C30B** and the PE/MMT nanocomposites made with this catalyst. Most of the TMA added during the support treatment step is expected to react with the hydroxyl groups of the organic modifier (Figure 6.1.a) or present on the clay surface. It is supposed that the **N2** complex added during the catalyst supporting step will be intercalated between the clay galleries, where their NH_2 functional groups will react with the TMA-treated support and modifier, creating strong covalent bonds that will help avoid catalyst leaching during the polymerization, thus resulting in the formation of well exfoliated nanocomposites, as also illustrated in Scheme 6.1. The synthesis of **CNa** and **C93A** catalysts should proceed in a similar way, with the difference that TMA can only react with hydroxyl groups present on the clay surface, since Cloisite Na^+ has no organic modifier and the modifier employed with Cloisite 93A (Figure 6.1.b) does not have functional groups that can react with the NH_2 groups of the catalyst ligands.

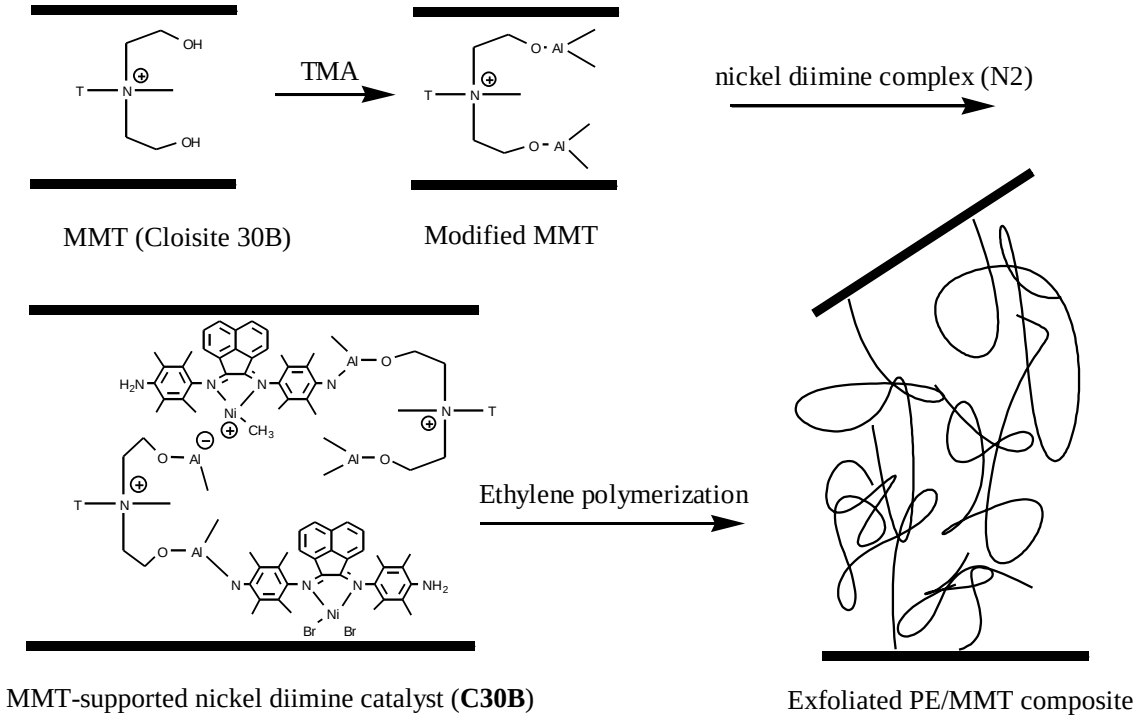

Scheme 6.1. Preparation steps for **C30B** and PE/MMT nanocomposites.

TGA derivative curves for dried MMTs and MMT-supported nickel diimine catalysts are shown in Figure 6.2. No TGA events were detected for Cloisite Na^+ and **CNa** from 100 to 500°C. The T_d (main event) for **C93A** is located at 400°C, approximately 30°C higher than that for Cloisite 93A. The TGA profile for Cloisite 30B is bimodal (with events at 260°C and 360°C); on the other hand, **C30B** has a unimodal TGA derivative profile with a single event at 390°C. Weight changes in the range from 100°C to 500°C are 1.8 % higher for **CNa** (4.5 %) than for Cloisite Na^+ (2.7 %), 2.3 % higher for **C30B** (22.9 %) than for Cloisite 30B (20.6 %), but 2.4 % lower for **C93A** (26.5 %) than for Cloisite 93A (28.9 %). While the increased weight loss for **CNa** may be attributed to the presence of the supported catalyst and TMA treatment, the weight changes for **C30B** and **C93A** also depend on the removal of part of the organic modifier during the supporting

process (Lee et al., 2005). It was reported that the TGA derivative curve for Cloisite 30B had two events below 500°C, one corresponding to the decomposition of the organic modifier molecules and the other to the decomposition of the organic modifier cations (McLauchlin and Tomas, 2009). By comparing Figures 6.2.a and 6.2.b for Cloisite 30B and **C30B**, it is hypothesized that the event at 270°C was eliminated during the supporting process because it was caused by organic modifier molecules that interacted weakly with the MMT support. On the other hand, the characteristic event of the organic modifier cations (360°C) is shifted to a higher temperature (390°C), perhaps indicating that the structure of the organic modifier was modified due to the presence of (or reaction with) **N2** molecules, as proposed in Scheme 6.1. The equivalent change in the T_d of Cloisite 93A and **C93A** indicates that a similar phenomenon takes place in this system as well.

a)

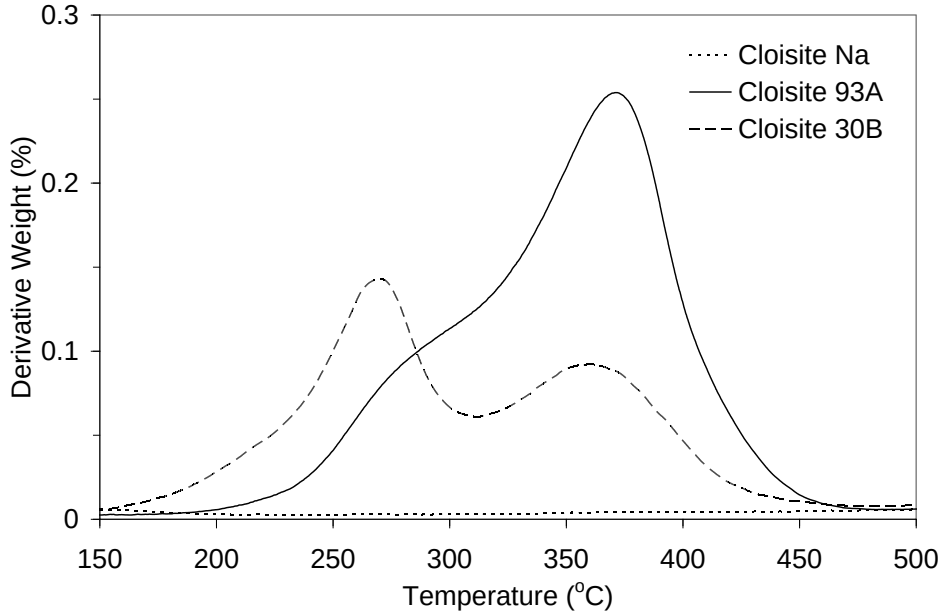

b)

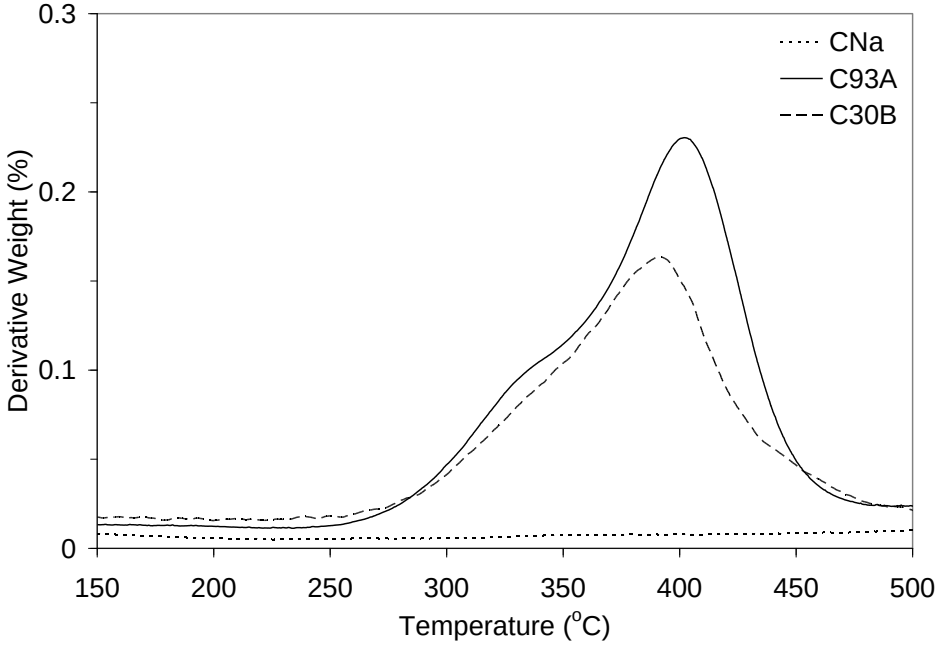

Figure 6.2. TGA analysis results: a) Dried MMTs; b) MMT-supported nickel diimine catalysts.

The XRD patterns are shown in Figure 6.3. The *d*-spacings for **CNa** and Cloisite Na are the same (Figure 6.3.a), indicating that no appreciable intercalation took place during catalyst supporting. On the other hand, the XRD results for **C93A** (Figure 6.3.b) show a smaller band shifted to a wider angle at $2\theta = 4.1^{o}$, as compared to the XRD of Cloisite 93A, suggesting that some of the galleries might be intercalated/exfoliated, while some galleries collapsed during the support treatment. Interestingly, the characteristic band of Cloisite 30B at $2\theta = 4.9^{o}$ corresponding to a *d*-spacing of d_{001} = 18.0 Å disappeared, and new diffraction bands appear for **C30B** at $2\theta = 4.1^{o}$ and 7.6^{o}, corresponding to *d*-spacings of d_{001} = 21.6Å and 11.6 Å, respectively (Figure 6.3.c). These results indicate that some galleries were exfoliated due to the reactions with alkylaluminum and **N2**, while some galleries collapsed after the supporting process.

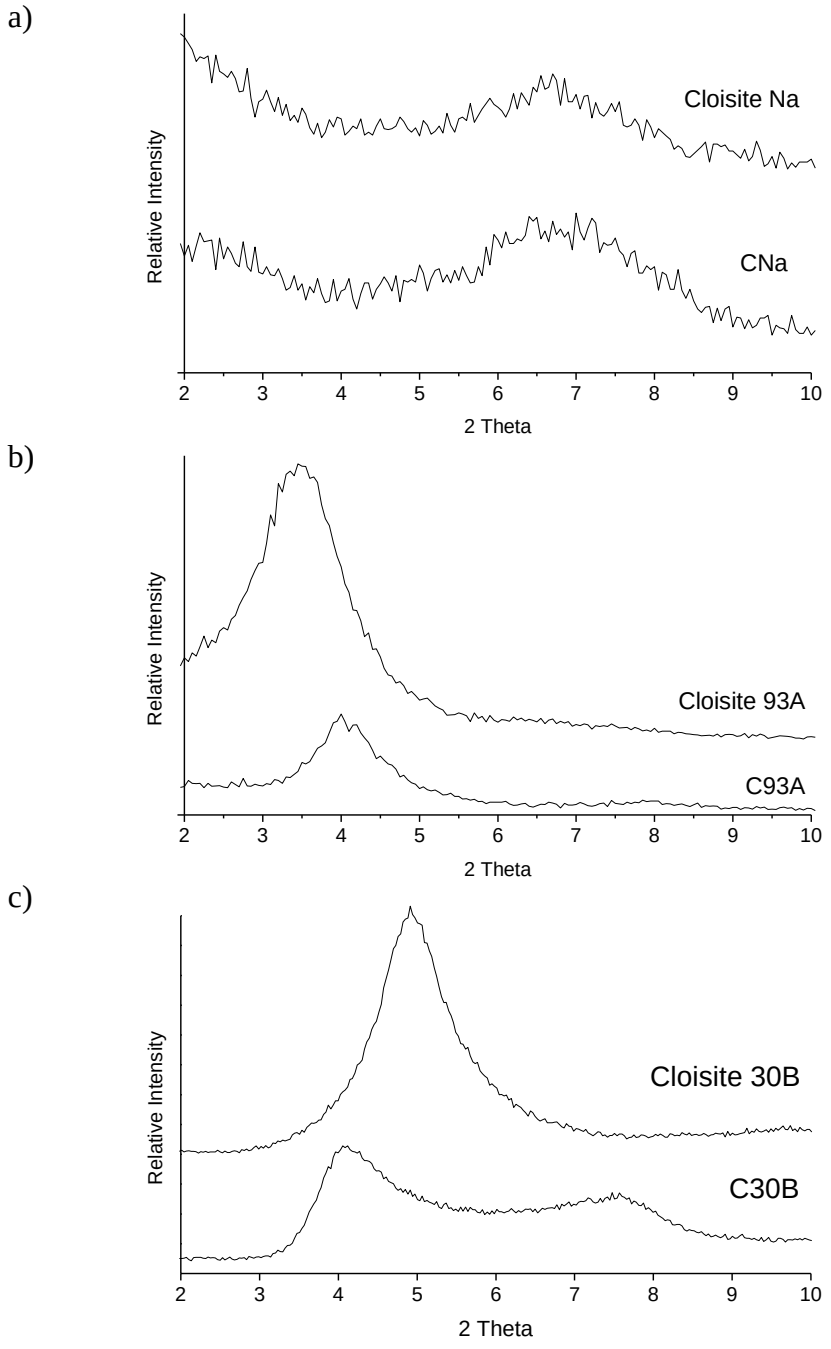

Figure 6.3. X-ray diffraction patterns of the MMTs and MMT-supported **N2** catalyst: a) Cloisite Na and **CNa**, b) Cloisite 93A and **C93A**, c) Cloisite 30B and **C30B**.

6.3.2. In Situ Polymerization

Table 6.1 summarizes the results of ethylene polymerizations using MMT-supported **N2** catalysts under various polymerization conditions. The polymerization with unsupported **N2** catalyst (Run 1, Table 6.1) was used as a reference. A series of nanocomposites with different MMT fractions were prepared by varying the polymerization time. EASC was used as the catalyst activator.

Interestingly, while EASC is required for the polymerization of ethylene with **CNa** and **C93A**, polymerizations with **C30B** in the absence of EASC have activities that are similar to those done in the presence of EASC under the same reaction conditions (compare, for instance, Run 7 and Run 9, Table 6.1). In case of polymerizations with **C30B** in the absence of EASC, it is speculated that the aluminoxane linkage generated through the reaction of TMA molecules and hydroxyl groups present in the alkyl ammonium modifier, as proposed in Scheme 6.1, could function as activators for the **N2** catalyst (Simplicio et al., 2004).

Table 6.1. Ethylene polymerization results using MMT-supported nickel diimine catalysts.

Run	Polymerization conditions				Results				
	Catalyst	Activator	Time (min)	Ethylene (psig)	Yield (pol.+cat., g)	MMT (wt.-%) [a)]	T_m (°C)	T_d (°C)	Crystallinity (%)
1	N2	EASC	55	20	1.2	0	119.9	473.4	1.0
2	CNa	EASC	40	20	1.2	13.0	115.3	414.0	2.2
3	CNa	EASC	60	20	2.4	6.4	118.0	425.5	4.6
4	C93A	EASC	15	20	1.5	13.3	119.5	420.1	4.2
5	C93A	EASC	60	20	2.5	6.0	118.6	427.0	2.6
6	C30B	EASC	8	20	0.6	23.0	122.4	378.3	7.5
7	C30B	EASC	30	20	1.7	12.7	122.7	450.2	6.1
8	C30B	EASC	45	20	2.7	6.8	123.1	445.7	10.3
9	C30B	Not used	30	20	1.1	14.3	125.0	476.0	31.7
10	C30B	Not used	100	20	2.4	8.3	125.6	475.2	33.2
11	C30B	Not used	225	20	4.1	3.8	126.8	476.7	37.1
12	CNa	EASC	3	50	1.2	13.0	122.7	404.0	28.0
13	CNa	EASC	6	50	2.4	5.4	122.8	427.5	32.1
14	C93A	EASC	2	50	1.5	12.0	122.3	390.1	12.0
15	C93A	EASC	4	50	2.5	5.1	122.1	418.7	17.5
16	C30B	Not used	6	50	0.6	16.7	125.3	473.6	34.6
17	C30B	Not used	15	50	1.0	10	125.9	467.1	34.9
18	C30B	Not used	21	50	1.6	6.5	126.3	477.3	35.1

Polymerization conditions: catalyst 100-200 mg, temperature 60°C, EASC 2 mmol, 0.1 TIBA mmol added as scavenger in Runs 9-11 and Runs 16-18.

[a)] Determined using the mass of MMT and final polymer yield.

Figure 6.4 compares the ethylene uptake profiles for polymerizations with the homogeneous **N2** catalyst and with the supported **C30B** system (Run 1 and Run 11, Table 6.1). Notice that the initial decay in ethylene flow rate is only a reflection of solvent saturation by ethylene and does not imply fast catalyst activity decay. The **C30B** system is clearly more stable than the equivalent unsupported **N2** complex. The formation of more stable nickel diimine sites by supporting onto SiO_2 carriers has also been observed in Chapter 3.

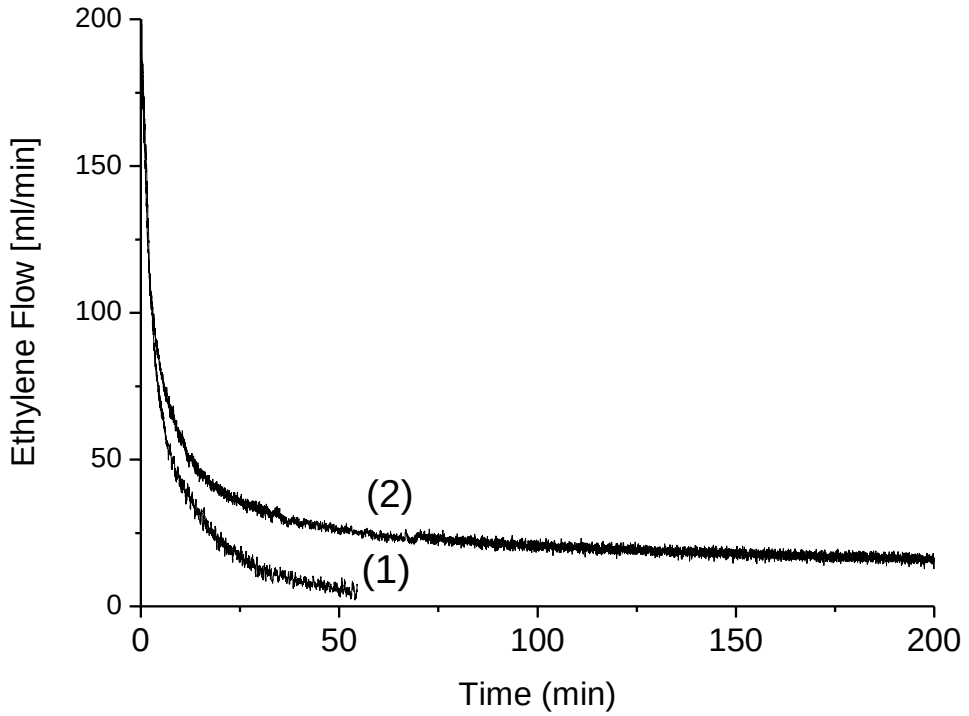

Figure 6.4. Comparison of ethylene uptake rates as a function of polymerization time: 1) Unsupported **N2** catalyst (Run 1, Table 6.1); 2) **C30B** (Run 11, Table 6.1).

The degree of crystallinity of the produced nanocomposites was determined with respect to the fraction of MMT using the theoretical melting enthalpy of 100 % crystalline

polyethylene as a reference (Reddy and Das, 2006). Surprisingly, the PE/**C30B** nanocomposites made without activator had the highest T_m and crystallinities of all other nanocomposites or homogeneous polyethylene samples made with the **N2** catalyst. This may be due to strong steric effects present inside the galleries of **C30B**, resulting in a significant reduction in the chain walking frequency, and therefore leading to the formation of polyethylene chains with fewer short chain branches, higher crystallinities, and higher melting temperatures.

For the PE/**C30B** nanocomposites (Runs 6-8, Runs 9-11 and Runs 16-18, Table 6.1), T_m and crystallinity increase for longer polymerization times (or lower MMT loadings), but this trend is not so clear for the other nanocomposites shown in Table 6.1. This increase in T_m and crystallinity with decreasing MMT weight fraction in the PE/**C30B** nanocomposites may be related to different nucleating capabilities of the MMT galleries as a function of their exfoliation degree. As expected, higher ethylene pressures made nanocomposites with higher T_m due to decreased chain walking frequency (lower SCB formation).

Figure 6.5 shows TGA derivative curves for several PE/MMT nanocomposites with different clay loadings. The T_d of most nanocomposites was significantly lower than that of the reference homogeneous polyethylene resin (473.4^{o}C), except for the PE/**C30B** nanocomposites, demonstrating again that this system has indeed special properties. It has been reported that the presence of alkyl modifiers in the MMT contributes to the degradation of polyethylene at lower temperatures. Moreover, as the PE/**CNa** nanocomposites demonstrate, MMT itself seems to accelerate the degradation of polyethylene. On the other hand, some PE/**C30B** nanocomposites made without EASC

activator had decomposition temperatures that were even slightly higher than that of the reference homogeneous resin; such behavior might be attributed to the good dispersion of the MMT galleries in the polymer matrix, resulting in enhanced thermal stability of the nanocomposites (Zhu et al., 2001). Regardless of the type of MMTs used, T_d increases and the derivative TGA curves become narrower, as the polymerization time increases and the MMT content decreases.

The XRD patterns of several PE/MMT composites are compared in Figure 6.6 and 6.7. The *d*-spacing for PE/**CNa** nanocomposites (Figure 6.6.a) increases from d_{001} = 15.0 Å to d_{001} = 19.6 Å, as the MMT fraction decreases from 13.0 % to 6.4 %. A longer polymerization time exfoliates the galleries due to polymer formation in the intergallery spaces, but the detection of *d*-spacing of d_{001} = 19.6 Å for clay content as low as 6.4 % indicates that Cloisite Na^+ does not fully exfoliate. A similar trend was observed for PE/**C93A** nanocomposites (Figure 6.6.b), indicating that even for the nanocomposite with the lowest MMT fraction, the MMT layers in PE/**C93A** were not fully exfoliated, although the XRD bands were smaller and broader than those for PE/**CNa**. In the case of PE/**C30B** nanocomposites made in the presence of EASC (Figure 6.7.a), the event at $2\theta = 5.8^o$ (d_{001} = 15.2 Å) practically disappeared as the polyethylene fraction increased. A similar trend was observed when PE/**C30B** was made without EASC (Figure 6.7.b): the broad diffraction band shifted to lower angles at higher polymerization time, indicating an increase in MMT exfoliation due to polymer formation.

a)

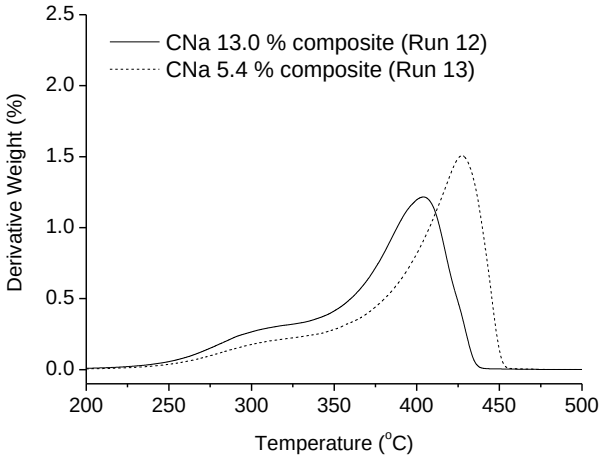

b)

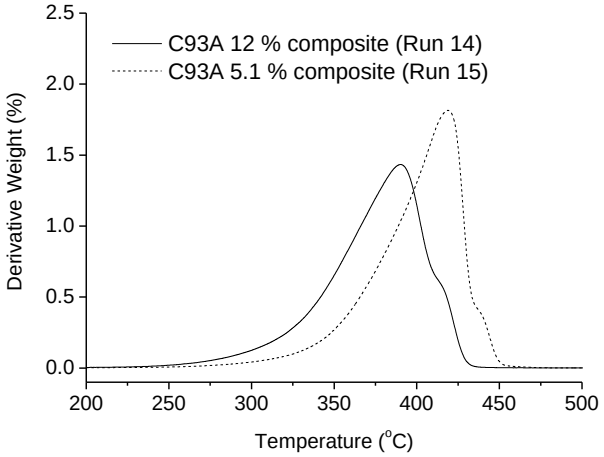

c)

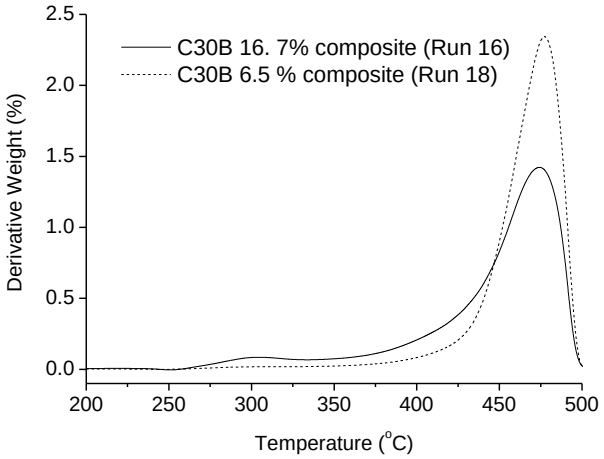

Figure 6.5. Influence of MMT fraction of the derivative TGA curves for: a) PE/**CNa**; b) PE/**C93A**; and c) PE/**C30B**.

a)

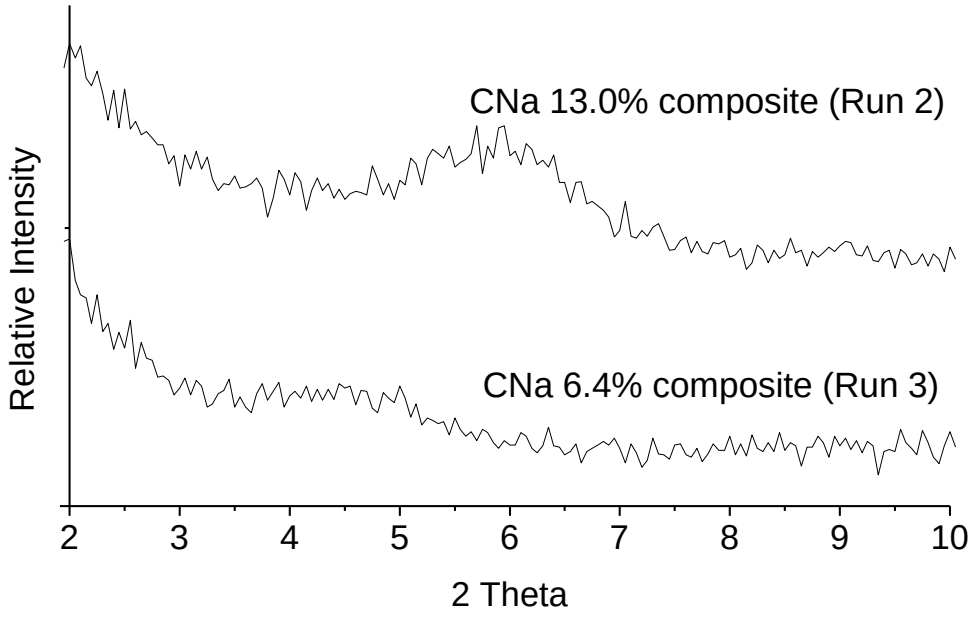

b)

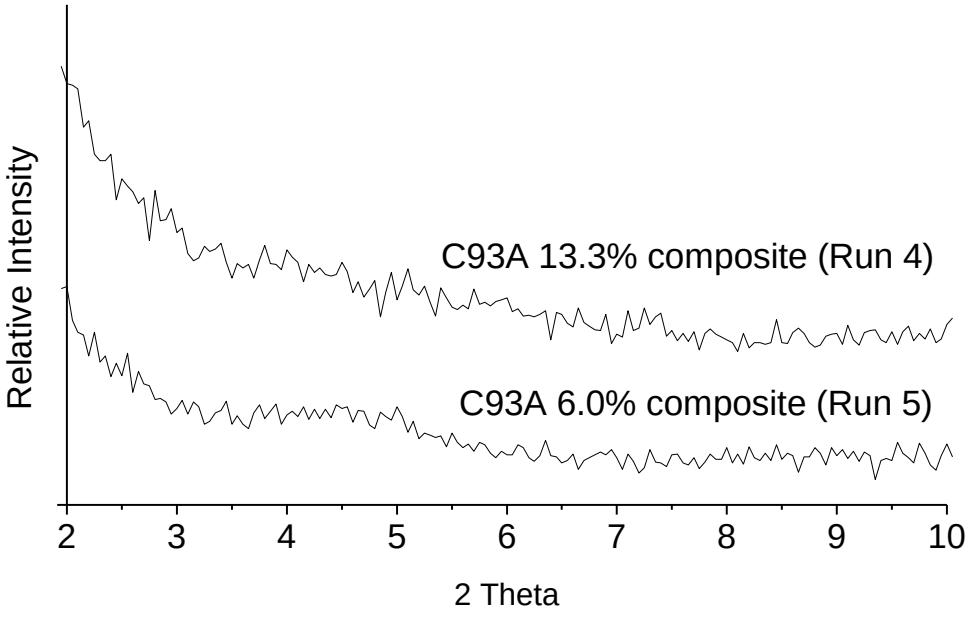

Figure 6.6. X-ray diffraction patterns of nanocomposites using MMT-supported nickel diimine catalysts: a) PE/**CNa**; b) PE/**C93A**.

a)

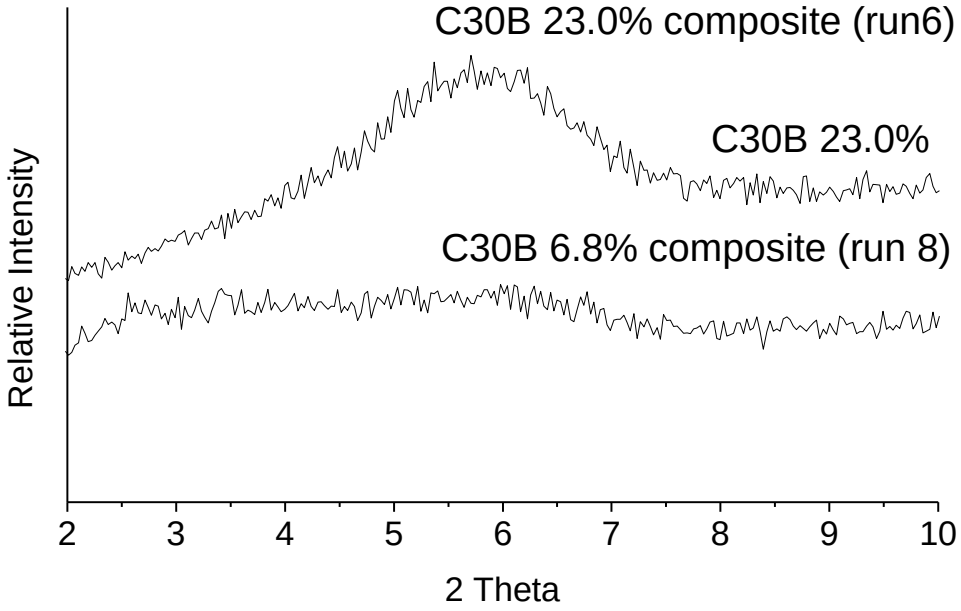

b)

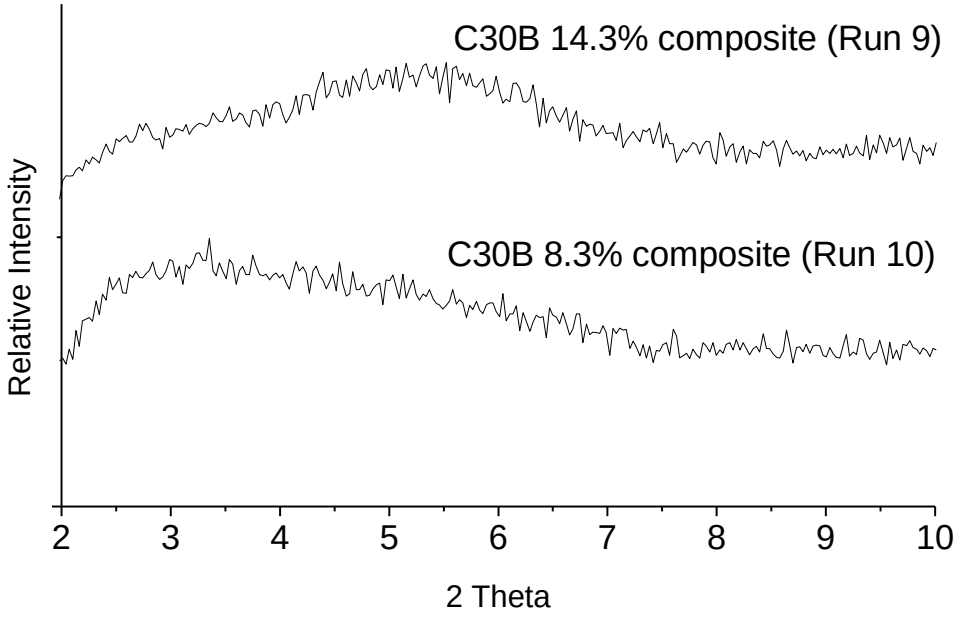

Figure 6.7. X-ray diffraction patterns of nanocomposites using a MMT-supported nickel diimine catalyst: a) PE/**C30B** with activator; b) PE/**C30B** without activator.

Figure 6.8 shows SEM micrographs of **C30B** and PE/**C30B** nanocomposites. Figures 6.8.a and 6.8.b are images of **C30B**, showing irregular particles in the 2~3 μm width range, several hundreds of nanometers thick. Figure 6.8.b, the expanded view of Figure 6.8.a, shows that the edges of the **C30B** particles are "curly", indicating that MMT layers have been intercalated and exfoliated by diffusion of the reactants from their edges to their centers during the supporting process. As a result, **C30B** particles have tactoid structures with increased *d*-spacing, as already observed in Figure 6.3.c. The morphology of the PE/**C30B** nanocomposite (Run 10, Table 6.1) is depicted in Figures 6.8.c and 6.8.d. There was no reactor fouling during the polymerization, and the resulting nanocomposite powder was "free-flowing" and composed of rough and flaky particles with a relatively broad particle size distribution, as shown in Figure 6.8.c. In the expanded view of PE/**30B** (Figure 6.8.d), the MMT layers appear as stacks connected by polymer strips and fibrils of different lengths and width. These polymer strips were further investigated by TEM, as shown in Figure 6.9.

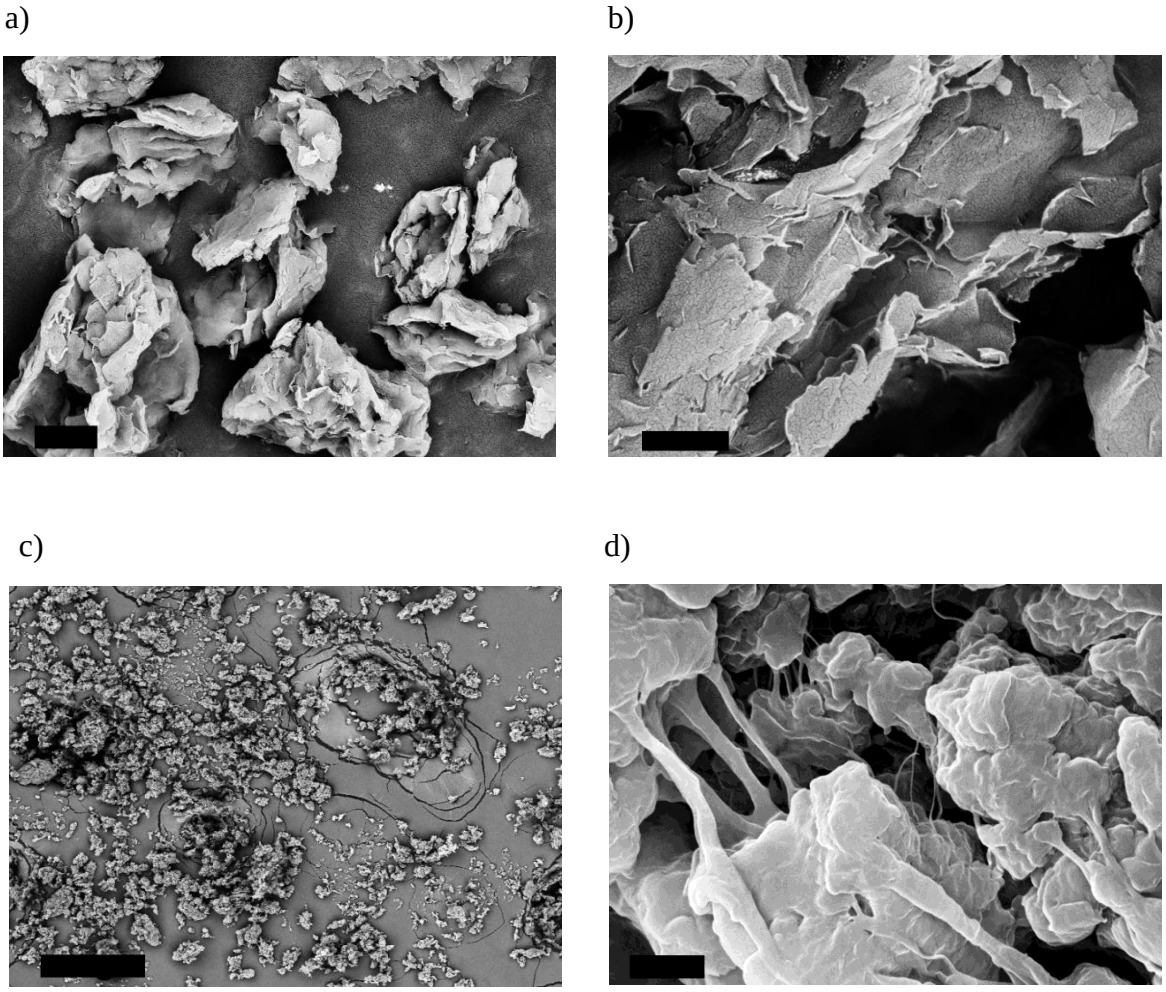

Figure 6.8. SEM micrographs: a) **C30B** (scale bar 1 µm); b) Expanded view of a) (scale bar 0.4 µm); c) PE/**C30B** nanocomposite (Run 10 in Table 6.1, scale bar 200 µm); d) Expanded view of c) (scale bar 0.5 µm).

TEM images of PE/**C30B** nanocomposites are presented in Figure 6.9 to complement the SEM image shown in Figure 6.8.d. Figure 6.9.a shows the image of a sliced plane, with particle fragmentation similar to that of the SEM image shown in Figure 6.8.d. Dark areas are those where the fraction of MMT is the highest. The regions indicated as 1, 2 and 3 are seen in higher magnification in Figures 6.9.b, 6.9.c and 6.9.d. Figure 6.9.b shows that the MMT layers are oriented in planes that are approximately parallel to the slicing plane, appearing as dark regions in the center of the image. On the other hand, the MMT layers are oriented perpendicularly to the slicing plane in Figure 6.9.c, showing very good exfoliation. Figure 6.9.d shows several layers of MMT that appear to be completely exfoliated and seem to "flow" with the polymer. These images confirm that a nanophase distribution of MMT layers was generated during in situ polymerization with **C30B**.

Figure 6.10 illustrates uniquely well the particle fragmentation mechanism that is operative with polymerizations done with **C30B**. Large MMT particles are broken into several smaller particles, starting from their edges, leading to the intercalation and exfoliation of the MMT layers by the growing polymer. It is believed this TEM image provides conclusive evidence of this fragmentation mechanism leading to a nanophase distribution of MMT layers on the polymer matrix.

a) b)

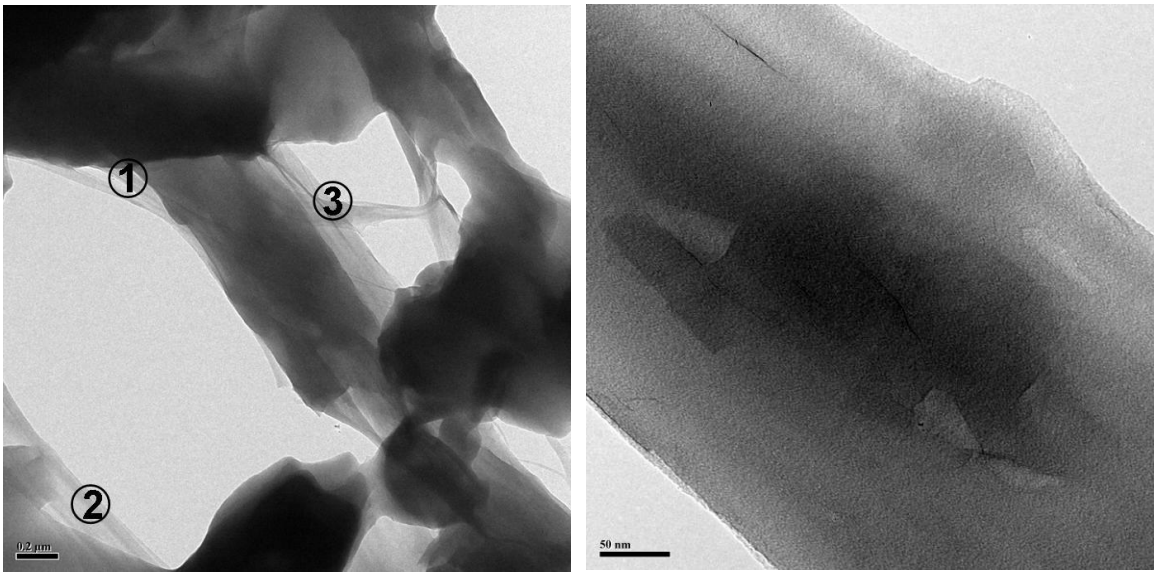

c) d)

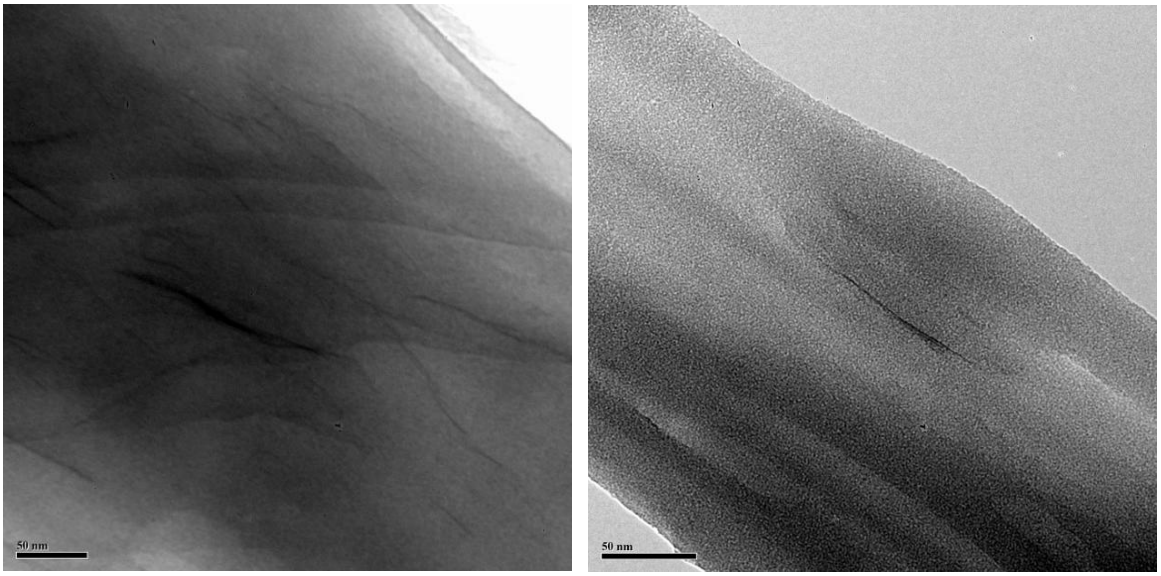

Figure 6.9. TEM micrographs (Run 17, Table 6.1): a) PE/**C30B** (scale bar 200 nm); b), c) and d) Closer views (scale bar 50 nm) of the regions marked as 1, 2 and 3 in a).

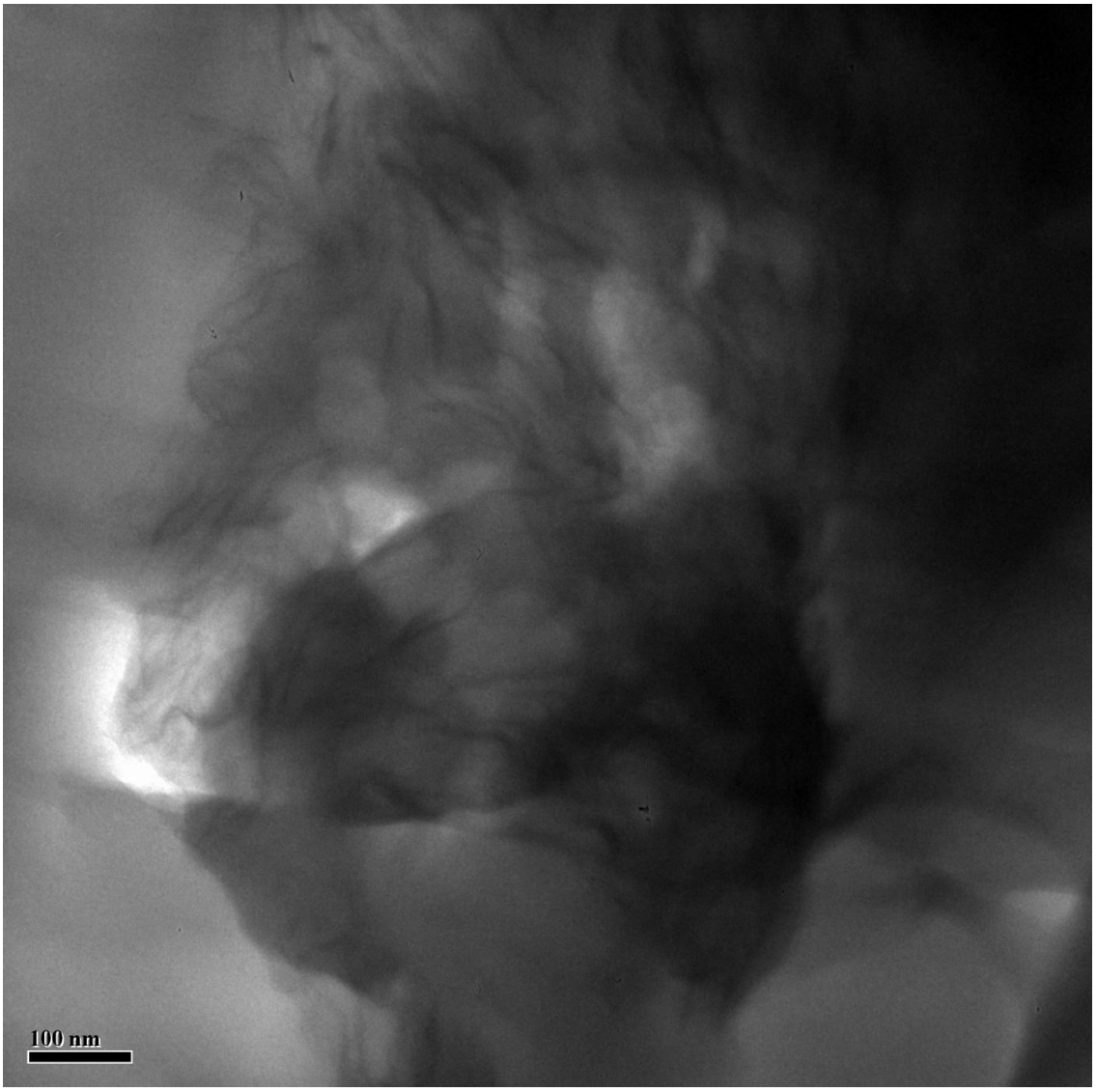

Figure 6.10. TEM micrographs of PE/**C30B** (Run 10, Table 1), scale bar 100 nm.

6.4. Conclusion

Polyethylene/montmorillonite nanocomposites were prepared by in situ polymerization with a functionalized nickel diimine catalyst (bis(4-amino-2,3,5,6-tetramethylimino)acenaphtene nickel(II) dibromide, **N2**) supported on Cloisite Na^+ and two organically-modified MMTs, Cloisite 93A and Cloisite 30B. X-ray diffractograms revealed that particle intercalation and exfoliation was initiated by the insertion of the nickel diimine complex into TMA-modified MMT galleries, and continued even further during the polymerization by the formation of polymer chains within the clay galleries.

The nanocomposites produced with **N2** supported on Cloisite 30B (**C30B)** had much better thermal properties than the nanocomposites made with Cloisite Na^+ and Cloisite 93A. In addition, **C30B** was active for ethylene polymerization even in the absence of the EASC activator, likely due to the formation of an internal activator via the reaction of TMA and the hydroxyl-functionalized organic modifier used in Cloisite 30B. It has been suggested that this internal activator also induced further intercalation of the catalyst during the supporting stage, resulting in excellent exfoliation of the MMT galleries during ethylene polymerization. SEM and TEM micrographs confirmed the formation of a nanophase of MMT layers distributed in the polymer matrix and showed polymer fibrils that seem to grow from the surface of the clay platelets.

Chapter 7 : Recommendations

An important extension of this work would be to use these supported catalysts to synthesize ethylene/polar monomer copolymers. Late transition metal catalysts with α-diimine ligands were the first catalysts capable of copolymerizing ethylene and propylene with polar functionalized vinyl monomers to high molar mass polymers by a coordination-type polymerization. Therefore, polar comonomers such as methyl acrylate and undecenyl alcohol can be selected for the synthesis of functional olefin copolymers. Copolymerization is suggested with several supported nickel diimine catalysts at various conditions (ethylene/polar monomer mole ratio, catalyst/cocatalyst mole ratio, polymerization temperature and ethylene pressure) to determine catalytic activities, comonomer incorporation abilities, resultant polymer morphology, and the effect of polar comonomers on the polymerization rate.

It was found that $MgCl_2$-based supports could be an alternative carrier for single-site catalysts due to the high activity even without activator. Moreover, polymer properties are controlled by chemical composition of $MgCl_2$-based supports. These catalysts, however, had a relatively poor morphology, with very porous and friable particles. An interesting

follow up work would involve the recrystallization of $MgCl_2$ to produce particles with well controlled morphologies and better mechanical strength.

Chapter 5 shows that hybrid supported catalysts could be used to tailor the CCD and the MWD of polyolefins. For more sophisticated polymer microstructural control, the synthesis of hybrid catalysts with different catalyst types and ratios is suggested. Various internal activators, such as borates and methylaluminoxane, could also be investigated to obtain higher activities.

Lastly, to gain a better understanding of those complicated relationships between intercalated catalysts and exfoliation of MMT layers, a wide range of polymerization conditions could be attempted. Ethylene pressure or amounts of supported catalysts on MMT may affect the degree of intercalation and exfoliation, and the distribution of the clay layers in the polymer matrix. Furthermore, mechanical property tests should be attempted to test the performance of the resultant nanocomposites and established structure-property relationships.

Bibliography

Abbenhuis, H. C. L., **Heterogenization of metallocene catalysts for alkene polymerization**, *Angew. Chem. Int. Ed.* **1999**, *3*8, 1058-1060.

Alobaidi, F., Z. Ye, S. Zhu, **Ethylene polymerization with silica-supported nickel-diimine catalyst–effect of supporting and polymerization conditions on catalyst activity and polymer properties**, *Macromol. Chem. Phys.* **2003**, *204*, 1653-1659.

Alonso, C., A. Antiñolo, F. C. Hermosilla, P. Carrión, A. Otero, J. Sancho, E. Villaseñor, **Modified silicas as supports for single-site zirconocene catalysts**, *J. Mol. Catal. A: Chem.* **2004,** *220*, 286-296.

Arai, T., H. T. Ban, T. Uozumi, K. Soga, **Syntheses of polysiloxane-supported zirconocene catalysts and application to ethene polymerization**, *Macromol. Chem. Phys.* **1997**, *198*, 229-237.

Ban, H. T., T. Uozumi, T. Sano, K. Soga, **Synthesis of metallocene catalysts supported on poly[*p*-(silylene)phenylene] derivatives for the application to olefin polymerizations**, *Macromol. Chem. Phys*. **1999**, *200*, 1897-1902.

Barret, A. G. M., T. R. de Miguel, **A well-defined metallocene catalyst supported on polystyrene beads**, *Chem. Commun*. **1998**, *19*, 2079-2080.

Bergman, J. S., G. W. Coates, H. Chen, E. P. Giannelis, M. G. Thomas, **Synthesis and characterization of polyolefin-silicate nanocomposites: a catalyst intercalation and in situ polymerization approach**, *Chem. Commun.* **1999**, *21*, 2179-2180.

Bleinmeister, J., W. Hagendorf, A. Harder, B. Heitmann, I. Schimmel, E. Schmedt, W. Schnuchel, H. Sinn, L. Tikwe, N. Von Thienen, K. Urlass, H. Winter, O. Zarncke (1995). **The role of MAO-Activators, in Zielger Catalyst**, G. Fink, R. Mülhaupt, H. H. Brintzinger, editor; Springer-Verlag: Berlin, 57-82.

Boffa, L. S., B. M. Novak, **Copolymerization of polar monomers with olefins using transition-metal complexes**, *Chem. Rev.* **2000**, *100*, 1479-1494.

Braca, G., G. Sbrana, A. M. Raspolli-Galletti, A. Altomare, G. Arribas, M. Michelotte, F. Ciardelli, **Supported transition metal complexes for ethylene polymerization**, *J. Mol. Catal. A: Chem.* **1996**, *107*, 113-121.

Brintzinger, H. H., D. Fischer, R. Mülhaupt, B. Rieger, R. M. Waymouth, **Stereospecific olefin polymerization with chiral metallocene catalysts**, *Angrew. Chem. Int. Ed.* **1995**, *34*, 1143-1170.

Bubeck, R. A., **Structure-property relationships in metallocene polyethylenes**, *Mat. Sci. Eng.* **2002**, *39*, 1-28.

Chen, Y. X., T. J. Marks, **Cocatalysts for metal-catalyzed olefin polymerization: Activators, activation processes, and structure-activity relationships**, *Chem. Rev.* **2000,** *100*, 1391-1434.

Chien, J. C. W., D. He, **Olefin copolymerization with metallocene catalysts. III. Supported metallocene/methylaluminoxane catalyst for olefin copolymerization**, *J. Polym. Sci. A: Polym. Chem.* **1991**, *29*, 1603-1607.

Cho, H. S., J. S. Chung, J. H. Han, G. Ko, W. Y. Lee, **Polymerization of ethylene and ethylene/1-hexene over Ziegler–Natta/metallocene hybrid catalysts supported on $MgCl_2$ prepared by a recrystallization method**, *J. Appl. Polym. Sci*. **1998**, *70*, 1707-1715.

Choi, Y., J. B. P. Soares, **Supported Single-Site Catalysts for Slurry and Gas Phase Olefin Polymerization**, *Can. J. Chem. Eng.* **2011**, *in press*.

Choi, Y., S. Y. A. Shin, J. B. P. Soares, **Preparation of Polyethylene/Montmorillonite Nanocomposites Through in situ Polymerization Using a Montmorillonite-Supported Nickel Diimine Catalyst**, *Macromol. Chem. Phys*. **2010a**, *211*, 1026-1034.

Choi, Y., J. B. P. Soares, **Synthesis of supported nickel diimine catalysts for ethylene slurry polymerization**, *Macromol. Chem. Phys*. **2009**, *210*, 1979-1988.

Choi, Y., J. B. P. Soares, **Ethylene slurry polymerization using nickel diimine catalysts covalently-attached onto $MgCl_2$-based supports**, *Polymer* **2010b**, *51*, 2271-2276.

Choi, Y., J. B. P. Soares, **Supported hybrid early transition metal/late transition metal catalysts for the synthesis of polyethylene with tailored molecular weight and chemical composition distributions**, *Polymer* **2010c**, *51*, 4713-4725.

Chu, K. J., J. B. P. Soares, A. Penlidis, **Polymerization mechanism for in situ supported metallocene catalysts**, *J. Polym. Sci. A: Polym. Chem.* **2000**, *38*, 462-468.

Chung, J. S., H. S. Cho, Y. G. Ko, W. Y. Lee, **Preparation of the Ziegler–Natta/metallocene hybrid catalysts on $SiO_2/MgCl_2$ bisupport and ethylene polymerization**, *J. Mol. Cat. A: Chem.* **1999**, *144*, 61–69.

Chung, T. C., **Synthesis of functional polyolefin copolymers with graft and block structures**, *Prog. Polym. Sci.* **2002**, *27*, 39-85.

Ciardelli, F., A. Altomare, M. Michelotte, G. Arribas, S. Bronco (1999). **Zeolite supported metallocene catalysts: effect of support structure and surface groups on the polymerization process, in Metalorganic Catalysts for Synthesis and Polymerization**, W. Kaminsky, editor; Springer: Berlin, 358-367.

Collins, S., W. M. Kelly, D. A. Holden, **Polymerization of propylene using supported, chiral, *ansa*-metallocene catalysts: production of polypropylene with narrow molecular weight distributions**, *Macromolecules* **1992**, *25*, 1780-1785.

Covarrubias, C. R. Quijada, R. Rojas, **Ethylene polymerization using dealuminated ZSM-2 zeolite nanocrystals as an active metallocene catalyst**, *Appl. Catal. A* **2008**, *347*, 223-233.

De Freitas, A. J. D., J. H. Z. Dos Santos, S. M. P. Meneghetti, M. R. Meneghetti, **Polymerization of ethylene: Some aspects of metallocene catalyst stabilization under homogeneous and heterogeneous reaction conditions**, *J. Appl. Polym. Sci.* **2011**, *119*, 3051-3057.

Dubois, L. H., B. R. Zegarski, **Reaction of alkoxysilane coupling agents with dehydroxylated silica surfaces**, *J. Am. Chem. Soc.* **1993**, *115*, 1190-1191.

Dubois, P., M. Alexandre, R. Jerome, **Polymerization-filled composites and nanocomposites by coordination catalysis**, *Macromol. Symp.* **2003**, *194*, 13-26.

Finch, W. C., R. D. Gillespie, D. Hedden, T. J. Marks, **Organometallic molecule-inorganic surface coordination and catalytic chemistry. In situ CPMAS NMR delineation of organoactinide adsorbate structure, dynamics, and reactivity**, *J. Am. Chem. Soc.* **1990**, *112*, 6221-6232.

Fink, G., B. Steinmetz, J. Zechlin, C. Przybyla, B. Tesche, **Propene polymerization with silica-supported metallocene/MAO catalysts**, *Chem. Rev.* **2000**, *100*, 1377-1390.

Forte, M. C., F. V. Cunha, J. H. Z. Santos, **Characterization and evaluation of the nature of chemical species generated in hybrid Ziegler–Natta/metallocene catalyst**, *J. Mol. Cat. A: Chem.* **2001**, *175*, 91-103.

Franceschini, F.C., T. T. Da R. Tavares, D. Bianchini, M. Do Carnao M. Alves, M. L. Ferreira, J. H. Z. Dos Santos, **Characterization and evaluation of supported *rac*-dimethylsilylenebis(indenyl)zirconium dichloride on ethylene polymerization**, *J. Appl. Polym*. Sci. **2009**, *112*, 563-571.

Galli, P., G. Vecellio, **Polyolefins: The most promising large-volume materials for the 21st century**, *J. Polym. Sci. Pt. A. Polym. Chem*. **2004**, *42*, 396-415.

Gate, D. P., S. A. Svejda, E. Onate, C. M. Killian, L. K. Johnson, P. S. White, M. Brookhart, **Synthesis of branched polyethylene using (alpha-diimine)nickel(II) catalysts: Influence of temperature, ethylene pressure, and ligand structure on polymer properties**, *Macromolecules* **2000**, *33*, 2320-2334.

Hamielec, A. E., J. B. P. Soares, **Polymerization reaction engineering-Metallocene catalysts**, *Prog. Polym. Sci.* **1996**, *21*, 651-706.

Heinemann, J., P. Reichert, R. Thomann, R. Mülhaupt, **Polyolefin nanocomposites formed by melt compounding and transition metal catalyzed ethene homo- and copolymerization in the presence of layered silicates**, *Macromol. Rapid Commun.* 1999, **20**, 423-430.

Hlatky, G. G., **Heterogeneous single-site catalysts for olefin polymerization**, *Chem. Rev.* **2000**, *100*, 1347-1376.

Hong, S. C., S. Mihan, D. Lilge, L. Delux, U. Rief, **Immobilized $Me_2Si(C_5Me_4)(N\text{-}tBu)TiCl_2/(nBuCp)_2ZrCl_2$ hybrid metallocene catalyst system for the production of poly(ethylene-co-hexene) with pseudo-bimodal molecular weight and inverse comonomer distribution**, *Polym.Eng. Sci.* **2007**, *47*, 131-139.

Iiskola, E. I., S. Timonen, T. T. Pakkanen, O. Härkki, P. Lehmus, J. V. Seppälä, **Cyclopentadienyl surface as a support for zirconium polyethylene catalysts**, *Macromolecules* **1997**, *30*, 2853-2859.

Ittel, S. D., L. K. Johnson, **Late-metal catalysts for ethylene homo- and copolymerization**, *Chem. Rev.* **2000**, *100*, 1169-1203.

Jamjah, R., G. H. Zohuri, M. Javaheri, M. Nekoomanesh, S. Ahmadjo, A. Farhadi, **Synthesizing UHMWPE using Ziegler-Natta catalyst system of $MgCl_2$(ethoxide type)/$TiCl_4$/tri-isobutylaluminum**, *Macromol. Symp.* **2008**, *274*, 148-153.

Janiak, C, **Metallocene and related catalysts for olefin, alkyne and silane dimerization and oligomerization**, *Coord. Chem. Rev.* **2006**, *250*, 66-94.

Johnson , L. K., C. M. Killian, M. Brookhart, **New Pd(II)- and Ni(II)-based catalysts for polymerization of ethylene and α-olefins**, *J. Am. Chem. Soc.* **1995**, *117*, 6414-6415.

Kamfjord, T., T. S. Wester, E. Rytter, **Supported metallocene catalysts prepared by impregnation of MAO modified silica by a metallocene/monomer solution**, *Macromol. Rapid Commun*. **1998**, *19*, 505-509.

Kaminaka, M., K. Soga, **Polymerization of propene with catalyst systems composed of Al_2O_3 or $MgCl_2$-supported zirconocene and $Al(CH_3)_3$**, *Polymer* **1992**, *33*, 1105-1107.

Kaminsky, W., F. Renner, **High melting polypropenes by silica-supported zirconocene catalysts**, *Makromol. Chem. Rapid Commun*. **1993**, *14*, 239-243.

Kim, I., B. H. Han, C. S. Ha, J. K. Kim, H. S. Suh, **Preparation of silica-supported bis(imino)pyridyl Iron(II) and Cobalt(II) catalysts for ethylene polymerization**, *Macromolecules* **2003**, *36*, 6689-6691.

Kim, J. D., (1998), **Synthesis of polyolefins with controlled distributions of molecular weight and chemical composition by selective combination of supported metallocene/MAO catalysts**. PhD Thesis, Chemical Engineering, University of Waterloo.

Kim, J. S., J. H. Pawlow, L. M. Wojcinski II, S. Murtuza, S. Kacker, A. Sen, **Novel nickel(II)- and palladium(II)-based catalytic systems for the synthesis of hyperbranched polymers from ethene**, *J. Am. Chem. Soc.* **1998**, *120*, 1932-1933.

Kitagawa, T., T. Uozumi, K. Soga, T. Takata, **Syndiospecific propene polymerization with polymer-supported metallocene catalyst**, *Polymer* **1997**, *38*, 615-620.

Ko, Y. S., T. S. Seo, D. S. Hong, S. I. Woo (1999). **Preparation of novel supported metallocenes and their olefin polymerization capabilities, in Metalorganic Catalysts for Synthesis and Polymerization**, W. Kaminsky, editor; Springer: Berlin, 368-380.

Lee, D. H., H. B. Lee, S. K. Noh, B. K. Song, S. M. Hong, **Ethylene polymerization initiated by anchored CpIndZrCl$_2$ on silica with hexamethyltrisiloxane and pentamethylene spacers**, *J. Appl. Polym. Sci***. 1999**, *71*, 1071-1080.

Lee, D., H. Kim, K. Yoon, K. E. Min, K. H. Seo, S. K. Noh, **Polyethylene/MMT nanocomposites prepared in situ polymerization using supported catalyst systems**, *Sci. Technol. Adv. Mater.* **2005**, *6*, 457-462.

Li, W., A. Adams, J. Wang, B. Blümich, Y. Yang, **Polyethylene/palygorskite nanocomposites: Preparation by in situ polymerization and their characterization,** *Polymer* **2010**, *51*, 4686-4697.

Lindeman, L. P., J. Q. Adams, **Carbon 13 nuclear magnetic resonance spectrometry**, *Anal. Chem.* **1971**, 43, 1245-1252.

Liu, S., F. Meng, G. Yu, B. Huang, **Preparation of polymer-supported zirconocene catalysts and olefin polymerization**, *J. Appl. Polym. Sci.* **1999**, *71*, 2253-2258.

Ma, Z., W. Sun, N. Zhu, Z. Li, C.Shao, Y. Hu, **Preparation of silica-supported late transition metal catalyst and ethylene polymerization**, *Polym. Int.* **2002**, *51*, 349-352.

Marques, M. F. C., C. A. Henriques, J. L. F. Monteiro, S. M. C. Menezes, F. M. B. Coutinho, **Bis(cyclopentadienyl)zirconium dichloride supported on zeolites for ethylene polymerization**, *Macromol. Chem. Phy*. **1997**, *198*, 3709-3717.

McKenna, T. F. L., A. D. Martino, G. Weickert, J. B. P. Soares, **Particle growth during the polymerisation of olefins on supported catalysts, 1–nascent polymer structures**, *Macromol. React. Eng*. **2010**, *4*, 40-64.

McKenna, T. F. L., J. B. P. Soares, **Single particle modelling for olefin polymerization on supported catalysts: A review and proposals for future developments**, *Chem. Eng. Sci.* **2001**, *56*, 3931-3949.

McLauchlin, A. R., N. L. Thomas, **Preparation and thermal characterisation of poly(lactic acid) nanocomposites prepared from organoclays based on an amphoteric surfactant**, *Polym. Deg. Stab.* **2009**, *94*, 868-872.

Mehdiabadi, S., J. B. P. Soares, **Influence of metallocene type on the order of ethylene polymerization and catalyst deactivation rate in a solution reactor**, *Macromol. Symp.* **2008**, *285*, 101-114.

Meng, F., G. Yu, J. Huang, **Polymer-supported zirconocene catalyst for ethylene polymerization**, *J. Polym. Sci. A: Polym. Chem.* **1999**, *37*, 37-46.

Michelotti, M., A. Altomare, F. Ciardelli, G. Rolland, **Zeolite supported polymerization catalysts: Copolymerization of ethylene and α-olefins with metallocenes supported on HY zeolite**, *J. Mol. Cat. A: Chem*. **1998**, *129*, 241-248.

Mishra, J. K., K. J. Hwang, C. S. Ha, **Preparation, mechanical and rheological properties of a thermoplastic polyolefin (TPO)/organoclay nanocomposite with reference to the effect of maleic anhydride modified polypropylene as a compatibilizer**, *Polymer* **2005**, *46*, 1995-2002.

Monrabal, B., J. Sancho-Tello, N. Mayo, L. Romero, **Crystallization elution fractionation. A new separation process for polyolefin resins**, *Macromol. Symp.* **2007**, *257*, 71-79.

Nakayama, Y., J. Saito, H. Bando, T. Fujita, **$MgCl_2$/R'nAl$(OR)_{3-n}$: An excellent activator/support for transition-metal complexes for olefin polymerization**, *Chem. Eur. J*. **2006**, *12*, 7546-7556.

Nishida, H., T. Uozumi, T. Arai, K. Soga, **Polystyrene-supported metallocene catalysts for olefin polymerizations**, *Macromol. Rapid Commun*. **1995**, *16*, 821-830.

Park, H. W., J. S. Chang, S. H. Bae, I. K. Song, **Physical property and chemical composition distribution of ethylene–hexene copolymer produced by metallocene/Ziegler–Natta hybrid catalyst**, *J. Mol. Cat. A: Chem.* **2006**, *255*, 69-73.

Peruch, F., H. Cramail, A. Deffieux, **Kinetic and UV-visible spectroscopic studies of 1-hexene polymerization initiated by an alpha-diimine-[N,N] nickel dibromide/MAO catalytic system**, *Macromolecules* **1999**, *32*, 7977-7983.

Preishuber-Pflugl, P., M. Brookhart, **Highly active, supported nickel diimine catalysts for polymerization of ethylene**, *Macromolecules* **2002**, *35*, 6074-6076.

Przybyla, C., B. Weimann, G. Fink (1999). **Influence of the particle size of silica support on the kinetics and the resulting polymer properties at the polypropylene polymerization with heterogeneous metallocene catalysts; Part II: development of a model as well as a mathematical simulation, in Metalorganic Catalysts for Synthesis and Polymerization**, W. Kaminsky, editor; Springer: Berlin, 333-346.

Przybyla, C., J. Zechlin, B. Steinmetz, B. Tesche, G. Fink (1999). **Influence of the particle size of silica support on the kinetics and the resulting polymer properties at the polypropylene polymerization with heterogeneous metallocene catalysts; Part I: experimental studies and kinetics analysis, in Metalorganic Catalysts for Synthesis and Polymerization**, W. Kaminsky, editor; Springer: Berlin, 321-332.

Pullukat, T. J., R. Shinomoto, C. Gillings, **Silica supports for metallocene catalysts**, *Plastics, Rubber and Composites processing application* **1998**, *27*, 8-11.

Quijada, R., R. Rojas, L. Alzamore, J. Retuert, F. M. Rabagliati, **Study of metallocene supported on porous and nonporous silica for the polymerization of ethylene**, *Catalysis Letters* **1997**, *46*, 107-112.

Rahiala, H., I. Beurroies, T. Eklund, K. Hakala, R. Gougeon, P. Trens, J. B. Rosenholm, **Preparation and characterization of MCM-41 supported metallocene catalysts for olefin polymerization**, *J. Catalysis* **1999**, *188*, 14-23.

Ray, S. S., M. Okamoto, **Polymer/layered silicate nanocomposites: a review from preparation to processing**, *Prog. Polym. Sci.* **2003**, *28*, 1539-1641.

Reddy, C. S., C. K. Das, **Polypropylene–nanosilica-filled composites: Effects of epoxy-resin-grafted nanosilica on the structural, thermal, and dynamic mechanical properties**, *J. Appl. Polym. Sci.*, **2006**, *102*, 2117-2124.

Santos, J. H. Z., S. Dorneles, F. C. Stedile, J. Dupont, M. C. Forte, I. J. R. Baumvol, **Silica supported zirconocenes and Al-based cocatalysts: surface metal loading and catalytic activity**, *Macromol. Chem. Phys.* **1997**, *198*, 3529-3537.

Santos, J. H. Z., C. Krug, M. B. da Rosa, F. C. Stedile, J. Dupont, M. C. Forte, **The effect of silica dehydroxylation temperature on the activity of SiO_2-supported zirconocene catalysts**, *J. Mol. Cat. A: Chem.* **1999**, *139*, 199-207.

Santos, J. H. Z., A. Larentis, M. B. da Rosa, C. Krug, I. J. R. Baumvol, J. Dupont, F. C. Stedile, M. C. Hagg, M. C. Forte, **Optimization of a silica supported bis(butylcyclopentadienyl)-zirconium dichloride catalyst for ethylene polymerization**, *Macromol. Chem. Phys.***1999**, *200*, 751-757.

Schneider, H., G. T. Puchta, F. A. R. Kaul, G. R. Sieber, F. Lefebvre, G. Saggio, D. Mihalios, Herrmann, W. A., J. M. Basset, **Immobilization of η^5-cyclopentadienyltris(dimethylamido)zirconium polymerization catalysts on a**

chlorosilane- and HMDS-modified mesoporous silica surface: a new concept for supporting metallocene amides towards heterogeneous single-site catalysts, *J. Mol. Catal. A: Chem.* **2001**, *170*, 127-141.

Schrekker, H. S., V. Kotov, P. P. Pflugl, P. White, M. Brookhart, **Efficient slurry-phase homopolymerization of ethylene to branched polyethylenes using α-diimine nickel(II) catalysts covalently linked to silica supports**, *Macromolecules* **2006**, *39*, 6341-6354.

Severn, J. R., J. C. Chadwick, **MAO-free activation of metallocenes and other single-site catalysts for ethylene polymerization using spherical supports based on $MgCl_2$**, *Macromol. Rapid Comm.* **2004a**, *25*, 1024-1028.

Severn, J. R., J. C. Chadwick, **$MgCl_2$-based supports for the immobilization and activation of nickel diimine catalysts for polymerization of ethylene**, *Macromolecules* **2004b**, *37*, 6258-6259.

Shin, S. A., L.C. Simon, J. B. P. Soares, G. Scholz, **Polyethylene-clay hybrid nanocomposites: in situ polymerization using bifunctional organic modifiers**, *Polymer* **2003**, *44*, 5317-5321.

Simplicio, L. M. T., F. G. Costa, J. S. Boaventura, E. A. Sales, S. T. Brandão, **Study of some parameters on the zirconocene immobilization over silica**, *J. Mol. Catal. A: Chem.* **2004**, *216*, 45-50.

Soares, J. B. P., T. F. McKenna, C. P. Cheng (2007). **Coordination polymerization. in Polymer Reaction Engineering**, J. M. Asua, editor; Blackwell publishing, Oxford, 29-117.

Soares, J. B. P., J. D. Kim, **Copolymerization of ethylene and alpha-olefins with combined metallocene catalysts. I. A formal criterion for molecular weight bimodality**, *J. Polym. Sci. A: Polym. Chem.* **2000**, *38*, 1408-1416.

Soga, K., T. Arai, T. Uozumi, **Polymerization of propene over a $MgCl_2$-supported dichlorosilylenebisindenylzirconium dichloride catalyst combined with methylalumoxane**, *Polymer* **1997**, *38*, 4993-4995.

Soga, K., M. Kaminaka, **Copolymerization of olefins with SiO_2-, Al_2O_3-, and $MgCl_2$-supported metallocene catalysts activated by trialkylaluminiums**, *Macromol. Chem. Phys.* **1994**, *195*, 1369-1379.

Soga, K., M. Kaminaka, **Polymerization of propene with the heterogeneous catalyst system $Et[IndH_4]_2ZrCl_2/MAO/SiO_2$ combined with trialkylaluminium**, *Makromol. Chem. Rapid Commun*. **1992**, *13*, 221-224.

Soga, K., M. Kaminaka, **Polymerization of propene with zirconocene-containing supported catalysts activated by common trialkylaluminiums**, *Makromol. Chem.***1993**, *194*, 1745-1755.

Soga, K., H. J. Kim, T. Shiono, **Highly isospecific SiO_2-supported zirconocene catalyst activated by ordinary alkylaluminiums**, *Macromol. Rapid Commun.***1994a**, *15*, 139-143.

Soga, K., H. J. Kim, T. Shiono, **Polymerization of propene with highly isospecific. SiO_2-supported zirconocene catalysts activated with common alkylaluminiums**, *Mackromol. Chem. Phys.* **1994b**, *195*, 3347-3360.

Soga, K., R. Koide, T. Uozumi, **Syndiotactic polymerization of styrene with Al_2O_3-supported Cp*$TiCl_3$ catalyst activated by trialkylaluminiums**, *Makromol. Chem. Rapid Commun*. **1993a**, *14*, 511-514.

Soga, K., D. H. Lee, **Polymerization of olefins with the catalyst system (RCp)$TiCl_3$ (R = H, CH_3)/SiO_2-common alkylaluminium activated with a suitable Lewis acid**, *Makromol. Chem*. **1992**, *193*, 1687-1694.

Soga, K., T. Shiono, H. J. Kim, **Activation of SiO_2-supported zirconocene catalysts by common trialkylaluminiums**, *Makromol. Chem*. **1993b**, *194*, 3499-3504.

Soga, K., T. Uozumi, M. Saito, T. Shiono, **Structure of polypropene and poly(ethylene-co-propene) produced with an alumina-supported $CpTiCl_3$/common alkylaluminium catalyst system**, *Macromol. Chem. Phys.***1994c**, *195*, 1503-1515.

Suhm, J., M. J. Schneider, R. Mülhaupt, **Influence of metallocene structures on ethene copolymerization with 1-butene and 1-octene**, *J. Mol. Catal. A: Chem.* **1998**, *128*, 215-227.

Sun, L., A. Shariati, J. C. Hsu, D. W. Bacon (1994). **A new polymer-supported catalyst for olefin polymerization, in Catalyst Design for Tailor-Made Polyolefins**, K. Soga and M. Terano, editors; Elsevier-Kodansha: Tokyo, 81-89.

Sun, T., J. M. Garces, **High-performance polypropylene–clay nanocomposites by in situ polymerization with metallocene/clay catalysts**, *Adv. Mat.* **2002**, *14*, 128-130.

Tait, P. J. T., R. Ediati (1999). **Supported metallocene catalysts for propene polymerization, in Metalorganic Catalysts for Synthesis and Polymerization**, W. Kaminsky, editor; Springer: Berlin, 307-320.

Timonen, S., T. T. Pakkanen, E. I. Iiskola, **Immobilization of zirconium amide on a Cp-modified silica surface and its use as a catalyst for ethylene polymerization**, *J. Organomet. Chem*. **1999**, *582*, 273-278.

Todor, J., L. Willington, D. O'Hare, B. Royan, **Intercalation of catalytically active metal complexes in phyllosilicates and their application as propene polymerisation catalysts**, *Chem. Comm.* **1996**, 2031-2032.

Usaki, A., M. Kato, A. Okada, T. Kurauchi, **Synthesis of polypropylene-clay hybrid**, *J. Appl. Polym. Sci***. 1997**, *63*, 137-138.

Usami T., S. Takayama, **Fine-branching structure in high-pressure, low-density polyethylenes by 50.10-MHz carbon-13 NMR analysis**, *Macromolecules* **1984**, *17*, 1756–1761.

Uozumi, T., T. Toneri, K. Soga, **Copolymerization of ethylene and 1-octene with Cp*TiCl$_3$ as catalyst supported on 3-aminopropyltrimethoxysilane treated SiO$_2$**, *Macromol. Rapid Commun.* **1997**, *18*, 9-15.

Wang, B., ***Ansa*-metallocene polymerization catalysts: Effects of the bridges on the catalytic activities**, *Coord. Chem. Rev.* **2006**, *250*, 242-258.

Weiss, K., C. Wirth-Pfeifer, M. Hofmann, S. Botzenhardt, H. Lang, K.Bruning, E. Meichel, **Polymerisation of ethylene or propylene with heterogeneous metallocene catalysts on clay minerals**, *J. Mol. Catal. A: Chem.* **2002**, *182*, 143-149.

Wilke, G., **Contributions to organo-nickel chemistry**, *Angew. Chem. Int. Ed.* **1988**, *27*,185-206.

Woo, S. I., Y. S. Ko, T. K. Han, **Polymerization of ethylene over metallocenes confined inside the supercage of a NaY zeolite**, *Macromol. Rapid Commun.* **1995**, *16*, 489-494.

Xu, J., J. Ouyang, Z. Fan, D. Chen, L. Feng, **Polymer-supported half-titanocene catalysts for the syndiospecific polymerization of styrene**, *J. Polym. Sci. A: Polym. Chem.* **2000**, *38*, 127-135.

Xu, R., D. Liu, S. Wang, B. Mao **Preparation of spherical $MgCl_2$-supported late-transition metal catalysts for ethylene polymerization**, *Macromol. Chem. Phys.* **2006**, *207*, 779-786.

Zhu J., F. M. Uhl, A. B. Morgan, C. A. Wilkie, **Studies on the mechanism by which the formation of nanocomposites enhances thermal stability**, *Chem. Mater.*, **2001**, *13*, 4649-4654.

US Patent 4701432 (1986), Exxon Chemical Patents Inc., inv.: H. C. Welborn Jr.

US Patent 5006500 (1991), Exxon Chemical Patents Inc., inv.: M. Chang.

US Patent 5238892 (1993), Exxon Chemical Patents Inc., inv.: M. Chang.

US Patent 5635437 (1997), Exxon Chemical Patents Inc., inv.: T. J. Burkhardt, W. B. Brandley.

US Patent 5767300 (1998). LG Chem, inv.: B. Y. Lee.

US Patent 6124029 (2000), Witco GmbH, inv.: R. J. Becker, R. Reiger.

US Patent 6114555 (2000), Repsol, invs.: A. M. Lafuente, G. H. Llinas

US Patent 7294600 (2007), LG Chem., invs.: K. S. Lee, H. S. Lee, E. J. Lee, S. W. Lee, C. H. Lee.

World Intellectual Property Organization (WO) Patent 087770 (2004), LG Chem, inv.: K. S. Lee, H. S. Lee, E. J. Lee, S. W. Lee, C. H. Lee.

World Intellectual Property Organization (WO) Patent 094302 (2006), E. I. Dupont de Nemours & Co., M. Brookhart, J. Citron, H. Schrekker, invs.: M. Brookhart, J. Citron, H. Schrekker.